NASA-CR-195111

Report No: TRC-EM-CAB-9401

ADVANCED ELECTROMAGNETIC METHODS FOR AEROSPACE VEHICLES

Semiannual Progress Report
(July 1 - December 31, 1993)

IN-31-CR
97P

by
Constantine A. Balanis
Weimin Sun
El-Budawy El-Sharawy
James T. Aberle
Craig R. Birtcher
Jian Peng
Panayiotis A. Tirkas
William V. Andrew
David Kokotoff
Frank Zavosh

N94-24699
Unclas
G3/37 0204163
(NASA-CR-195111) ADVANCED ELECTROMAGNETIC METHODS FOR AEROSPACE VEHICLES Semiannual Progress Report, 1 Jul. - 31 Dec. 1993 (Arizona State Univ.) 97 p

Prepared by

Telecommunications Research Center
College of Engineering and Applied Science
Arizona State University
Tempe, AZ 85287-7206

Sponsored by

Grant No. NAG-1-1082
National Aeronautics and Space Administration
Langley Research Center
Hampton, VA 23665

Contents

I. INTRODUCTION **1**

II. COMPOSITE MATERIALS **4**

A. Introduction 4
B. Antenna Patterns of Low Conductivity Composite Materials . 5
C. Guidelines of Green's Function Analysis of Composite Material Structures 8
D. FD-TD Modeling of Volumetric Composite Materials 10
E. FDTD Modeling of Pyramidal Horns With Composite E-plane Walls 12
F. Efficiencies of Horn Antennas Loaded with Composite Materials 14
G. Future Work 18

III. ANTENNA TECHNOLOGY **54**

A. Introduction 54
B. Cavity-Backed Microstrip Patch Antennas 54
C. Ferrite Tuned Cavity Backed Slot Radiators 59
D. Cavity Backed Slot Experiments 65

I. INTRODUCTION

The Advanced Helicopter Electromagnetics (AHE) Industrial Associates Program has fruitfully completed its fourth year. Under the support of the AHE members and the joint effort of the research team, new and significant progresses have been achieved in the year. Following the recommendations by the Advisory Task Force, the research effort is placed on more practical helicopter electromagnetic problems, such as HF antennas, composite materials and antenna efficiencies. In this annual report, the main topics to be addressed include

- Composite Materials
- Antenna Technology

The research work on each topic has been driven by the AHE Consortium members' interests and needs. The remarkable achievements and progresses in each subject is reported respectively in individual sections of the report.

The remarkable work in the area of Composite Materials includes:

a. Modeling of low conductivity composite materials by using Green's function approach;

b. Guidelines for composite material modeling by using the Green's function approach in the NEC code;

c. Development of 3-D volume mesh generator for modeling thick and volumetric dielectrics by using FD-TD method;

d. Modeling antenna elements mounted on a composite Comanche tail stabilizer;

e. Antenna pattern control and efficiency estimate for a horn antenna loaded with composite dielectric materials.

The research in the area of Composite Materials has long been focused on analytic modeling of composite sheets by using the Green's function approach. Some simple composite geometries such as the thin plate, wedge, and square plate grounded monopole have been previously designed to verify the Green's function approach in composite material modeling. Using

the surface impedance concept, the approach showed encourage agreement with measurements. Based on these previous work, this technique has been coupled into the NEC code to provide an equivalent surface impedance distribution, which is subsequently used by the NEC code for pattern predictions. To provide a guideline for using the surface impedance concept in antenna modelings, some conclusive remarks are provided in the report.

In addition to the Green's function modeling technique, the FD-TD has been widely used in dealing with composite structures. The direct application of the technique or direct use of an FD-TD code solely relies on the discretization of a complex geometry. In previous research periods, an FD-TD mesh generator has been developed; however it is based on surface mesh generation which is only applicable to objects consisting of conducting surfaces and thin dielectrics. The work on FD-TD modeling in this period has been extended by developing the volume FD-TD mesh generator. The automatic 3-D volume mesh generation allows the modeling of geometries involving thick and volumetric composite materials. To demonstrate the 3-D volume mesh generation, the numerical modelings of a lossy dielectric sphere, a grounded monopole on a thick composite substrate, and a composite Comanche tail stabilizer are reported.

The recent research revealed a significant improvement in bandwidth of a horn antenna loaded with composite materials. It was found that the FDTD method coupled with the contour path integrals is a robust approach to model this type of antennas. New results on radiation patterns of a horn loaded with composite materials have been obtained numerically and experimentally. Since antenna efficiency is a key issue in design of antennas mounted on helicopter platforms, especially when the antennas are loaded with lossy composite materials, the research on this subject has been recommended by the AHE Advisory Task Force at the biannual meeting held at the Boeing Helicopter on May 19 -20, 1993. In this report, the work on antenna efficiency modeling of a horn antenna loaded with composite sheets is also reported.

In the area of Antenna Technology, new and significant progresses have been achieved in investigations of conformal cavity-backed microstrip and ferrite-loaded cavity-backed antennas. The conformal cavity-backed microstrip antennas are used to overcome the tradeoff between bandwidth and scan volume in an array. The ferrite-loaded cavity-backed antennas are not only conformal to airplane fuselage, but also tunable in operation frequency. Most importantly, they have a potential use in UHF or even VHF frequencies.

The scattering and radiation performance of single elements of circular patches backed by circular and rectangular cavities were reported before. Since then, we have succeeded in verifying some of the theoretical results by experiments. Also, we have developed numerical code for the analysis of the radiation characteristics of infinite arrays of probe-fed circular patches each backed by a circular or rectangular cavity.

In the past, a two-dimensional analytical model of a magnetically-tuneable cavity-backed slot antenna was introduced. In this report, a three-dimensional analytical model of a cavity-backed slot antenna is provided with specific intent of analyzing the tuning capabilities of such an antenna at VHF and UHF frequencies. Now, the analytic model has the capability to calculate the monostatic or bistatic RCS (radar cross section) of the CBS antenna loaded with ferrite and dielectric layers. While the theoretical analysis work is on-going, some fundamental experiments on these ferrite-loaded cavity backed antennas have also been conducted. A new feed configuration has been successfully designed. Both magnetostatic volume and surface wave modes can be excited strongly with this new configuration. It is the magnetostatic volume mode that needs to be excited in order to have any potential of resonating such elements at UHF or VHF frequencies.

II. COMPOSITE MATERIALS

A. Introduction

The research in the area of Composite Materials has been conducted both experimentally and numerically. An approximate but efficient Green's function approach has been previously developed for modeling composite materials. This approach is focused on:

a. Analytic modeling of composite sheets by using the Green's function approach

b. Evaluation of their equivalent surface impedances

c. NEC code simulation taking into account of the surface impedance of the materials

Accordingly, some simple composite geometries, such as the thin plate, wedge and square plate grounded monopole, have been previously designed to verify the Green's function approach in composite material modeling. Using the surface impedance concept, the approach showed encouraging agreement with measurements. Based on the results of the previous work, this technique has been coupled into the NEC code to provide an equivalent surface impedance distribution, which is subsequently used by the NEC code for pattern predictions. To provide a guideline for using the surface impedance concept in antenna modelings, some conclusive remarks are provided in the report to help the AHE consortium members in their numerical work.

In addition to the Green's function modeling technique, the FD-TD has been demonstrated in the previous reports to be a powerful and accurate technique dealing with composite structures. The theory of FD-TD has been very well developed. The direct application of the technique or direct use of an FD-TD code solely relies on the discretization of a complex geometry. For a complex structure involving composite materials, the FD-TD mesh generation is not an easy task. In previous research periods, an FD-TD surface mesh generator has been developed; however it is based on ray-tracing algorithm which is applicable to objects consisting of conducting surfaces and thin dielectrics. The work on FD-TD modeling in this period has been upgraded by developing the volumetric FD-TD mesh generator. The automatic

3-D volumetric mesh generation allows the modeling of geometries involving thick and volumetric composite materials. To demonstrate the 3-D volumetric mesh generation, the numerical modelings of a lossy dielectric sphere and a grounded monopole on a thick composite substrate have been tested. Subsequently, the mesh generation has further been applied to a scaled composite Comanche tail stabilizer on which an antenna is mounted.

The recent research revealed a significant improvement in bandwidth of a horn antenna loaded with composite materials. It was found that the FDTD method coupled with the contour path integrals is a robust approach to model this type of antennas. New results on radiation patterns of a horn loaded with composite materials have been obtained numerically and experimentally. Since antenna efficiency is a key issue in design of antennas mounted on helicopter platforms, especially when the antennas are loaded with lossy composite materials, the research on this subject has been recommended by the AHE Advisory Task Force at the biannual meeting held at the Boeing Helicopter on May 19 -20, 1993. In this report, the work on antenna efficiency modeling of a horn antenna loaded with composite sheets is also reported.

B. Antenna Patterns of Low Conductivity Composite Materials

The objective of this work is to develop the parameters and criteria, necessary for accurately predicting and analyzing the effects of composite materials on antenna systems, mounted on helicopter platforms. The criteria to be developed are the mesh size, the wire diameter, and the location of the equivalent wire grid relative to the actual location of the antenna structure. Preliminary work has been done in this area last year, but further investigation and verification is required. In our previous reports we presented theory and measurements of:

a. Antenna and RCS patterns on composite materials of high conductivity such as graphite epoxy and fiberglass with screens near the surface.

b. Antenna patterns on composite materials of low conductivity including microwave absorbers.

c. RCS patterns of low conductivity materials.

In the above cases, the surface impedance of the composite material is evaluated using a spectral domain Green's functions approach and utilized to model the structure under investigation as a wire grid. The pattern of the structure is then computed using the wire grid option of NEC code. Monopole antennas on composite materials have been built and tested. Good agreement between predictions and measurements of radiation patterns of these antennas have been observed. The RCS patterns of structures made of composite materials were also predicted and are in good agreement with measurements.

In this report, the analysis criteria, developed and presented in our 1992 annual progress report, are tested and verified for the towel bar antenna. The towel bar antenna is used quite often in modern helicopter platforms and has certain advantages in composite material structures. This report shows that the radiation efficiency of towel bar antenna may not be reduced by implementing composite materials in the helicopter structure. The difference in absolute values of the measured patterns for the radiated fields is only about 1 dB.

1. Theory

It has been shown in our previous reports that the surface impedance Z_s of a two-layer media including a layer of composite material , can be written as

$$\bar{\bar{Z}}_s = (\bar{\bar{T}}_E + \bar{\bar{Z}}_T \bar{\bar{G}}_s)(\bar{\bar{Y}}_T + \bar{\bar{T}}_J \bar{\bar{G}}_s)^{-1} \tag{1}$$

$$\bar{\bar{G}}_s = \bar{\bar{T}}_{LJ} \bar{\bar{Z}}_{LT}^{-1}$$

where $\bar{\bar{Z}}_T$, $\bar{\bar{Y}}_T$, $\bar{\bar{T}}_E$, $\bar{\bar{T}}_J$ are the transmission matrices of the composite material and the subscript L denotes the medium below the composite material. At the limit when the thickness d of the bottom layer equal zero, the surface impedance becomes

$$\bar{\bar{Z}}_s = \bar{\bar{Z}}_T \bar{\bar{T}}_J^{-1} \tag{2}$$

If the structure under investigation is to be modeled using the two-impedance sheet method, as discussed in our previous progress reports, the contributions of the ground plane are duplicated. The surface impedance in

(1) assumes a ground plane at the back of the composite material. In addition, a PEC sheet is introduced again in the two-sheet wire grid model. This is most likely to increase the predicted RCS and antenna patterns of composite materials. To solve this problem, the free space ground plane admittance is subtracted from the above surface admittance as

$$\bar{\bar{Z}}_s^m = (\bar{\bar{Y}}_s - \bar{\bar{Y}}_s^a)^{-1} \tag{3}$$

where $\bar{\bar{Y}}_s^a$ is the free space admittance (can be found using (2)) and $\bar{\bar{Z}}_s^m$ is the modified surface impedance to avoid the inclusion of the ground plane twice.

2. Measurements and Predictions of Towel bar Antenna Patterns on Composite Materials

To show the effects of composite materials on the towel bar antenna patterns, a bar antenna was measured at 4 GHz and 5 GHz on a 6"x6" ground plane. The ground plane was partially covered with a 6"x3" microwave absorber (Figure 1). The thickness of the absorber was 40.0 mil (about 1.0 mm). The length and the height of the antenna were 3" and 0.3", respectively. As shown in Figures 2 and 3, the measured patterns of the towel bar antenna on composite materials were slightly different from the pattern of the same antenna on PEC (the composite material is removed). Thus, the radiation efficiency is not significantly sacrificed due to the composite material. In fact, at 4 GHz, the measured gain of the antenna increased by adding the composite material. This can be explained by the fact that, the image of the towel bar antenna counteracts the antenna element itself. This usually occurs when the antenna current is parallel to the ground plane. The composite material in this case weakens the effects of the image resulting in the observed improvement in the radiation pattern. This is in contrast with other types of antennas, such as the monopole antenna, where the image co-acts with the antenna. This occurs when the antenna current is perpendicular to the ground plane. In this case, the reduction in the radiation efficiency due to composite materials can be significant. As presented in our 1992 annual progress report, the effect of the composite material on monopole antennas is to reduce the overall pattern by as much as 10 dB.

We measured the material properties between 8.2-12.4 GHz using the

waveguide technique. The measured properties were then interpolated to ϵ_r =14.9-j0.1, μ_r =2.0-j1.6 at 5 GH. The structure was modeled as two wire grids with upper grid loaded with the computed surface impedance of the composite material (6+j38 ohms). The ratio of the mesh size of the upper grid (the composite material surface) to the wire radius was about 7. In the computation, only one value of the surface impedance, calculated at a radiation angle of 45^0 , was used. Initially, we had numerical problems in running the NEC code to model the above structure. These numerical problems were attributed to the presence of an excitation nearby the edge of the composite material. The edge singularity interfered with the calculations and resulted in a negative value of the input impedance of the antenna. This problem was solved by connecting the edges to the ground plane. The computed versus measured radiation patterns at 5 GHz are shown in Figures 4 and 5. The measured and computed patterns of the antenna on a PEC are also displayed in Figures 4 and 5 . Reasonably, good agreement is observed between theory and measurements, except at the back of the antenna where the discrepancy was about 4 dB. This is expected since the feed cables and circuits are not included in the model.

3. Conclusion

The effects of low conductivity composite materials on the towel bar antenna patterns is analyzed and presented. The code has been validated by computing the surface impedance and comparing predicted patterns to measurements of an antenna partially covered with a microwave absorber material. Small differences in the pattern of the towel bar antenna were observed due to the inclusion of composite materials in the structure. This suggests that the towel bar antenna may be an attractive antenna for platforms that employs composite materials of low conductivity.

C. Guidelines of Green's Function Analysis of Composite Material Structures

As stated previously, the analysis of composite materials mounted on helicopter platforms can employ the concept of the equivalent surface impedance. The surface impedance of the composite material is evaluated using a spectral domain Green's function approach and is utilized to model the composite

material structure as a wire grid. The electromagnetic characteristics of the structure are then computed using the wire-grid option of the NEC code. The parameters and criteria for using the wire grid model are:

- Wire radius; for PEC the wire radius can be chosen with a great deal of flexibility and is usually equal 0.01λ. For composite materials, the radius should equal the thickness of the composite material for best agreement with measurements. If there is a ground plane at the back of the composite material, the radius is chosen slightly less than the thickness of the composite material to avoid contact between the wire grid representing the composite material and the wire grid representing the ground plane.

- Mesh size; the standard mesh size is $0.1\lambda \times 0.1\lambda$ for PEC. The mesh size for composite materials has to be chosen such that the surface area of the wire equal approximately the surface area of the composite material. A typical ratio between the size and the radius of the wire is 7. Since the radius equal approximately the thickness, the mesh size is about 7 times the thickness. As the thickness of the composite material gets smaller compared to wavelength, a finer wire and smaller mesh is required to model the composite material.

As reported in the above section, work has been done to verify the above criteria The predicted RCS patterns of structures made of composite materials were in good agreement with measurements. Also, monopole antennas on low conductivity composite materials have been built and tested with good agreement between predictions and measurements of radiation patterns of these antennas.

The radiation efficiency of a towel bar antenna may not be reduced by implementing composite materials in the helicopter structure. The difference in the measured patterns values for the radiated fields is only about 2 dB. Our prediction for this type of antenna shows some discrepancy due to the interference of edge singularities and the calculations of the antenna input impedance. Without some precautions, the edge singularity may even result in a negative input impedance in which case the NEC code terminates the calculations prematurely. We detected this problem with an all PEC towel bar antenna. This leads to the conclusion that this problem is inherent with

the NEC code itself. In a personal discussion with Dr. Granzella from ESL, a subsidiary of TRW, he confirmed the same problem with the NEC code.

The above problem can be due to numerical inaccuracy or lack of the appropriate boundary conditions. To insure that this problem is not due to the latter, the NEC code was utilized to plot the current distribution of a $\lambda/2 \times \lambda/2$ sheet of composite material due to a plane wave incident at an angle $\theta = 45$ degrees, as shown in Figure 6. The material has a surface impedance of 5+j5 ohms. Figures 7 and 8 shows the current distribution on the sheet. The current behavior shows that the NEC code predicts the appropriate current edge conditions; the perpendicular currents vanish at the edges and the parallel currents increase near the edge.

In conclusion, we found that the Green's function approach provides good results in all cases that we tested except when an edge singularity is close to the excitation of the antenna. The combination of the Green's function surface impedance software/NEC code can handle a wide variety of scattering and antenna structures, including composite material with or without a metal backing.

D. FD-TD Modeling of Volumetric Composite Materials

The FD-TD method has been demonstrated to be a powerful and accurate technique in dealing with composite structures. However, the direct application of the technique or direct use of an FD-TD code relies on the discretization of a given complex geometry. When the geometry consists of only perfectly conducting surfaces, an FD-TD surface mesh generation algorithm can be used, because the FD-TD method only wants to know the cell indices on the conducting surfaces where the boundary conditions are enforced. Consequently, an efficient ray-tracing surface mesh generation program has been previously developed and integrated with the GEOM program. However, in dealing with objects consisting of both conductors and dielectrics, a 3-D volumetric mesh generation is inevitable. Recently we developed a 3-D volumetric FD-TD mesh generator. The automatic 3-D volumetric mesh generation allows the modeling of geometries involving thick and volumetric composite materials. The algorithm used for 3-D volumetric mesh generation is based on the previous surface mesh generation algorithm plus the

algorithm of reconstructing the volumetric mesh from boundary (or surface) elements. So far, the new 3-D volumetric mesh generation algorithm has not only been tested by modeling a lossy dielectric sphere and a monopole antenna grounded with both conducting and thick composite substrate, but also been applied to model realistic complex geometries such as the composite Comanche tail stabilizer.

As shown in Figure 9, a dielectric sphere was tested. The sphere has been used as a demonstration simply because of the availability of analytic solutions. The sphere has a radius of one half wavelength and its permittivity is $\epsilon_r = 2.0$, conductivity $\sigma = 0.001 S/m$, and permeability $\mu_r = 1.0$. The sphere is illuminated by a 300 MHz plane wave incident traveling in the negative z-direction and polarized toward the x-direction. A FD-TD lattice is automatically generated by the 3-D volumetric mesh generator with 30 cells per wavelength. The radar cross sections of the sphere in the planes of $\phi = 90^0$ and $\phi = 0^0$ are plotted in Figures 10 and 11. The FD-TD predictions have been compared with the exact solutions of Mie Theory. It is seen that the FDTD results agree with the Mie Theory quite well except in the backscattered directions. This discrepancy is due to the error of the stair-case modeling of smooth spherical surfaces.

The second example tested was a monopole antenna mounded on a ground plane. But the ground plane is placed on a very thick composite substrate. The geometry of problem is shown in Figure 12 where the ground plate is 2λ by 2λ and the composite material is one λ thick. The electric parameters of the composite material are the same as those used in the first example. The antenna radiation patterns in three principal planes are plotted in Figures 13 - 15. Significant backlobes, due to the contribution of the material substrate, can be seen in the patterns.

The third example is a scaled Comanche tail stabilizer. The original geometry of the stabilizer is shown in Figure 16, and its solid surface model is shown in Figure 17 where only a monopole antenna operating at 2 GHz is analyzed. The discretized FD-TD volumetric mesh of the stabilizer is shown in Figure 18. The computation domain is about 86x206x48 cells. The mesh generation for such a computation domain is less than 1 minute on the IBM RS/6000 350 machine. Three configurations have been analyzed which include 1) the all-metallic stabilizer; 2) the composite stabilizer ($\epsilon_r = 3.0 - j1.0^{-5}$) with a metal ground strip of 7.5" wide; and 3) the composite stabilizer ($\epsilon_r = 3.0 - j1.0^{-5}$) with a metal ground strip of 2.5"wide. Their

radiation power patterns in the pitch, roll, and yaw planes are compared and shown respectively in Figures 19-21. It is seen that in the yaw plane (XY plane), the radiation efficiency of an antenna on the composite stabilizer is much lower than that of the antenna on an all-metallic stabilizer. Obviously the dielectric loss contributes significantly to this deficiency. Several near field distribution patterns have been provided in Figures 22-25. Figures 22 and 23 shows the y- and z-components of electric fields inside the composite stabilizer (with 7.5" metal strip), while Figures 24 and 25 shows x-component of electric field and x-component of magnetic field on the surface of metal strip. The y-component of the surface current on the strip is the same as the x-component of magnetic field, and it is seen to decay rapidly along the strip.

From these examples, it is seen that the FD-TD method plus the 3-D volumetric mesh generator will facilitate the modeling of volumetric composite materials by using the FD-TD technique. This approach is fairly accurate and versatile, and it can be applied to composite platforms such as helicopters.

E. FDTD Modeling of Pyramidal Horns With Composite E-plane Walls

The Contour-Path Finite-Difference Time-Domain (CPFDTD) method is getting more widespread attention since its introduction to the electromagnetics community [1], [2]. The CPFDTD method is suitable for modeling structures that cannot be gridized using the standard Yee's rectangular or cubic grid. The method modifies the grid near the surface of the curved structure only and retains its basic cubic grid in the remaining computational domain. The magnetic field components in the distorted grid are updated through modified equations that assume no field variation within the distorted area. The second-order accurate central difference approximations are, therefore, reduced to first-order approximations only at the grid points near the structure surface and retain their second-order accuracy elsewhere in the domain. Distorting the electric field contours is avoided by the method. The electric field points where necessary are obtained through a "near neighbor" approximation, i.e., if a field value is not available, the value of the field component closest to the component that is required is taken.

The CPFDTD approach presents an efficient and still accurate approach to extend the application of the conventional FDTD method to model smoothly curved surfaces.

1. Analysis of Pyramidal Horn Antennas

The application of the staircase FDTD method to model pyramidal horn antennas was reported in [3]. It was found that to obtain acceptable radiation patterns, compared to measured ones, grid sizes on the order of 30 cells per wavelength were required. It is demonstrated here that using the CPFDTD method with 12 cells per wavelength yields accurate antenna gain patterns. For this application, seventh-order accurate absorbing boundary conditions [4] were used.

The flared parts of the antenna surface are modeled by distorting the contours that update the magnetic field components next to the antenna surface. Distorting the electric field contours is avoided. In the E-plane direction the contours for the x and z components of the magnetic field are distorted to conform to the antenna surface. In the H-plane direction, the contours for the y and z components of the magnetic field are distorted.

Furthermore, modifications were made in the basic CPFDTD approach to include the effect of electrically thin (less than the size of the FDTD cell) magnetic coatings. When magnetic materials are applied in the E-plane walls of the pyramidal horn, diffractions from the antenna edges are reduced. This results in reduced side lobe levels in the backside of the antenna. Depending on the extent to which the E-plane wall is coated, nearly symmetric E-plane and H-plane antenna patterns can be obtained.

2. Numerical Results

Some of the computed antenna patterns that were obtained from a $5'' \times 5''$ square aperture pyramidal horn antenna and compare them with measurements. The geometry of the horn is shown in Fig. 26. The frequency of operation was 10 GHz. The aperture of the antenna was $5'' \times 5''$, whereas the waveguide aperture was of standard X-band dimensions, i.e., $0.9'' \times 0.4''$. The transition length from the waveguide aperture to the antenna aperture was $10.5''$. A section of $3''$ long composite material was then glued on the upper and lower E-plane walls as shown in Figure 26. The electrical param-

eters of the composite material were measured to be $\epsilon_r = 15.95 - j0.45$ and $\mu_r = 1.58 - j1.18$ and its thickness was 40 mils.

The grid size was 0.1″(about 12 cells per wavelength), i.e., the waveguide was 9x4 cells whereas the antenna aperture was 50x50 cells. The distance from the waveguide transition to the antenna aperture was 105 cells. Between the antenna and the outer boundary 14 cells were allowed. The overall grid size was 78x78x144 cells. The CPFDTD program was run for 40 cycles to reach steady state, on a RISC/6000. The CPU time was 4,200 seconds for obtaining the E-and H-plane gain patterns over 360° (at 1° steps). Figure 27 exhibits the computed E-plane gain pattern of the antenna without the presence of composite material and compares it with measurements. The agreement between the CPFDTD results and measurements is very good. Figure 28 compares the computed gain pattern in the H-plane with measurements.

Figure 29 compares the E-plane pattern of the same antenna with measurements when the lossy coating in the E-plane wall is applied. With the application of composite material the maximum gain at broadside is reduced by 1.6 dB, but the first side lobe in the pattern is eliminated. The side lobes in the backside of the antenna are also much lower with the composite wall.

F. Efficiencies of Horn Antennas Loaded with Composite Materials

The antenna patterns of a horn loaded with composite materials can be predicted by using the FD-TD method. In addition, the analysis of antenna efficiency can also be performed by using the same FD-TD technique. The approach to calculate the horn input power, E- and H-plane gain patterns, radiation power and antenna radiation efficiency is outlined and numerical results are presented.

1. Pyramidal Horn Antenna Input Power, E- and H-plane Gain Patterns, Radiated Power and Radiation Efficiency

The geometry of a partially coated pyramidal horn is already shown in Fig. 26. A section of composite material of thickness t and length l_m is placed on the upper and lower E-plane walls of the horn for pattern control

purposes. The effect of the lossy material on the antenna performance is analyzed in this section.

The pyramidal horn was fed by a rectangular waveguide operating in the dominant TE_{10} mode whose tangential electric field at the aperture is represented by

$$E_y(x,y,z) = E_0 \sin(\frac{\pi}{a}x)\sin(\omega t - \beta_z z) \tag{4}$$

where $0 \leq x \leq a$ and $0 \leq y \leq b$. The constant β_z represents the waveguide propagation constant. At the reference feed plane, $\beta_z z$ was set to zero.

Using this feed scheme, the input power to the horn was estimated by integrating the input power density over the waveguide cross section, and it is given by

$$P_{10}^{input} = \frac{1}{2}E_0^2\left(\frac{\beta_z}{\omega\mu_0}\right)\left(\frac{ab}{2}\right) \tag{5}$$

The radiated far-zone E_θ and E_ϕ electric fields are obtained from the FDTD code through a near-to-far field transformation. The E-plane gain pattern was calculated using

$$G_E\left(\theta, \phi = 90°\right) = \frac{4\pi E_\theta^2\left(\theta, \phi = 90°\right)}{P_{10}^{input}} \tag{6}$$

Similarly, the H-plane gain pattern was calculated using

$$G_H\left(\theta, \phi = 0°\right) = \frac{4\pi E_\phi^2\left(\theta, \phi = 0°\right)}{P_{10}^{input}} \tag{7}$$

The antenna radiated power was estimated by integrating the far-zone fields over a sphere, and it is represented by:

$$P^{rad} = \int_0^\pi \int_0^{2\pi} U(\theta,\phi)\sin\theta d\theta d\phi \tag{8}$$

where $U(\theta,\phi)$ is the radiation intensity and is given by

$$U(\theta,\phi) = \frac{1}{2\eta_0}[\mid E_\theta(\theta,\phi)\mid^2 + \mid E_\phi(\theta,\phi)\mid^2] \tag{9}$$

where $\eta_0 = 120\pi$ is the free-space impedance. One important design parameter of pyramidal horns with lossy materials on the E-plane walls is the power loss or the antenna efficiency calculated using

$$\eta = \frac{P^{rad}}{P_{10}^{input}} \tag{10}$$

2. Numerical Results

A 20-dB standard gain pyramidal horn antenna with conducting inner walls was analyzed using the contour path FDTD method. Figs. 30 and 31 compare the computed E- and H-plane gain patterns, respectively, of the pyramidal horn with measurements. As illustrated by both figures, there is very good agreement between the computed and measured results over a dynamic range of 60 dB. The computed gain patterns agree very well with the measured ones when a standard cell size of $\lambda/12$ was used (0.1″). The overall FDTD grid required for this problem was $76 \times 60 \times 142$ cells. This simulation was run for 40 cycles to reach steady state and took about 2,500 seconds on an IBM-RISC/6000 computer for computing the E- and H-plane gain patterns over 360° at 1° steps.

The antenna radiation efficiency for the pyramidal horn with conducting walls was estimated by integrating the far-zone fields to obtain the radiated power. The amplitude of the y-directed electric field was set equal to $E_0 = 1$ V/m producing a reference input power of $P_{10}^{input} = 0.116226 \times 10^{-6}$ Watts. By evaluating the far fields and then integrating them (1° step), the radiated power was estimated to be $P^{rad} = 0.115077 \times 10^{-6}$ watts. The corresponding antenna radiation efficiency was $\eta = 0.99011 \simeq 99\%$. Therefore, most of the input power is radiated except for a small portion which is reflected back into the antenna.

For pattern control purposes, sections of ECCOSORB GDS composite material, with measured electrical parameters $\epsilon_r = 14.9 - j0.25$ and $\mu_r = 1.55 - j1.45$ at 10 GHz, were placed on the inner E-plane walls of the horn as illustrated in Fig. 26. The nominal thickness of the composite material section was t = 30 mil (0.0762cm). The material thickness, however, was measured to be t = 33 mil (0.08382cm).

For the FDTD simulations a grid size of 0.1″ was used. The material thickness was about a third of the FDTD cell. The composite material sections influence mainly the E-plane pattern. Thus, only results from the E-plane gain pattern calculation of the coated 20-dB standard gain horn are presented. Fig. 32 compares the FDTD computed results with measurements, when a 2″ section of composite material was used. The agreement between the computed and measured results is good. As illustrated in the figure, the first side lobe of the pattern is eliminated. Because of the presence of the material in the inner walls, the broadside antenna gain was reduced

by 2.69 dB. In this case the antenna radiated power was estimated to be $P^{rad} = 0.0886980 \times 10^{-6}$ watts, resulting in an antenna efficiency of $\eta = 0.7631493 \simeq 76.3\%$. The reduced antenna efficiency in this case is due to the power dissipated in the 2″ section of lossy magnetic material.

Fig. 33 compares the computed and measured E-plane patterns when a section of 4″ GDS material is used for coating the E-plane walls of the 20-dB standard gain horn. As illustrated in the figure, good agreement between the computed and measured gain patterns is obtained in this case also. With 4″ of GDS material the second side lobe in the pattern is almost eliminated. However in this case, the broadside gain is reduced by 4.98 dB. The radiation efficiency was reduced to $\eta = 0.63870 \simeq 63.9\%$. In this case a significant amount of power is dissipated in the lossy magnetic material.

Fig. 34 compares the FDTD computed gain pattern with measurements when a section of 66 mil thick and 2″ long GDS material is used for coating the E-plane walls of the 20-dB standard gain pyramidal horn. In this case two sections of 33 mil GDS material were glued together to form a 66 mil section. As illustrated in the figure, good agreement between the computed and measured gain patterns is obtained in the main lobe. There are, however, some differences between the computed and measured results in the side lobes of the pattern. With the 66 mil section of GDS material the broadside gain of the pattern is reduced by 2.64 dB. The antenna radiation efficiency in this case was estimated to be $\eta = 0.70004 \simeq 70.0\%$.

The FDTD results of the broadside gain and efficiency calculations for the different antenna geometries are summarized in Table 1.

Table 1: Broadside gain and radiation efficiency of a 20-dB standard gain horn at 10 GHz, partially coated with composite material.

Antenna type	$G_E(\theta = 0°, \phi = 90°)$ dB	Efficiency, η
Conducting walls	20.65	0.99011
GDS material, $l_m = 2''$, t = 33 mil	17.96	0.76315
GDS material, $l_m = 4''$, t = 33 mil	15.67	0.63870
GDS material, $l_m = 2''$, t = 66 mil	18.01	0.70004

To examine the effect of material thickness and length on the antenna radiation pattern, the broadside gain loss of the 20-dB standard gain horn was

calculated for different GDS material thickness and lengths. The variation of the broadside antenna gain loss versus the GDS material thickness, for different material lengths, is illustrated in Fig. 35. As illustrated in the figure the broadside antenna gain loss is largest for thickness in the range of 25 - 30 mil, and decreases for larger material thickness. Thus thickness range is not strongly influenced by the material length.

G. Future Work

Future work in this area will be directed toward modeling of complex structures by using FDTD technique plus the auto-mesh generation capability. Since FD-TD technique can model different materials in the computation domain in a unified way, it will be the primary vehicle to be used for solving complex composite geometries. In the meanwhile, the surface impedance approach will be coupled with other EM codes (NEC, ESP and FERM) to model thin dielectric and coated metallic geometries.

To facilitate composite material modeling, the two approaches (FD-TD and surface impedance) will be integrated into the GEOM code. Thus the GEOM can be used as a preprocessor to provide appropriate grids or meshes for a given complex geometry.

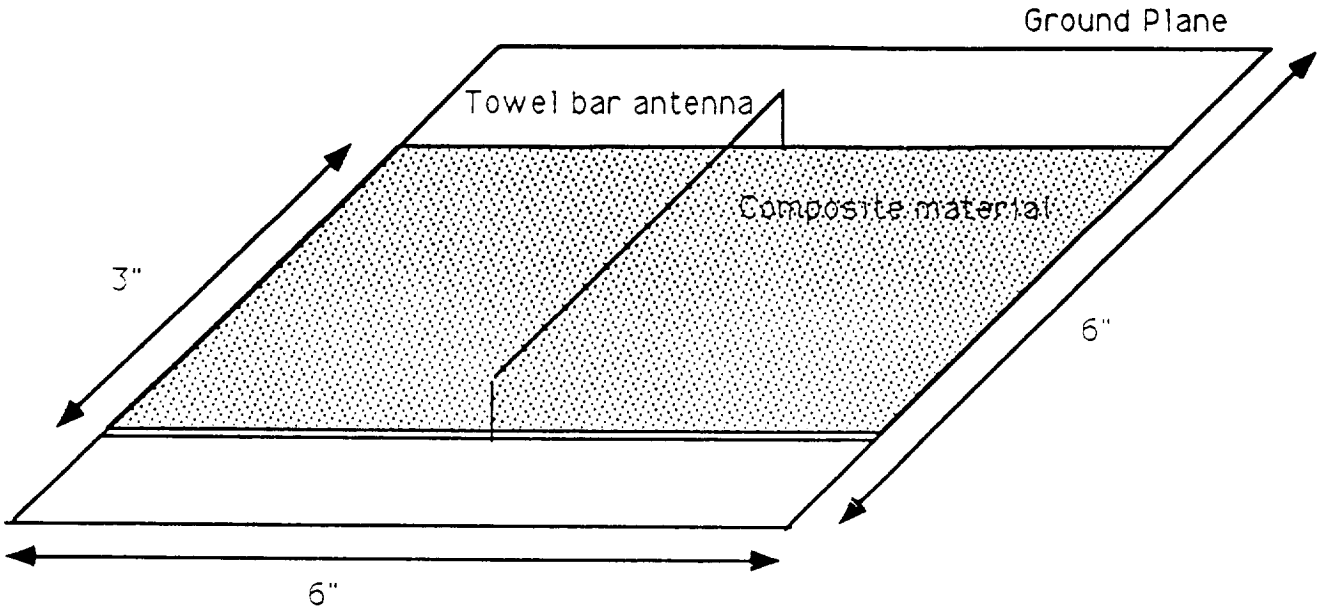

Figure 1: Geometry of a towel-bar antenna mounted on a composite material-coated plate

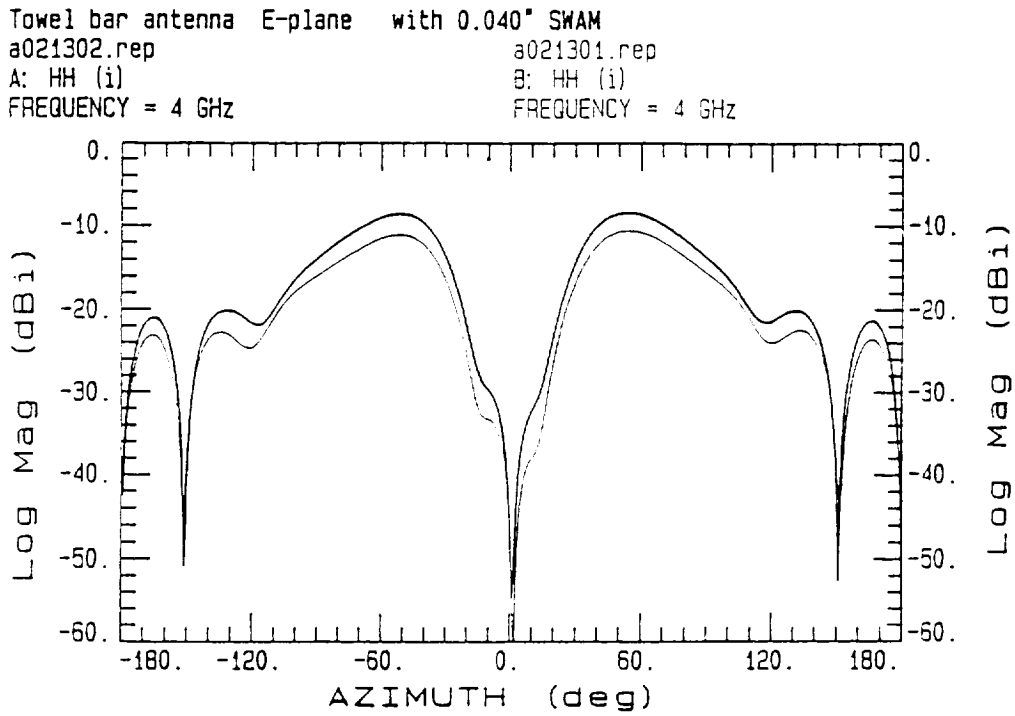

Figure 2: Measured yz-plane plane pattern of the towel bar antenna on composite materials at 4 GHz

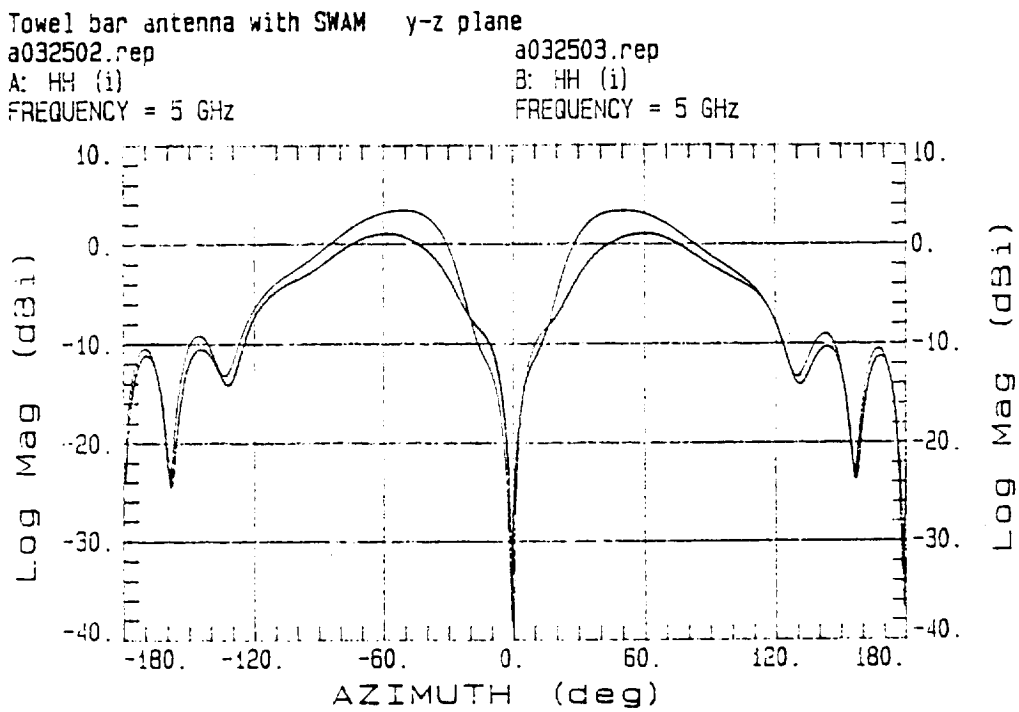

Figure 3: Measured yz-plane plane pattern of the towel bar antenna on composite materials at 5 GHz

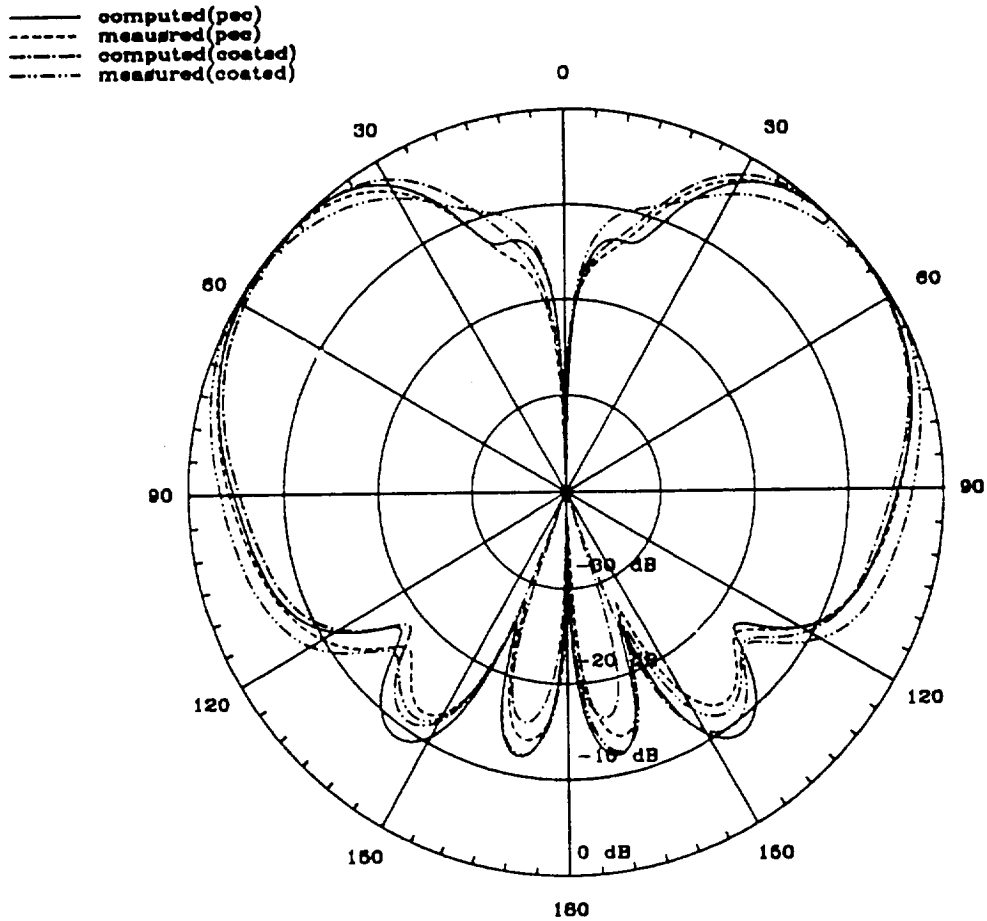

Figure 4: Predicted and measured radiation pattern of the towel-bar antenna in yz plane (the plane perpendicular to both the towel-bar plane and the ground plane).

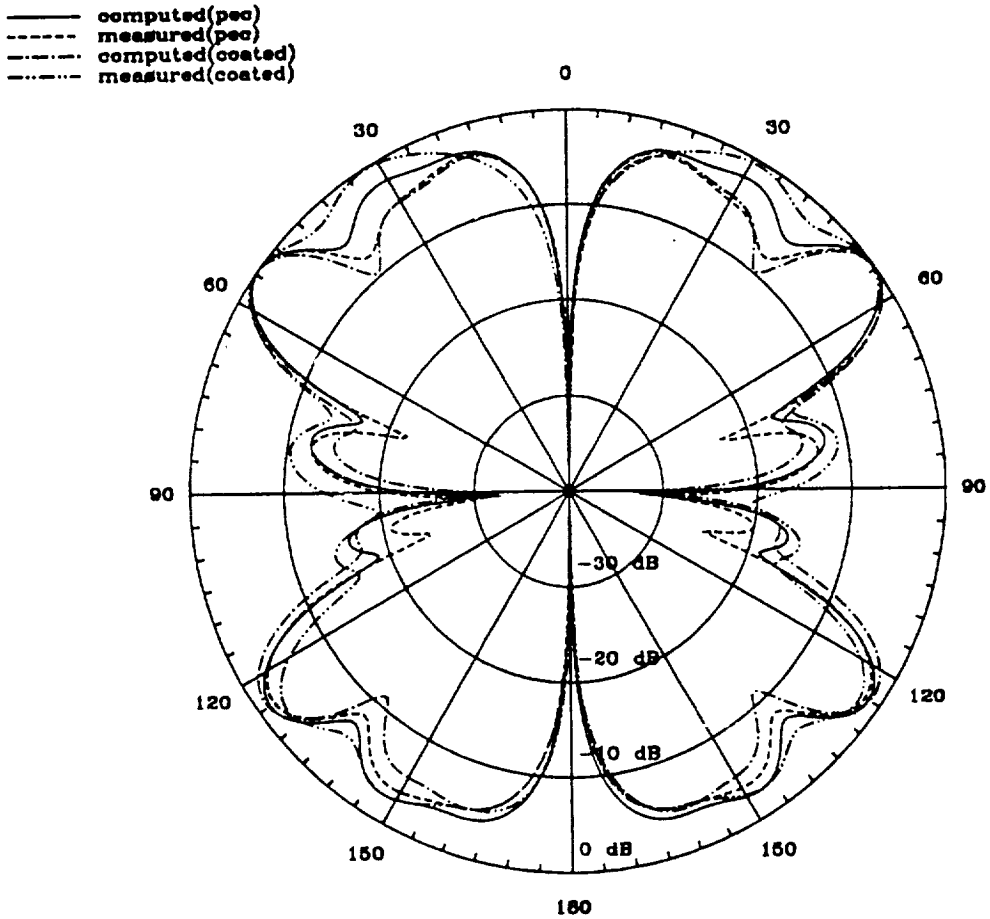

Figure 5: Predicted and measured radiation pattern of the towel-bar antenna in xy plane (the ground plane).

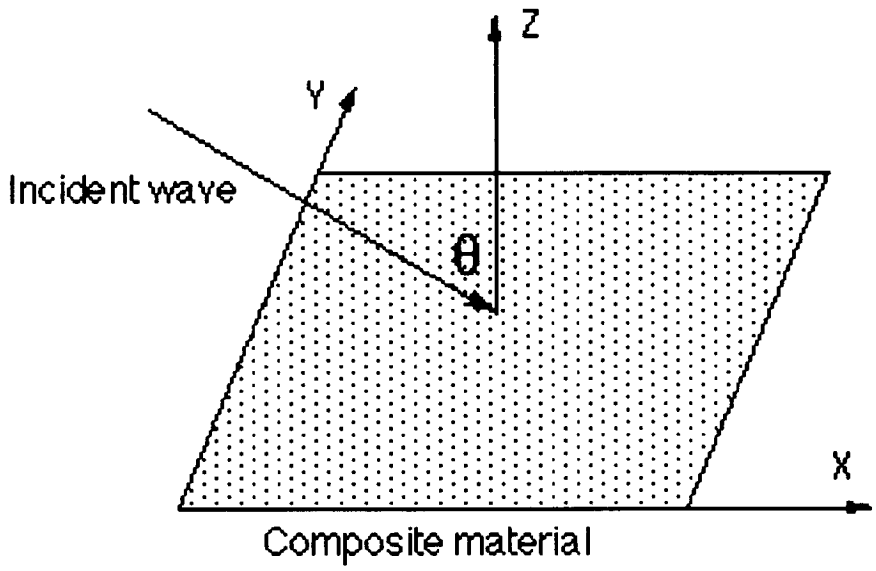

Figure 6: The geometry used to compute current distribution on a $\lambda/2 \times \lambda/2$ composite plate.

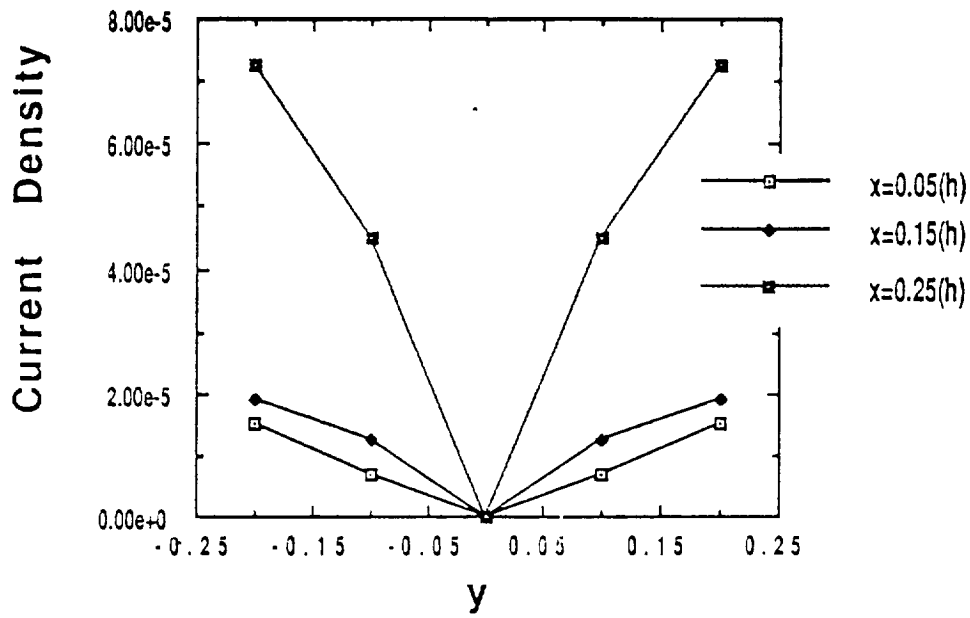

Figure 7: Current distribution along constant x lines. Hard polarization.

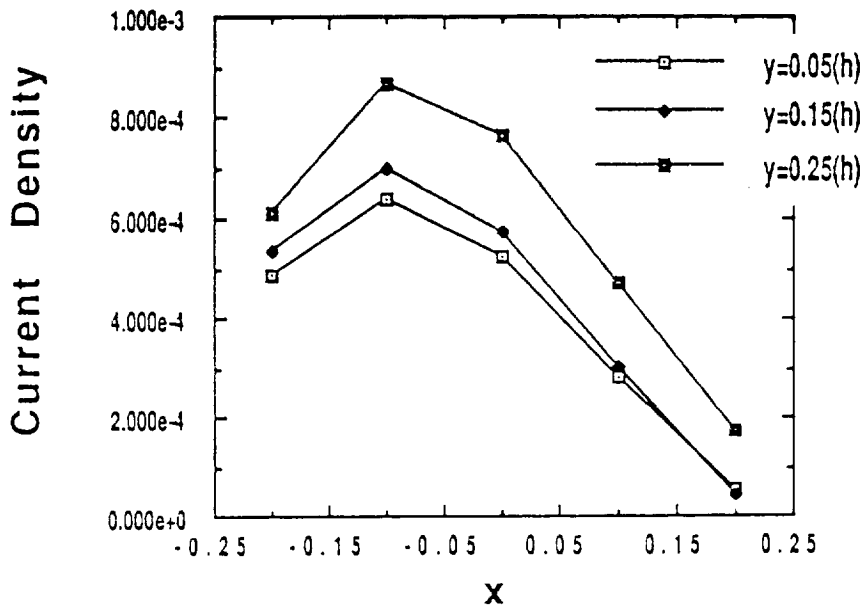

Figure 8: Current distribution along constant y lines. Hard polarization.

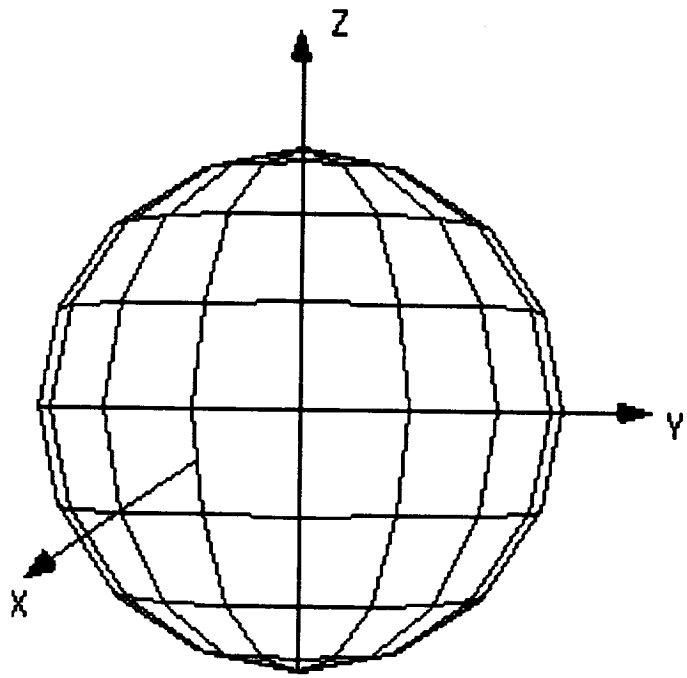

Figure 9: The geometry of a dielectric sphere with radius of 0.5λ.

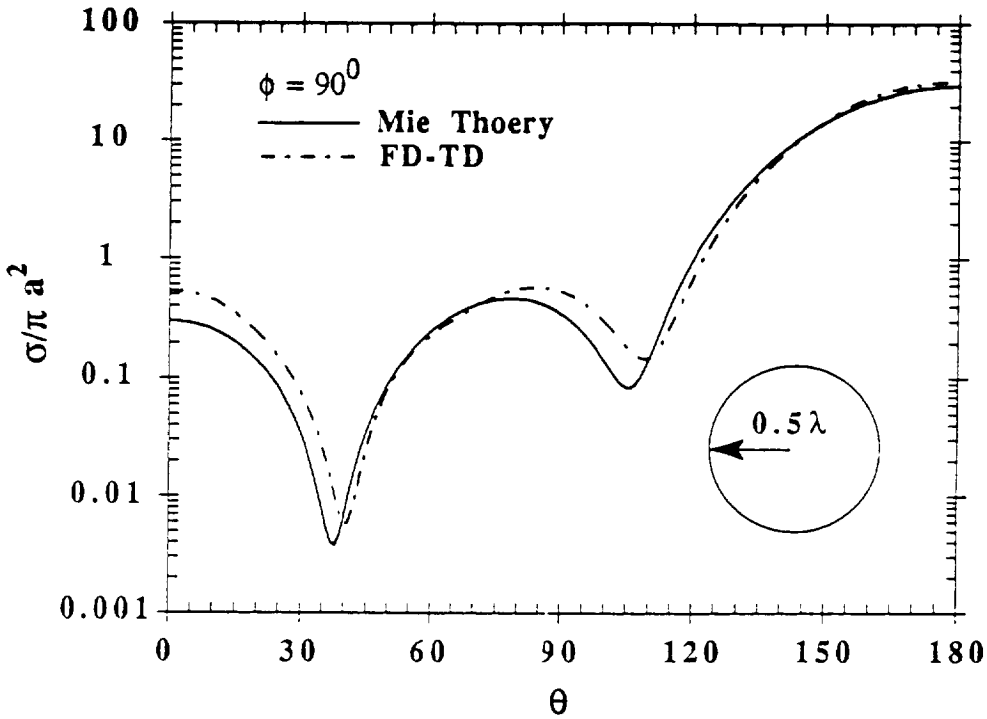

Figure 10: RCS of a dielectric sphere in the plane of $\phi = 90^0$. (ϵ_r=2.0 - j0.06)

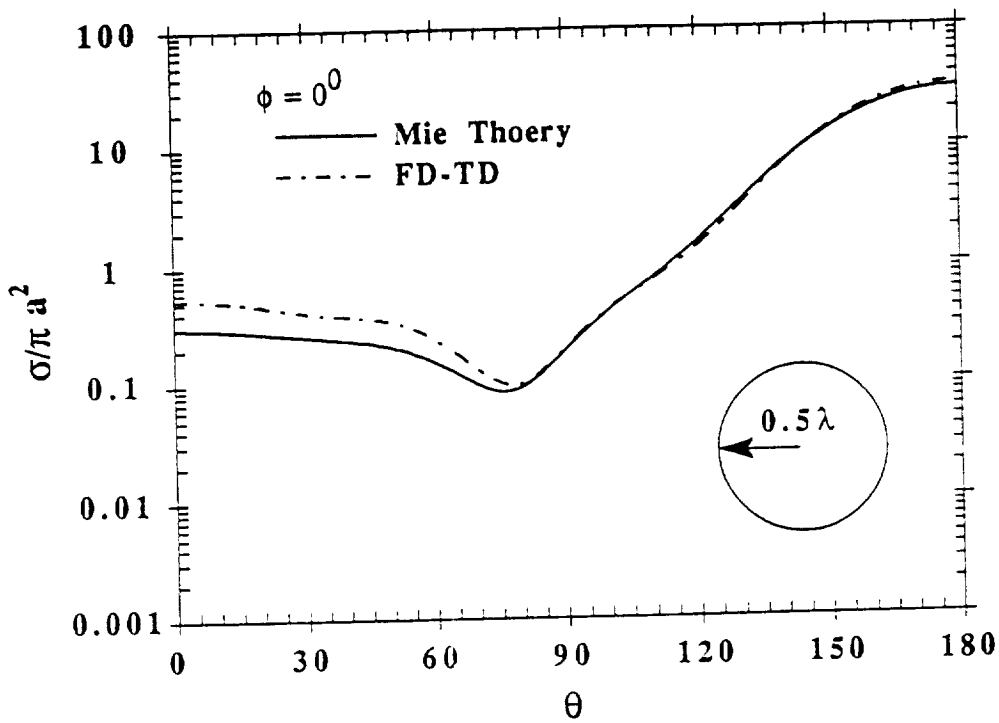

Figure 11: RCS of a dielectric sphere in the plane of $\phi = 0^0$. (ϵ_r=2.0 - j0.06)

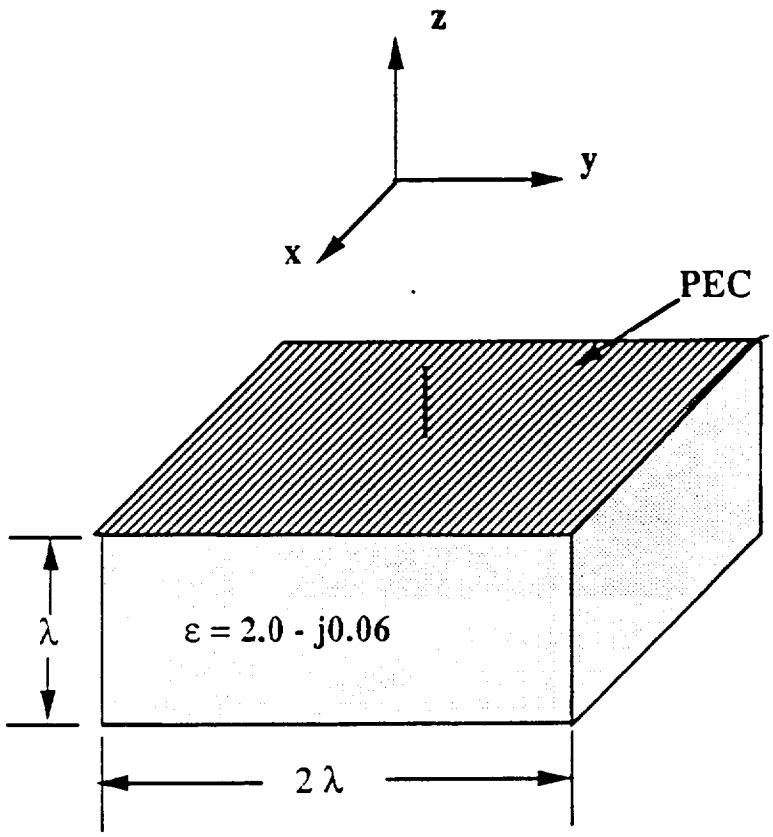

Figure 12: Geometry of a monopole grounded with PEC and dielectric substrate.

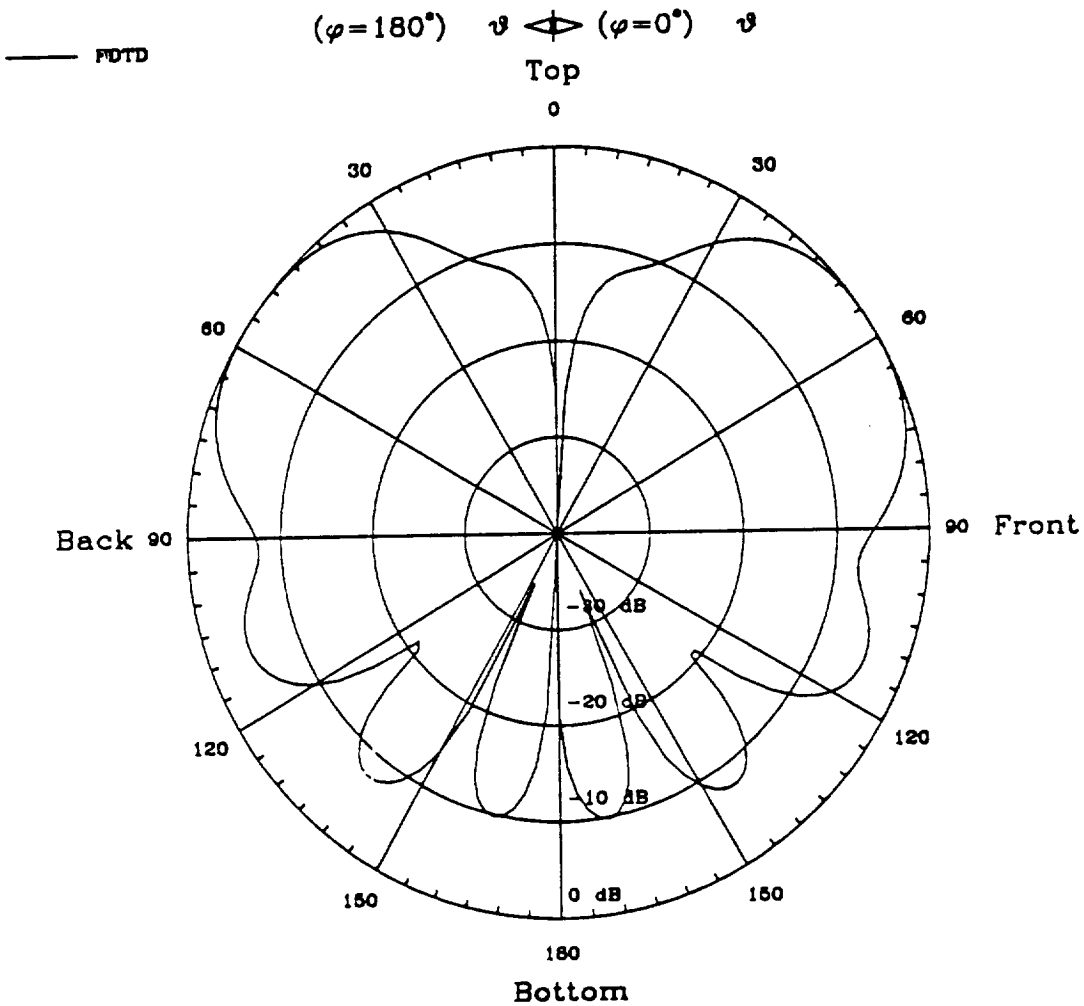

Figure 13: XZ-plane radiation pattern of a monopole grounded with PEC and dielectric substrate.

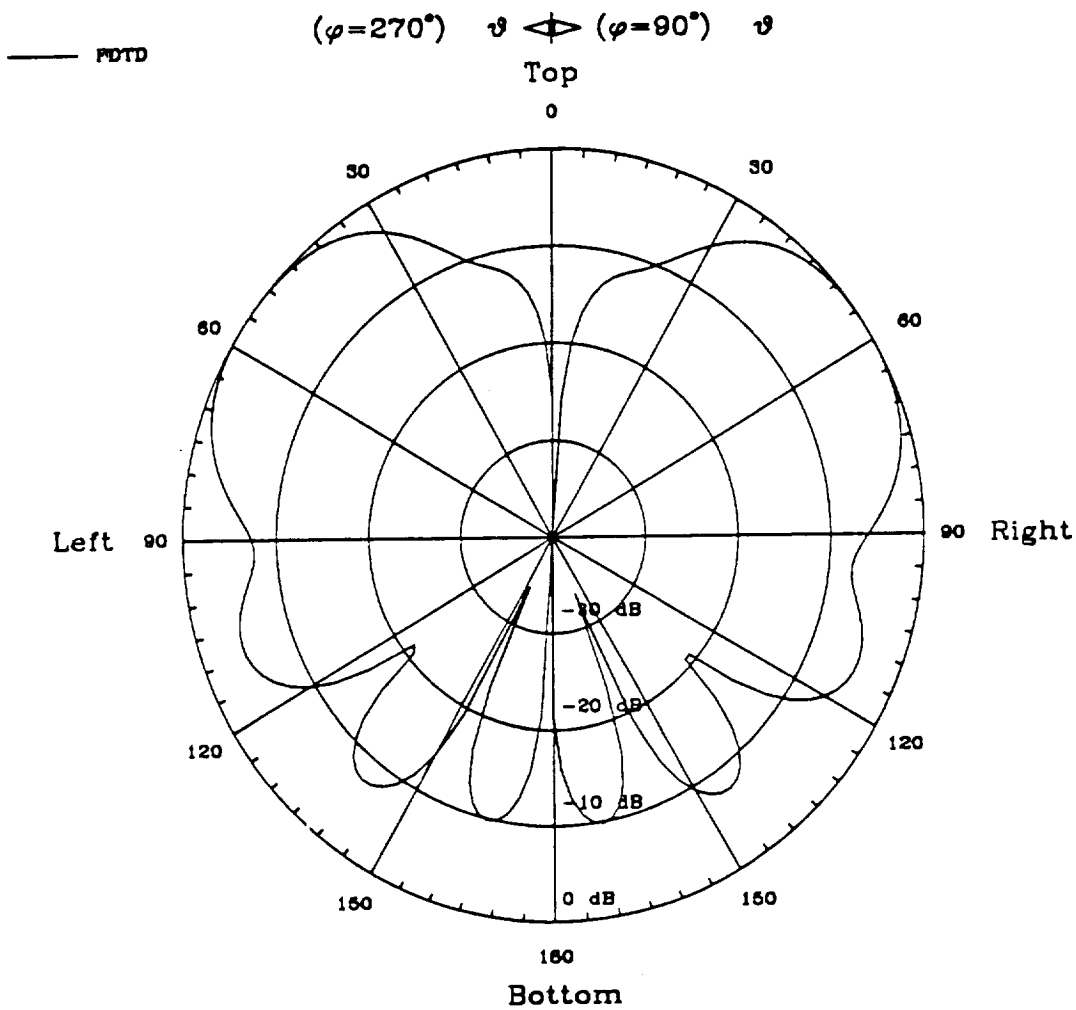

Figure 14: YZ-plane radiation pattern of a monopole grounded with PEC and dielectric substrate.

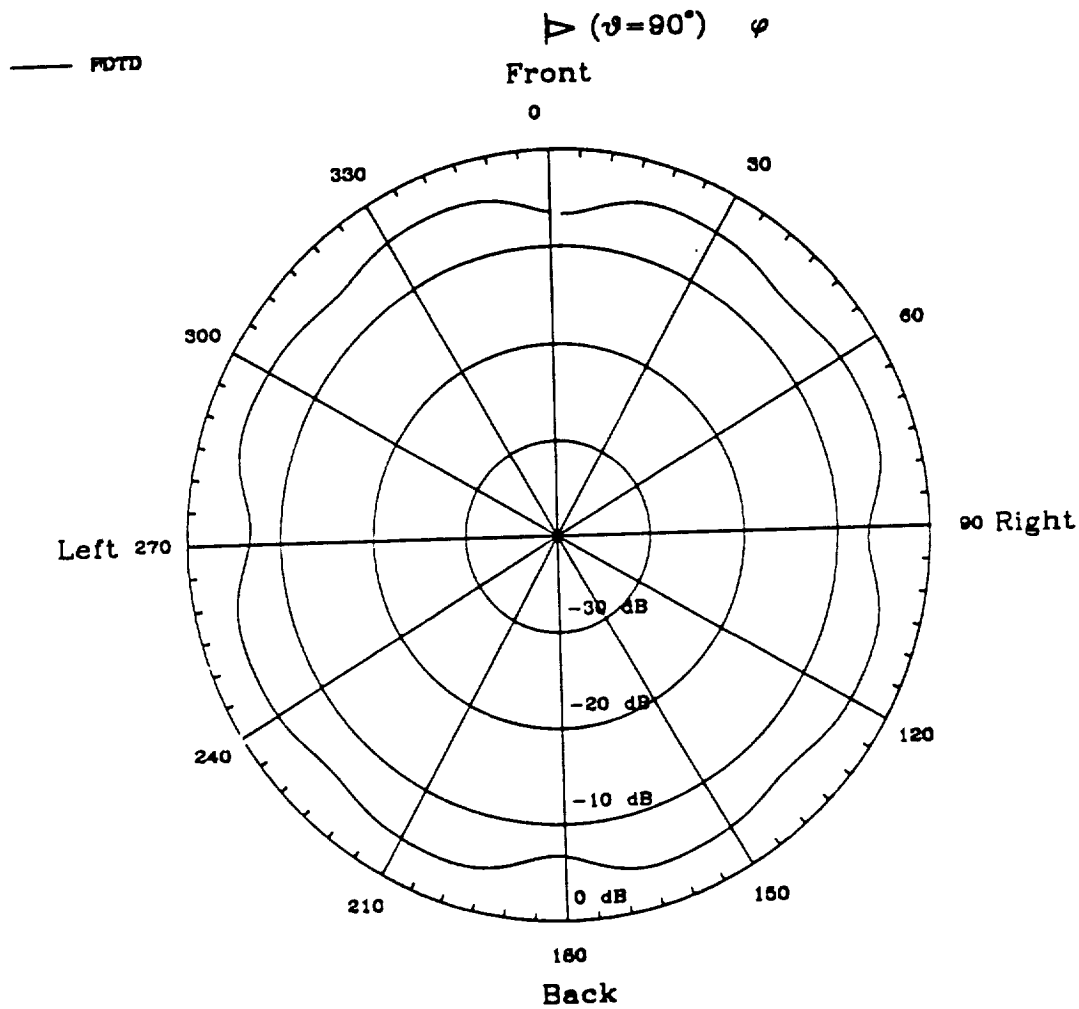

Figure 15: XY-plane radiation pattern of a monopole grounded with PEC and dielectric substrate.

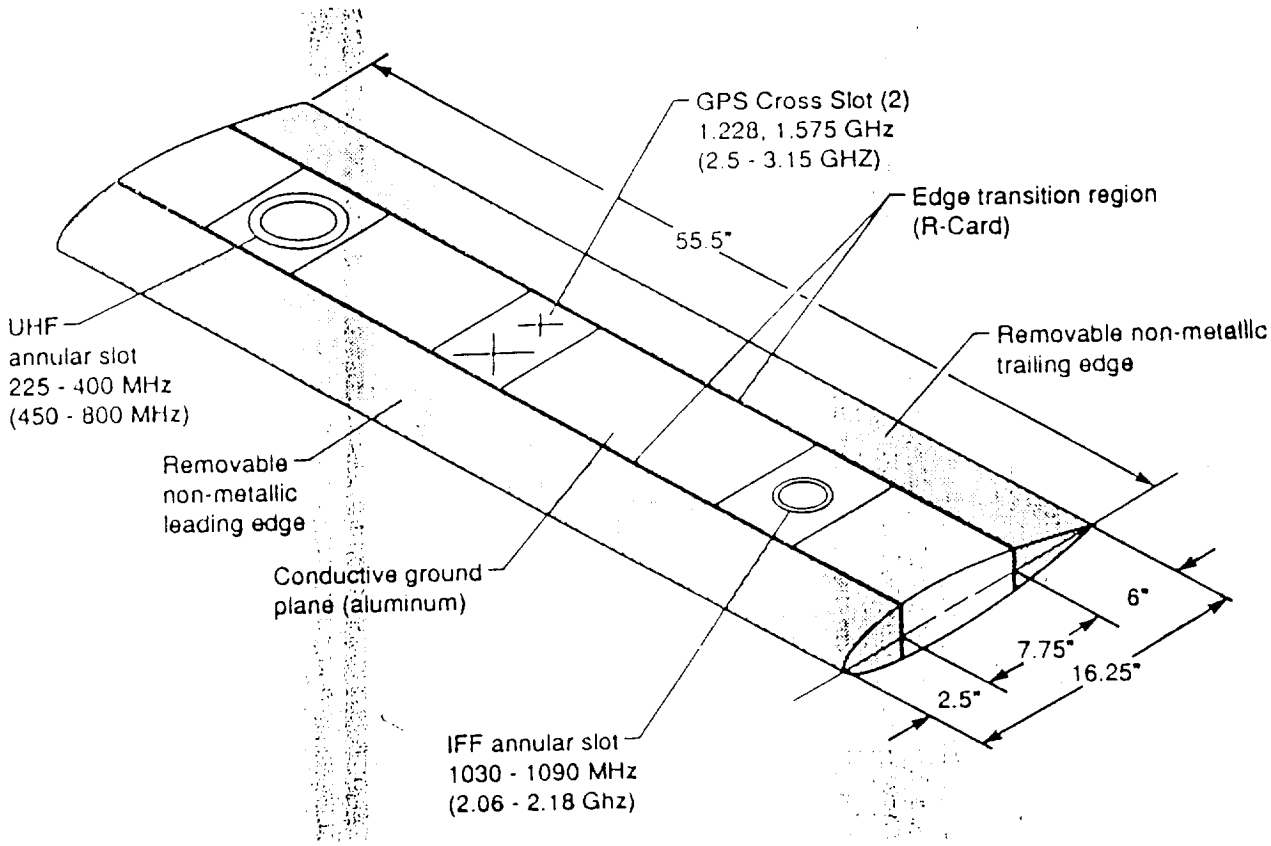

Figure 16: The original geometry of a scaled Comanche tail stalilizer.

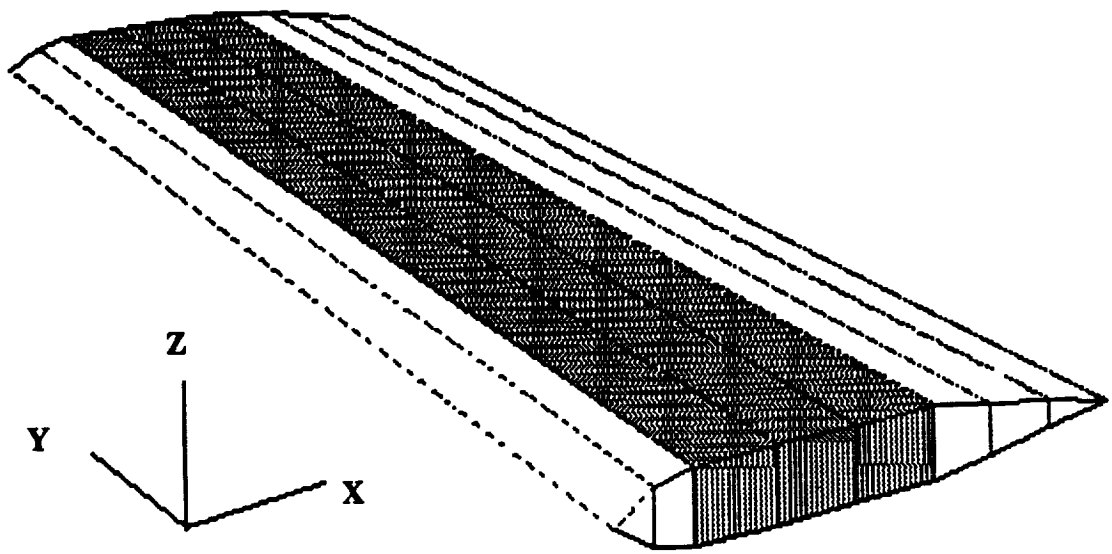

Figure 17: Solid surface model of the scaled Comanche stabilizer.

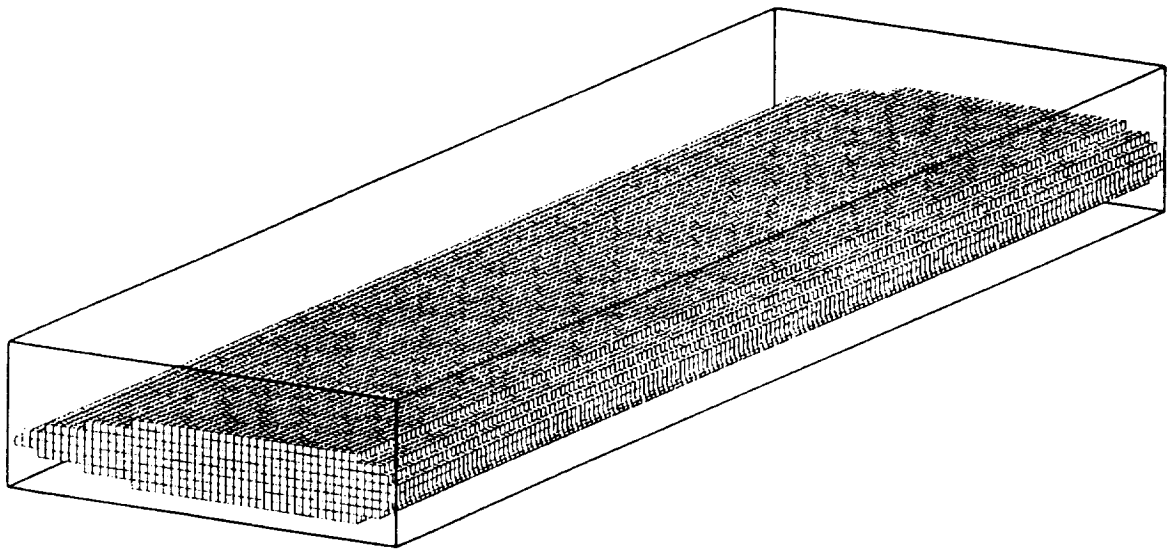

Figure 18: Volumetric FDTD mesh used to model the Comanche stabilizer.

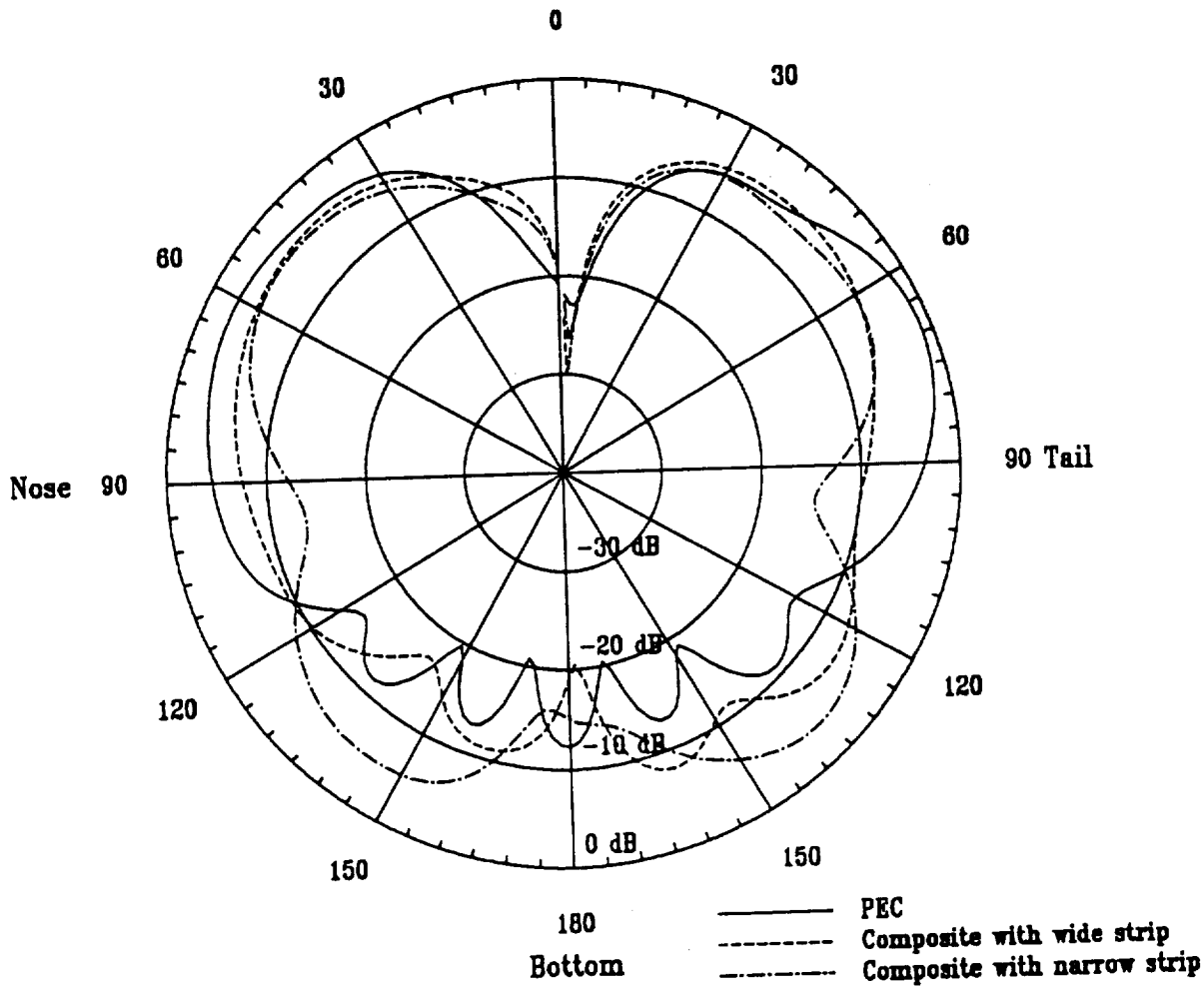

Figure 19: XZ-plane power radiation pattern of a monopole mounted on the stabilizer (solid line – all-metallic stabilizer; dashed line – stabilizer with 7.5" wide metal strip; dot-dashed line – stabilizer with 2.5" wide metal strip).

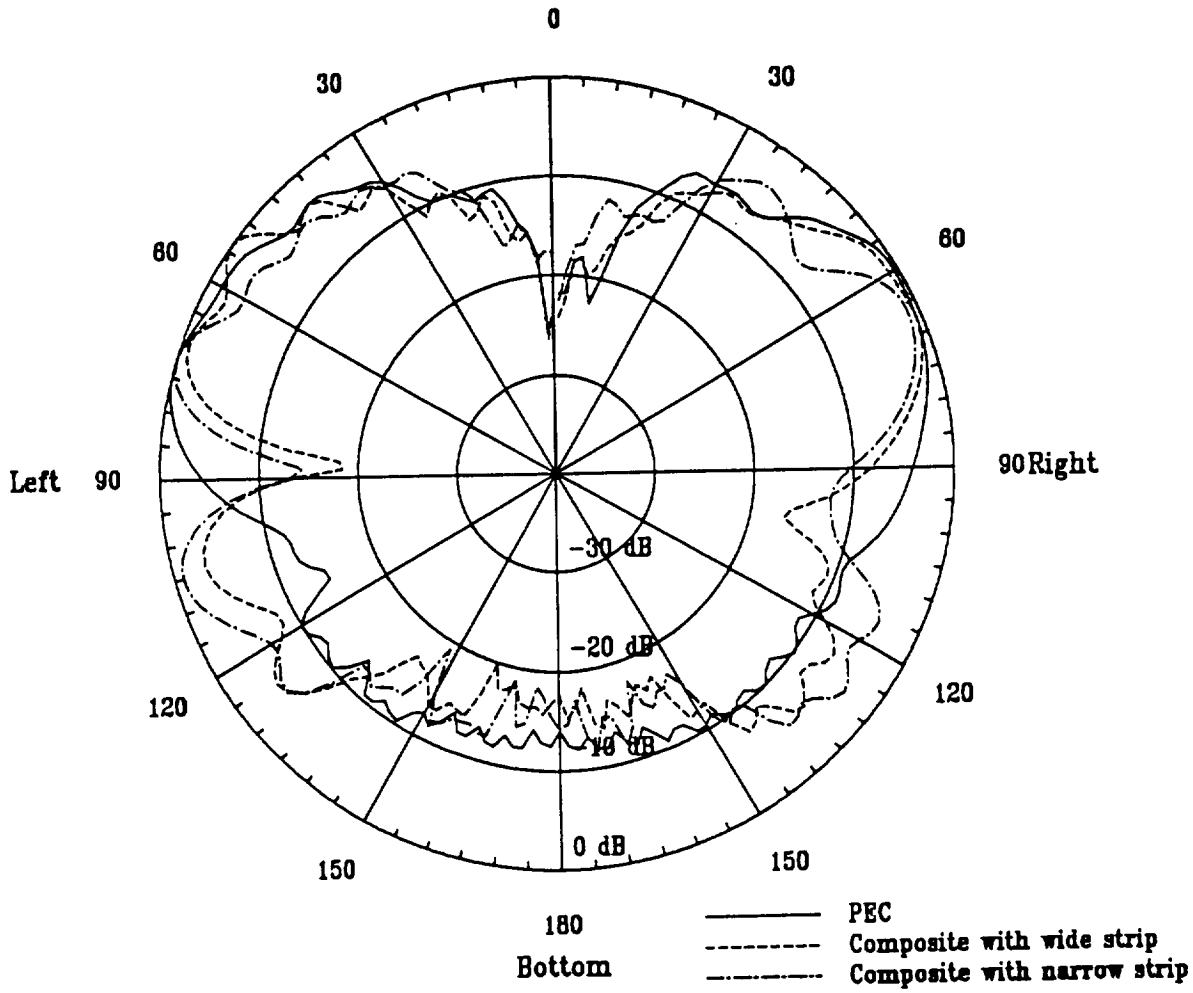

Figure 20: YZ-plane power radiation pattern of a monopole mounted on the stabilizer (solid line – all-metallic stabilizer; dashed line – stabilizer with 7.5" wide metal strip; dot-dashed line – stabilizer with 2.5" wide metal strip).

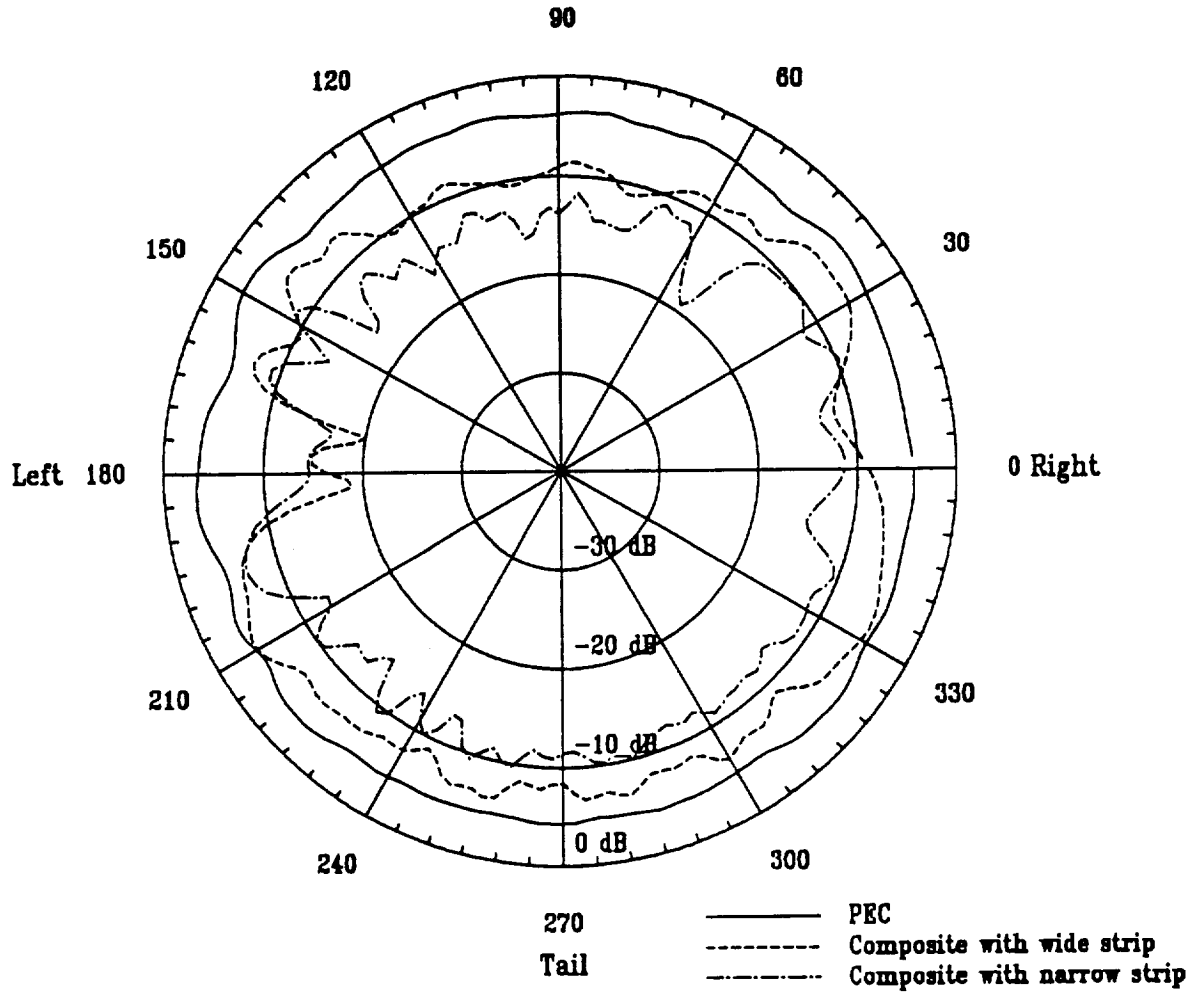

Figure 21: XY-plane power radiation pattern of a monopole mounted on the stabilizer (solid line – all-metallic stabilizer; dashed line – stabilizer with 7.5" wide metal strip; dot-dashed line – stabilizer with 2.5" wide metal strip).

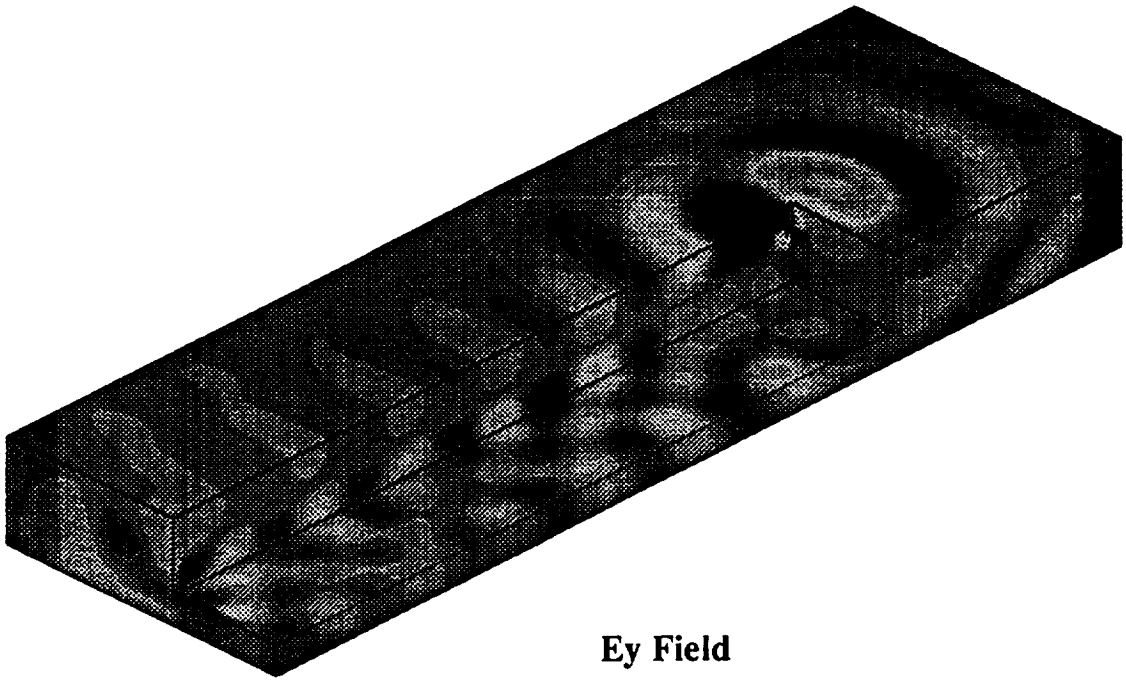

Figure 22: E_y field distribution inside and around the Comanche stabilizer (with 7.5" wide metal strip and $\epsilon_r = 3.0 - j1.0^{-5}$).

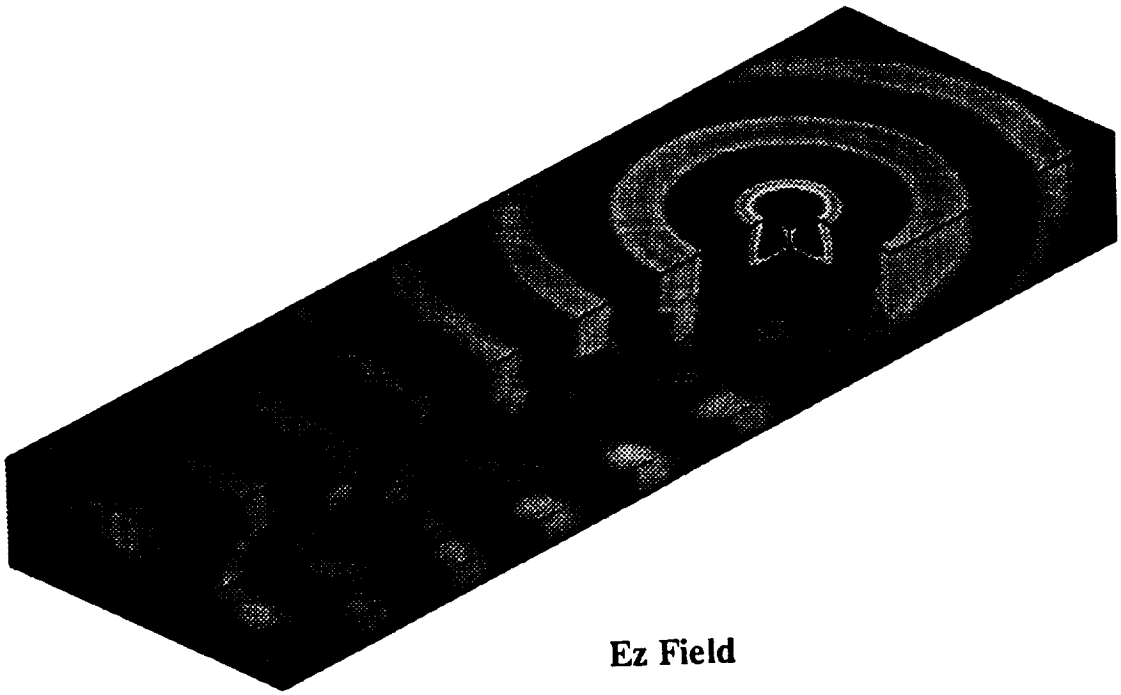

Figure 23: E_z field distribution inside and around the Comanche stabilizer (with 7.5" wide metal strip and $\epsilon_r = 3.0 - j1.0^{-5}$).

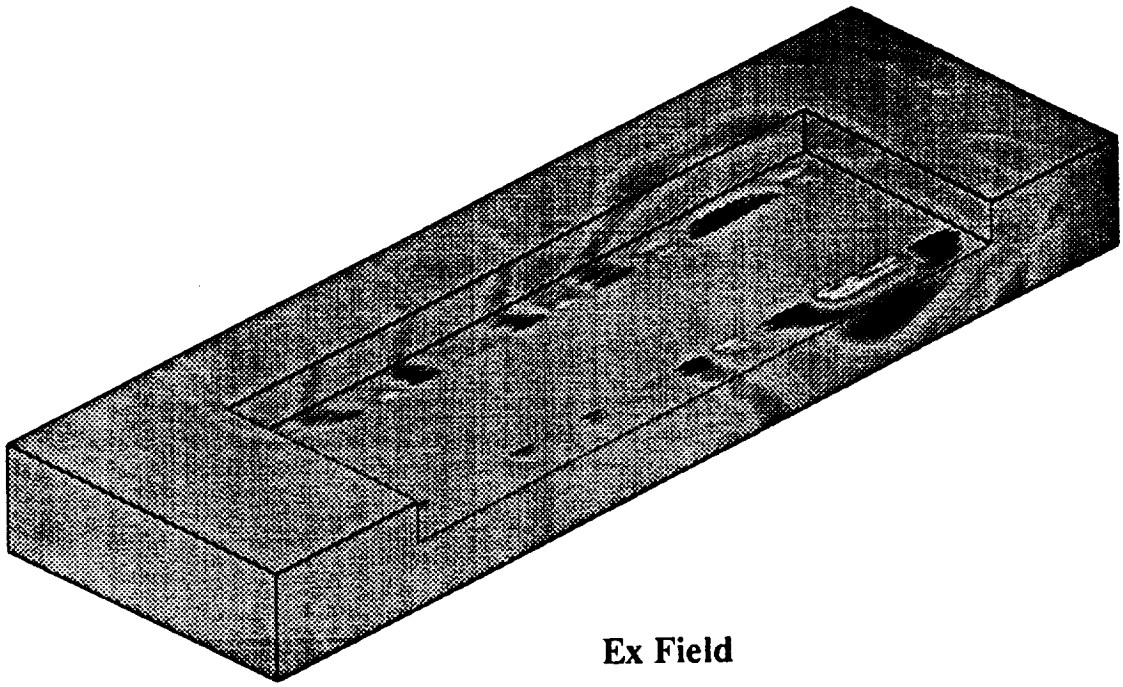

Figure 24: E_x field distribution on and around the metal strip of the stabilizer (with 7.5" wide metal strip and $\epsilon_r = 3.0 - j1.0^{-5}$).

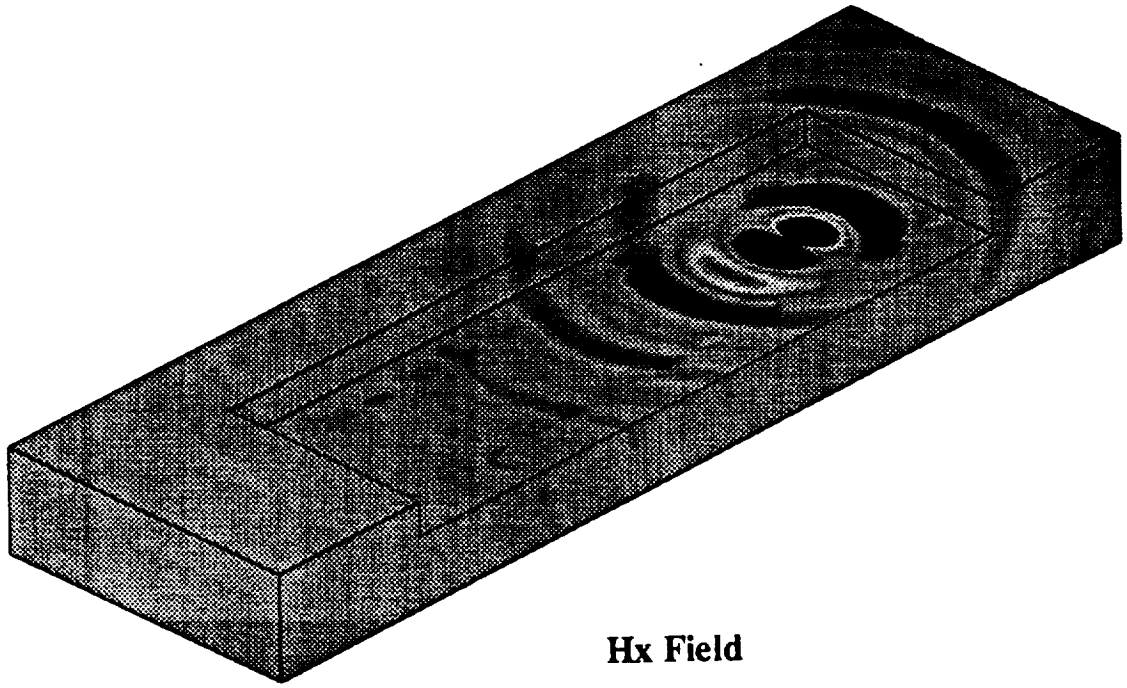

Figure 25: H_x field distribution on and around the metal strip of the stabilizer (with 7.5" wide metal strip and $\epsilon_r = 3.0 - j1.0^{-5}$).

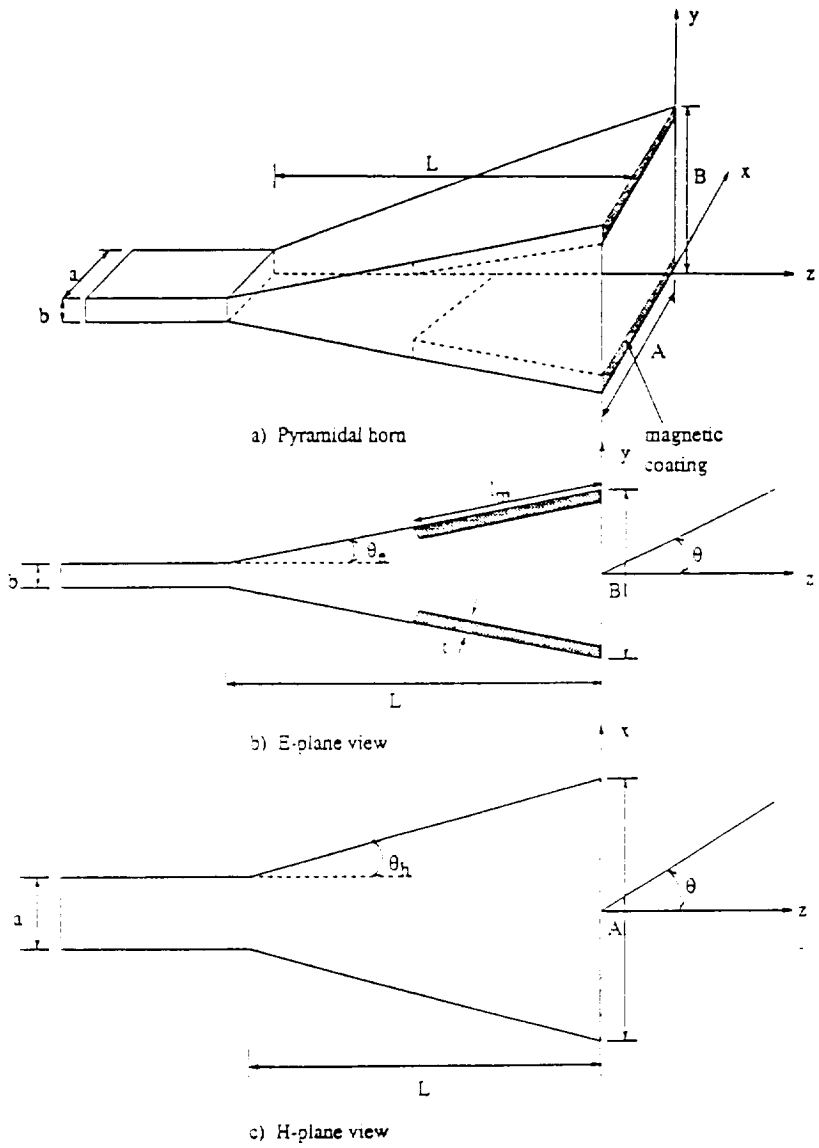

Figure 26: Geometry of a pyramidal horn antenna with composite E-plane walls.

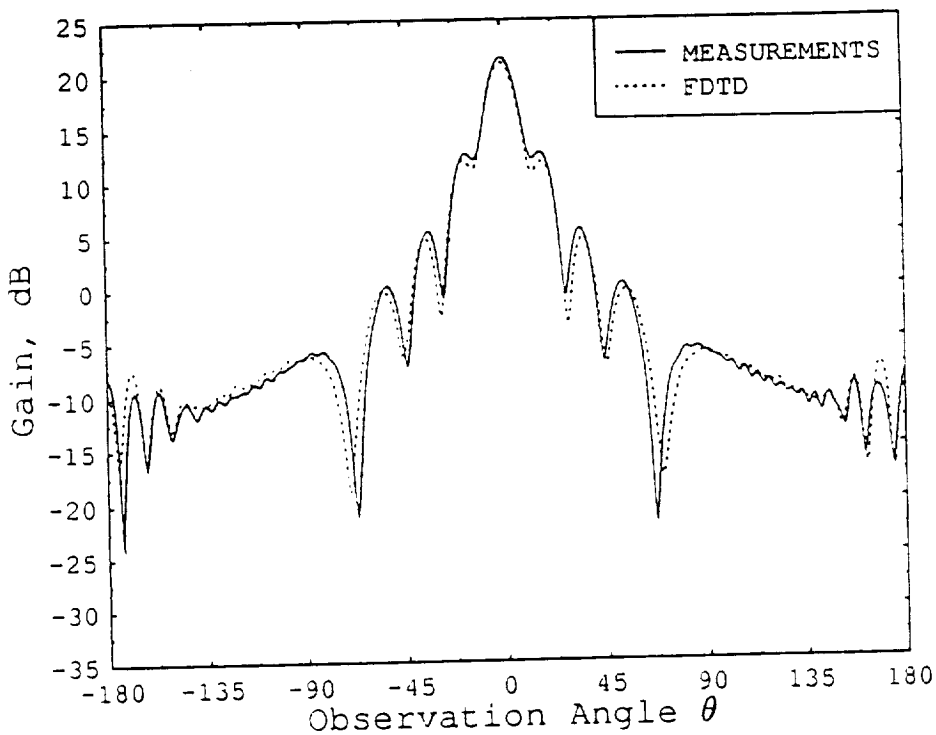

Figure 27: E-plane gain pattern of a square aperture pyramidal horn at 10.0 GHz. The antenna size was $A = 5''$, $B = 5''$, $L = 10.5''$, $a = 0.9''$ and $b = 0.4''$.

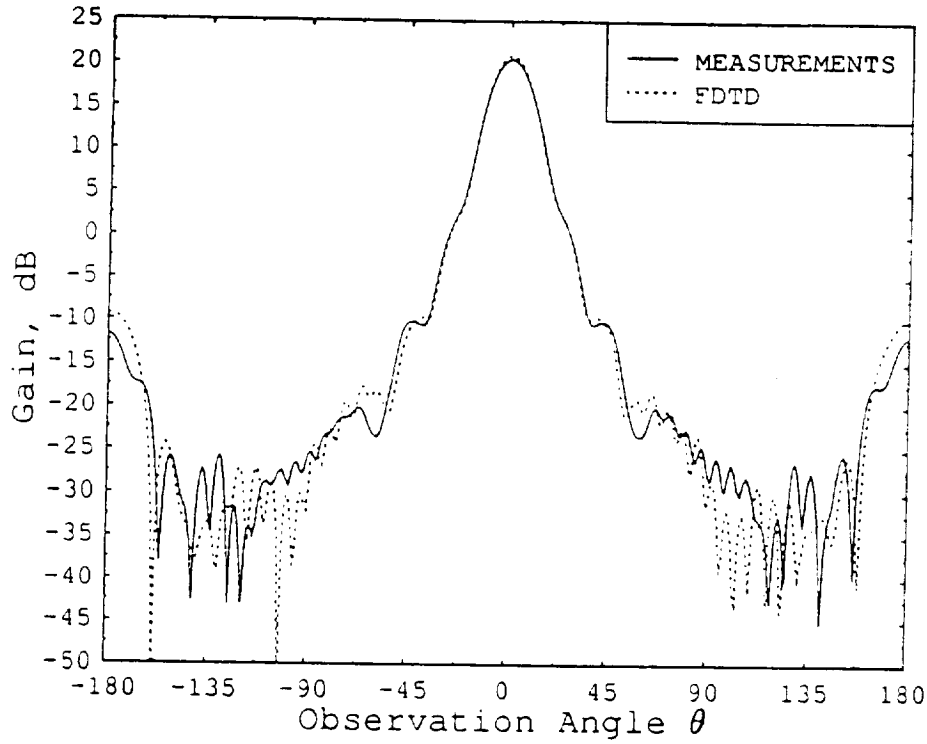

Figure 28: H-plane gain pattern of a square aperture pyramidal horn at 10.0 GHz. The antenna size was $A = 5''$, $B = 5''$, $L = 10.5''$, $a = 0.9''$ and $b = 0.4''$.

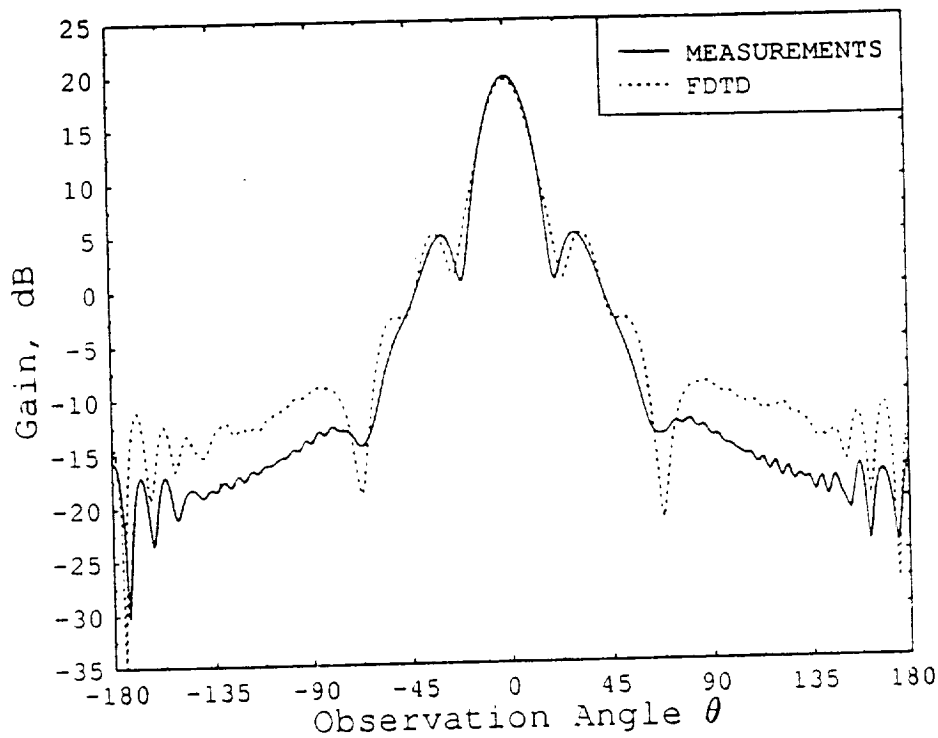

Figure 29: E-plane gain pattern of a square aperture pyramidal horn with composite E-plane walls at 10.0 GHz. The antenna size was $A = 5''$, $B = 5''$, $L = 10.5''$, $a = 0.9''$ and $b = 0.4''$. The parameters of the composite material were $l_m = 3''$, $t = 0.040''$, $\epsilon_r = 15.95 - j0.45$ and $\mu_r = 1.58 - j1.18$.

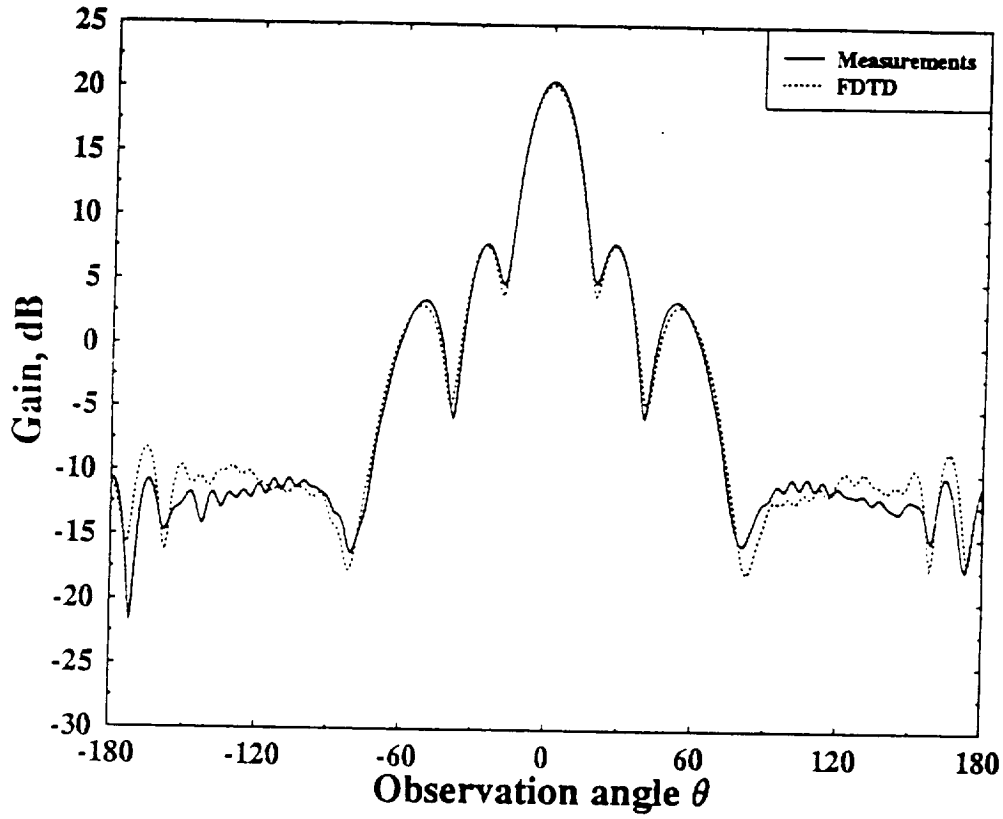

Figure 30: E-plane gain of a 20-dB standard gain pyramidal horn with conducting walls at 10.0 GHz (A = 4.87″, B = 3.62″, L = 10.06″, a = 0.9″ and b = 0.4″).

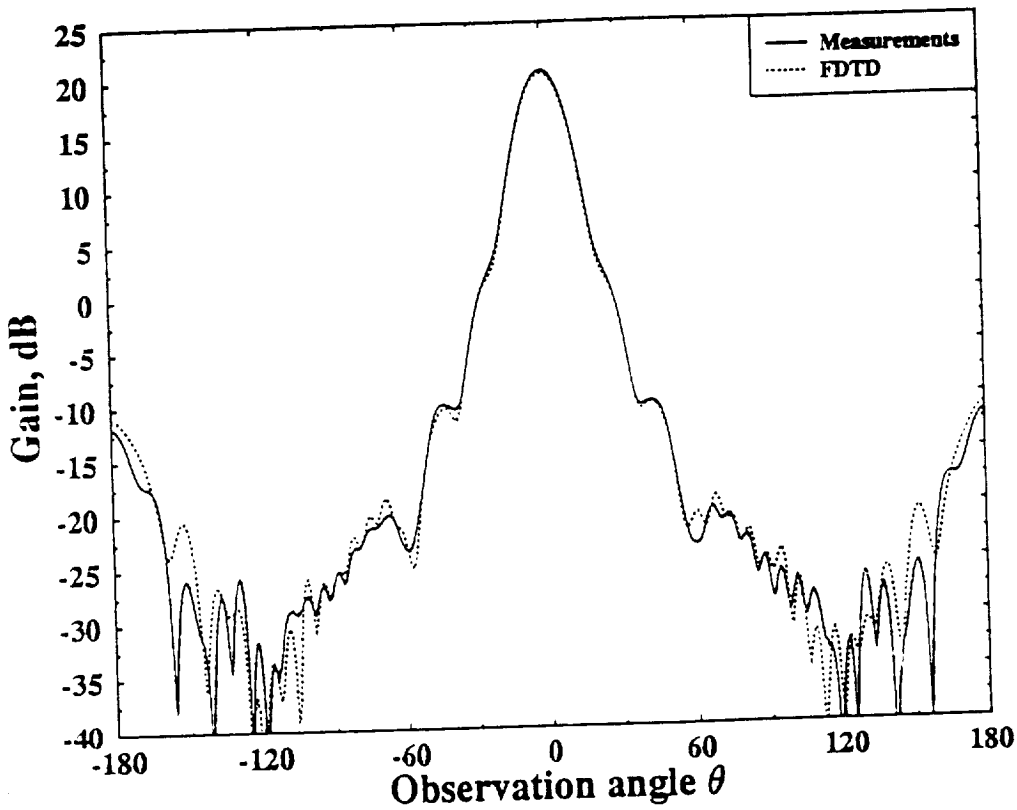

Figure 31: H-plane gain of a 20-dB pyramidal standard gain horn with conducting inner walls at 10.0 GHz.

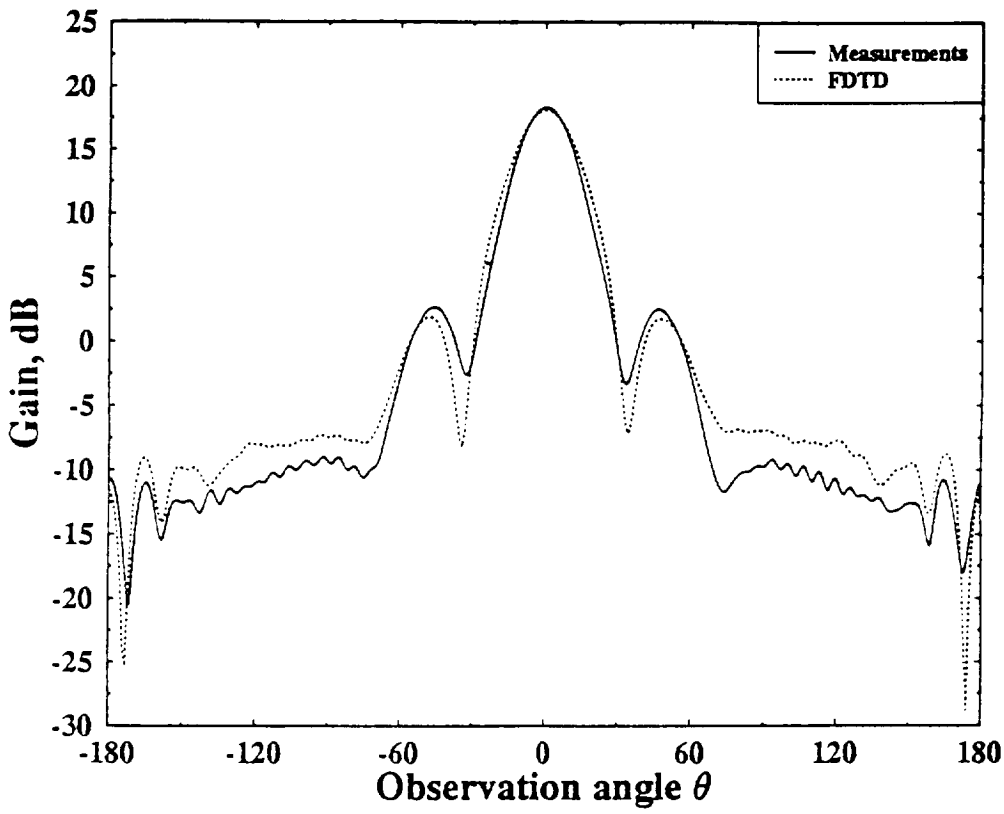

Figure 32: E-plane gain of a 20-dB standard gain pyramidal horn at 10.0 GHz, partially coated with GDS magnetic material ($\epsilon_r = 14.9 - j0.25$ and $\mu_r = 1.55 - j1.45$, t = 33 mil and $l_m = 2''$).

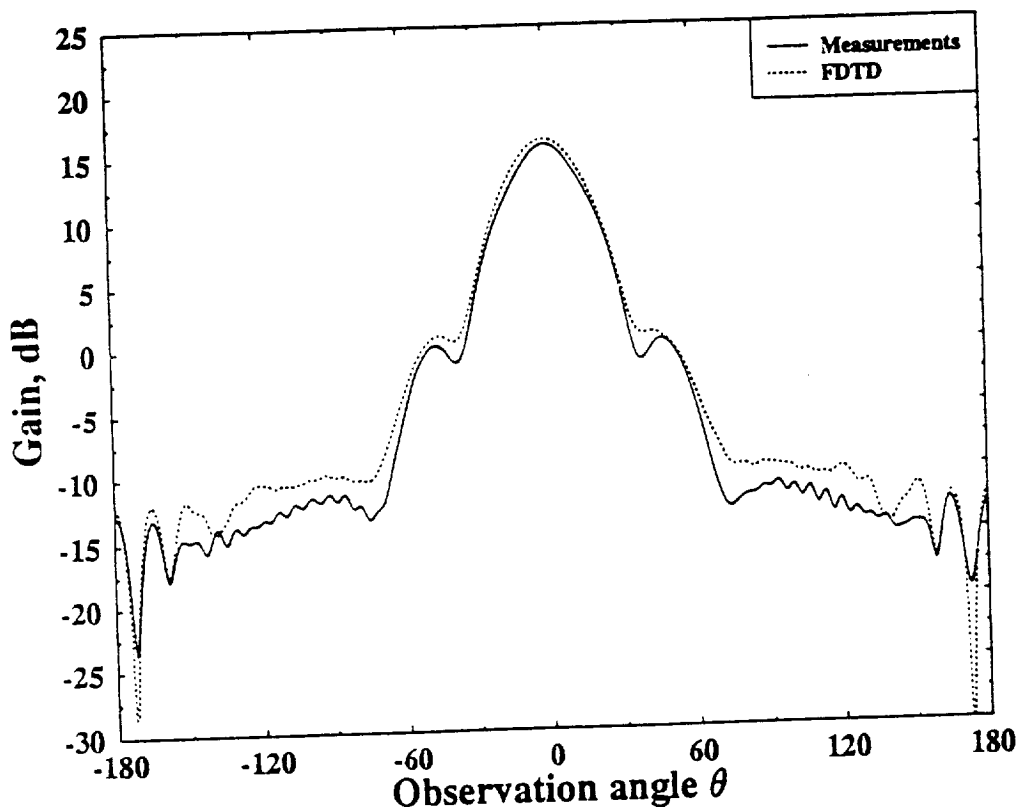

Figure 33: E-plane gain of a 20-dB standard gain pyramidal horn at 10.0 GHz, partially coated with GDS magnetic material ($\epsilon_r = 14.9 - j0.25$ and $\mu_r = 1.55 - j1.45$, t = 33 mil and $l_m = 4''$).

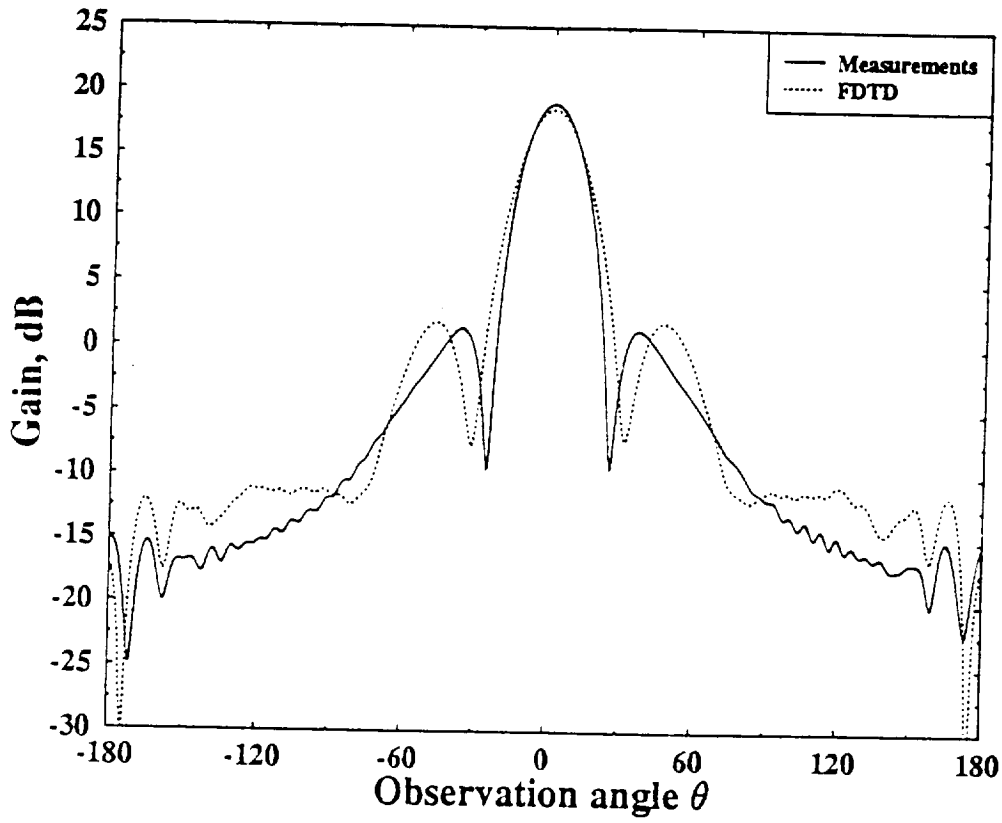

Figure 34: E-plane gain of a 20-dB standard gain pyramidal horn at 10.0 GHz, partially coated with GDS magnetic material ($\epsilon_r = 14.9 - j0.25$ and $\mu_r = 1.55 - j1.45$, t = 66 mil and $l_m = 2''$).

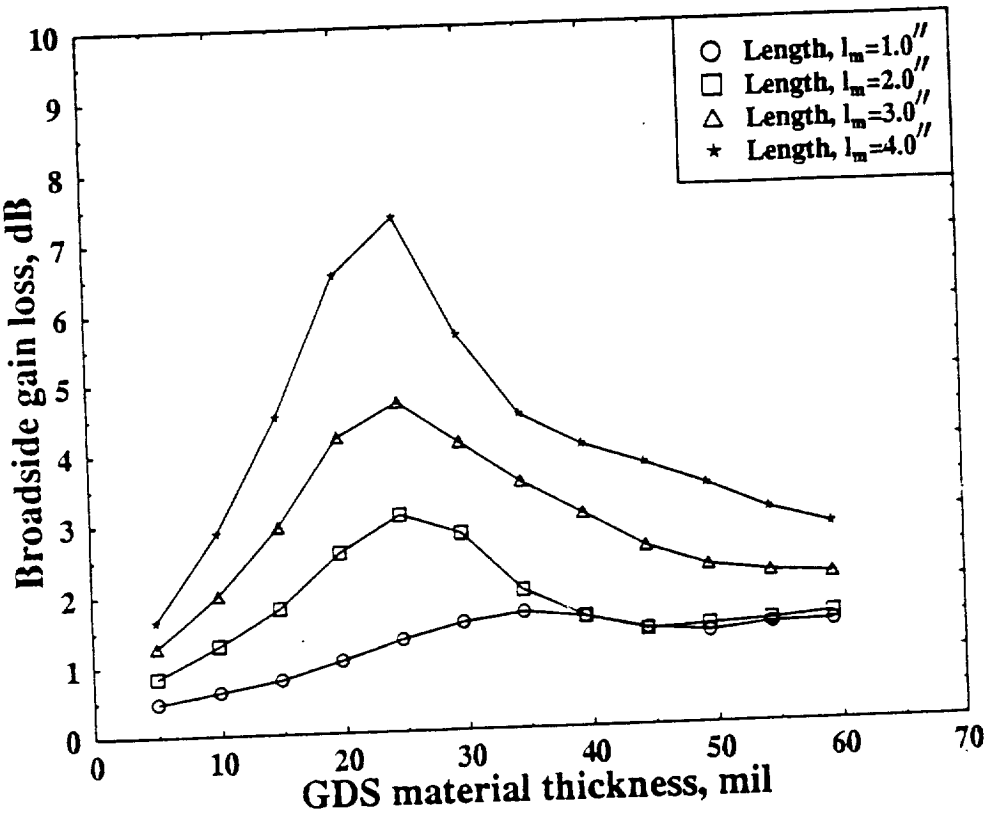

Figure 35: Broadside antenna gain loss of a 20-dB standard gain pyramidal horn at 10.0 GHz, partially coated with GDS magnetic material ($\epsilon_r = 14.9 - j0.25$ and $\mu_r = 1.55 - j1.45$).

III. ANTENNA TECHNOLOGY

A. Introduction

During this annual period, significant progress in the area of conformal cavity-backed and ferrite cavity-backed antennas has been achieved.

In the previous reports, the scattering and radiation performance of single elements of circular patches backed by circular and rectangular cavities were presented. Since then, we have succeeded in verifying some of the theoretical results by fabricating and testing a single circular patch antenna backed by a circular cavity. In addition, we have also developed numerical code for the analysis of the radiation characteristics of infinite arrays of probe-fed circular patches each backed by a circular or rectangular cavity.

In this report, the progress on the theory with the three dimensional analytic model of the CBS antenna is also reported. In addition, more cavity experiments have been performed to identify the types of magnetostatic wave modes excited. Now, the analytic model has the capability to calculate the monostatic or bistatic RCS (radar cross section) of the CBS antenna loaded with ferrite and dielectric layers and some theoretical results will be presented. The experiments have been concentrated on altering the cavity and feed structure in the hopes that this change would excite a magnetostatic volume wave mode, which resonates at UHF or even VHF. It will be shown that both magnetostatic volume and surface wave modes were excited strongly with this new configuration.

B. Cavity-Backed Microstrip Patch Antennas

One way to overcome the tradeoff that exists between bandwidth and scan volume in a microstrip patch element phased array is to surround each patch element with a cavity. By doing so, the substrate can no longer support guided wave modes. Therefore, the substrate thickness can be increased substantially to improve the bandwidth without a corresponding decrease in scan coverage.

In this report period, we have succeeded in verifying some of the theoretical results by fabricating and testing a single circular patch antenna backed by a circular cavity. Fig. 36 shows the cross section of this antenna. The parameters used for the experimental model are given by:

R_1 = 4.55 cm	R_2 = 5.72cm	
ϵ_r = 2.2 (1 - j0.0009)	μ_r = 1	
a = 4.55 cm	c = 0.2286 cm	
x_p = 1.18 cm	y_p = 0	r_0 = 0.045 cm

The antenna was tested by measuring the S11 parameter, using an HP8510 network analyzer. Fig. 37 illustrates the experimental and theoretical input impedance results on a Smith chart. As can be seen, the results agree well. Fig. 38 shows the theoretical and experimental return loss. The slight variation in the resonant frequency between the theory and experiment is primarily due to the tolerance of the dielectric constant of the substrate, and the machining of the cavity.

In this report period, we have also developed numerical code for the analysis of the radiation characteristics of infinite arrays of probe-fed circular patches each backed by a circular or rectangular cavity. The geometry of an infinite array of circular patches backed by circular cavities is shown in Fig. 39.

Results of the computer codes for the two different antenna geometries are compared to those of an infinite array of conventional patches. The parameters of interest are the broadside-matched active reflection coefficient, and the active resistance of an array elements. The broadside-matched reflection coefficient is determined by matching the antenna elements at broadside ($\theta = 0$, $\phi = 0$), and calculating the antenna reflection coefficient as a function of scan angle (Fig. 40). This can be used to determine the scanning range of the array as a function of substrate thickness. Furthermore, by calculating the active resistance of the antenna as a function of frequency for varying substrate thickness, we can gain insight into the bandwidth performance of the antenna.

We can begin by first considering a thin substrate. The parameters for Case A for the circular cavity-backed array are given by:

$R_1 = 0.178\ \lambda_0$	$R_2 = 0.222\ \lambda_0$	
$\epsilon_r = 2.5$	$\mu_r = 1$	
a $= 0.27065\ \lambda_0$	c $= 0.02\ \lambda_0$	
$x_p = 0.089\ \lambda_0$	$y_p = 0$	$r_0 = 0.004\ \lambda_0$
$d_x = 0.5\ \lambda_0$	$d_y = 0.5\ \lambda_0$	

Fig. 41 illustrates the E-plane (ϕ=0) broadside-matched active reflection coefficient of this antenna along with an equivalent array of circular patches backed by rectangular cavities and an array of conventional circular patches. The figure shows that for thin substrates the scan performance of conventional and cavity-backed patches are similar. However, there exists a peak in the reflection coefficient of the conventional array near grazing angle that does not appear in the cavity-backed patches. This peak corresponds to the excitation of leaky wave modes in the substrate of a conventional array that has been effectively eliminated in the cavity-backed patch geometries.

Fig. 42 illustrates the H-plane (ϕ=90) broadside-matched active reflection coefficient of the three antennas for Case A. This result is also similar for the three arrays.

Next, we increase the substrate thickness and look at the results for the three arrays. The parameters chosen for Case B are given by:

$R_1 = 0.164\ \lambda_0$	$R_2 = 0.205\ \lambda_0$	
$\epsilon_r = 2.5$	$\mu_r = 1$	
a $= 0.27065\ \lambda_0$	c $= 0.05\ \lambda_0$	
$x_p = 0.082\ \lambda_0$	$y_p = 0$	$r_0 = 0.004\ \lambda_0$
$d_x = 0.5\ \lambda_0$	$d_y = 0.5\ \lambda_0$	

Fig. 43 illustrates the E-plane reflection coefficient for Case B. The results indicate that the cavity-backed patch arrays show improvement in scan performance over the conventional patch array for the thicker substrate. Fig. 44 illustrates the H-plane reflection coefficient for Case B. The cavity-backed patch arrays also show enhanced performance in the H-plane, but not as dramatic as the E-plane. Furthermore, the leaky wave resonance in the conventional patch array has shifted closer to broadside that is an undesirable

effect of a thicker substrate. Finally, increasing the substrate thickness even more, we use parameters of Case C given by:

$R_1 = 0.156\ \lambda_0$	$R_2 = 0.195\ \lambda_0$	
$\epsilon_r = 2.5$	$\mu_r = 1$	
$a = 0.27065\ \lambda_0$	$c = 0.08\ \lambda_0$	
$x_p = 0.078\ \lambda_0$	$y_p = 0$	$r_0 = 0.004\ \lambda_0$
$d_x = 0.5\ \lambda_0$	$d_y = 0.5\ \lambda_0$	

Fig. 45 illustrates the E-plane reflection coefficient of the three arrays for Case C. The results show that the cavity-backed patch arrays demonstrate substantial improvement in their scan performance over the conventional patch array. Fig. 46 illustrates the H-plane reflection coefficient results. This also indicates that the cavity-backed patch arrays have an enhanced scan volume. Fig. 47 illustrates the E-plane reflection coefficient of the circular cavity-backed patch array as a function of substrate thickness. This clearly demonstrates the advantage of using a thicker substrate in obtaining better scan performance. In addition to scan volume enhancement, the cavity-backed patches also exhibit improvement in bandwidth. Fig. 48 illustrates the active resistance of the circular cavity-backed patch array as a function of substrate thickness. As can be seen, as the substrate thickness is increased the bandwidth of the array also increases.

The overall results of the cavity-backed patch arrays indicate that by increasing the substrate thickness, both scan volume and bandwidth performance of the array can be improved. Furthermore, surface and leaky wave resonances excited in the substrate of conventional microstrip patch phased arrays are completely eliminated in the cavity-backed patch arrays. Thus, the cavity-backed patch arrays show substantial improvement over the conventional patch arrays.

1. Future work for conformal antenna technology

During the next year, research in the area of conformal antenna technology will emphasize two major areas. These areas are (1) development of conformal antennas suitable for use at UHF and possibly lower frequencies, and (2)

incorporation of the effect of platform geometry and materials on conformal antenna radiation characteristics.

A. Conformal Antennas for UHF and Lower Frequencies

Microstrip antennas are extremely attractive candidates for aerospace applications because of their conformability, light weight and low cost. However, these antennas are rarely used at UHF and lower frequencies because of excessive size. Although the size of the antenna can be reduced by using a high dielectric constant substrate, the effects of surface waves supported by such substrates severely degrades the antenna performance. Past research on conformal antennas in this program has emphasized the development of cavity-backed microstrip antennas. This configuration is of great interest because the deleterious effects of surface waves are eliminated by the presence of the cavity. We propose to investigate the use of cavity-backed patch antennas such as that shown in Figure 49 at UHF and possibly lower frequencies.

B. Effect of Platform Geometry and Materials on Conformal Antenna Radiation Characteristics

Past research on conformal antennas in this program has emphasized the development of novel microstrip antenna concepts which overcome certain intrinsic disadvantages of microstrip antennas such as narrow bandwidth and the tradeoff between scan volume and bandwidth in large arrays without significantly comprising the attractive features that make microstrip antennas so desirable. It is now appropriate to begin to investigate the effect of platform geometry and materials on the antenna radiation characteristics. To this end the following tasks will be undertaken:

a. Extension of the hybrid FEM/spectral-domain MoM technique to three dimensions and to coated conductors.

b. Investigation of hybrid MoM/PO techniques for antenna radiation on complex platforms.

C. Ferrite Tuned Cavity Backed Slot Radiators

The cavity backed slot (CBS) antenna is a lightweight, conformal radiator, and considered efficient due to its electrical size and material loading within the cavity. Having these characteristics, the CBS antenna is an ideal choice for experimentation as a tunable antenna. As stated in previous reports, the concept of using a ferrite to magnetically tune a CBS antenna is not new [5]. The literature, however, lacks any substantial work to verify the capability of such an antenna [5], [6] and [7].

In the last report, the progress and some theory with the three dimensional analytic model of the CBS antenna was reported. Also, more cavity experiments were performed to identify the types of magnetostatic wave modes excited; however, only surface wave modes were excited. For completeness of this section, the properties of ferrites will be reviewed. After that, some of the verifications used to check the validity (correctness and accuracy) of the solution will be discussed. Then, some theoretical results of the RCS of the CBS antenna will be shown. The power handling capabilities of the ferrite layer will also be analyzed. The last portion of the section will summarize the analytical portion of this section.

1. Background

Ferrite substrates are ferromagnetic, or superparamagnetic, materials constructed from solid ceramic materials which have been sintered with certain metal oxides at high temperatures. At microwave frequencies they exhibit strong magnetic effects, which result in anisotropic behavior. By applying an external DC magnetic field, the permeability tensor of the ferrite is altered. This change occurs due to the interaction of the internal magnetic moment of the ferrite and the magnetic field of the material. The interaction effectively alters the electrical characteristics of the material used in the CBS structure. Consequently, the antenna will resonate at a different frequency for different values of the applied DC magnetic field.

There are two types of modes that can be excited inside the cavity. The first type of modes considered is the dynamic mode, which strongly depends on the the size of the cavity and the electrical properties of the materials inside the cavity. This mode is somewhat independent of the magnetic bias of the ferrite as shown in previous reports. This has been the traditional mode

type excited within the CBS antenna. The second type of modes considered is the magnetostatic mode. This mode also depends on the external magnetic bias field. For this type of modes, the biased ferrite material gives rise to low frequency magnetostatic volume wave modes which become appreciable with large external bias fields. The volume wave modes travel in the direction of the bias field. Furthermore, magnetostatic surface wave modes can exist. Their cutoff frequency is higher than a volume wave mode and these modes travel perpendicular to the direction of the bias field. It is these volume wave modes that will allow the a microwave CBS antenna to operate in a frequency range much lower than those of the dynamic modes.

2. Theoretical Analysis and Validation

The purpose of this section is to document the work on the rigorous modeling of the CBS antenna filled with dielectric and ferrite layers. The CBS antenna is depicted in Figure 50. Previously, the methodology taken to solve this problem and the progress of the code was discussed. Since the last report, the echo area of a rectangular CBS filled with any combination of ferrite and dielectric layers can be analyzed.

Numerical solutions of real world problems are often treated as boundary value problems. These mathematical descriptions cannot always be performed in 'closed form.' The mathematical methods of solution can be very complex and may require intense numerical computation. When reducing the mathematical formulas to tractable numerical algorithms, some numerical approximations may be employed, e.g. utilizing gaussian quadrature to perform a numerical integration. Therefore, it is necessary to examine and verify the software's results to gain confidence in the correctness and accuracy of the solutions. Of course, checks can only be performed in some limiting sense, since for a flexible code, the necessity of checking all possible cases would be a major undertaking. Also note that no set of comparisons can be considered as absolute proof that the code works under all possible conditions.

Rather than show all the checks performed on the software, only two checks will be shown. The first will be a comparison of two different codes which can analyze a CBS antenna. The comparison code was written by Dr. Aberle, a contributor of this program, for another project [8]. The second comparison will be between an analytic expression and the moment

method/spectral domain approach (SDA) for the interior admittance.

The first geometry used for validation is an annular slot cut in a perfectly conducting plane. The interior region is a rectangular cavity filled with a single homogeneous layers of dielectric material. The structure is depicted in Figure 51. The dimensions can be seen in Table 2. Both solutions are obtained using Galerkin's method and SDA [9]-[11]; however, the Green's functions are determined differently. The modes chosen to expand the fields in the slot are of the same form but chosen in a different manner. The two codes were written independently of one another.

Variable	Meaning .	Physical Dimensions
R_1	inner radius of slot	2.0 cm
R_2	outer radius of slot	2.1 cm
a	cavity width	4.2 cm
b	cavity length	4.2 cm
c	cavity depth	0.21844 cm
μ_r	relative permeability	2.33
ϵ_r	relative permittivity	1.0

Table 2: Annular CBS Parameters.

The results for the monostatic RCS at a frequency of 5 GHz are shown in Figure 52. As shown the $\phi\phi$ polarization of the RCS overlay exactly. The $\theta\theta$ polarization of the RCS overlays at normal incident, and diverges slightly, on the order of 1 dB as the echo area is measured at grazing incidence. This slight variation is a function of the basis set chosen and in the evaluation of the exterior admittance elements. Dr. Aberle's code chooses the azimuthal modal expansion number, the ϕ variation, to lie between 0 and 2. The code developed in this program chooses the azimuthal mode number to lie between 0 and 3. Also, Dr. Aberle's code does one numerical integration and one analytic integration in the exterior admittance calculation since the slot and exterior region is ϕ symmetric. The code developed here does two numerical integrations since the slot shape of interest is the rectangular slot which has no ϕ symmetry. These differences attribute slightly to discrepancies between the two calculated results. It is unclear to say which result is a more accurate prediction; however, both results are correct.

The second result is a comparison of the internal matrix elements for a dielectric loaded rectangular cavity. If the rectangular slot is the same dimension as that of the cavity, the interior matrix can be solved for analytically. This closed form solution is analogous to a multimode transmission line terminated in a short circuit. This is described in the context of the network formulation explained in the previous quarterly report. Table 3 depicts the interior structure to be analyzed and Table 4 lists the matrix elements as calculated by the SDA and the transmission line method. The agreement is excellent. Note that the real part of all elements are zero. This occurs since the materials were assumed lossless. If the materials were lossy, the real part would have a positive value.

Variable	Meaning	Cavity Dimensions
a	cavity width	1.7 cm
b	cavity length	2.0 cm
c	cavity depth	0.1 cm
μ_r	relative permeability	1.0
ϵ_r	relative permittivity	1.0

Table 3: Rectangular Cavity Parameters.

mode number	SDA	Analytic
1	-1.0631×10^{-1}	-1.0631×10^{-1}
2	-1.0665×10^{-1}	-1.0665×10^{-1}
3	-1.0751×10^{-1}	-1.0751×10^{-1}
4	1.1686×10^{-3}	1.1686×10^{-3}
5	-1.0890×10^{-1}	-1.0890×10^{-1}

Table 4: Imaginary part of the Interior Admittance Calculation.

3. Numerical Results

A single result for the monostatic RCS at normal incidence from a CBS antenna versus frequency for different values of H_o will be discussed. The antenna's dimensions can be found in Table 5 and the results can be seen in Figure 53. The structure is very similar to the cavity examined in the measurement portion of this section of the report. The frequency was varied between 400 MHz and 2 GHz. Two differently-directed DC bias fields are shown, H_o is 200 and 400 Oersted (Oe). The third plot corresponds to replacing the ferrite material by a dielectric layer, $4\pi M_s = 0$. As shown in the figure, the $\theta\theta$ polarization of the RCS is much more weakly excited as compared to the $\phi\phi$ polarization. In addition, the $\theta\theta$ polarization has little to no variation for different bias strengths. The $\theta\theta$ polarization is the cross polarization of the slot which does not couple strongly to the cavity or radiate well. The copolarized field, in this case the $\phi\phi$ polarization, is more influenced by the magnetization. The ripples in the RCS calculation correspond to the excitation of magnetostatic modes in the ferrite material. The first dynamic mode resonance is above 3 GHz. By examining the curve corresponding to a DC bias of 200 Oe and some fundamental equations for a ferrite, some insight can be gained into the nature of the magnetostatic resonances.

The equations governing the cutoff and resonance of magnetostatic backward volume wave and magnetostatic surface wave modes are given by,

$$f_c = \gamma\sqrt{H_o(H_o + 4\pi M_s)} \tag{11}$$

$$f_{r_{vwm}} = \gamma H_o \tag{12}$$

and,

$$f_c = \gamma\sqrt{H_o(H_o + 4\pi M_s)} \tag{13}$$

$$f_{r_{swm}}^{fs} = \gamma(H_o + 2\pi M_s) \tag{14}$$

$$f_{r_{swm}}^{mw} = \gamma(H_o + 4\pi M_s) \tag{15}$$

where γ is the gyromagnetic ratio and the subscripts vwm and swm refer to volume and surface wave modes, respectively. Also, the superscripts refer to the free space boundaries (fs) and metallic wall boundaries(mw). Note that the cutoff frequencies of the two cases are identical and the volume

wave mode cutoff frequency is greater than its resonance frequency, $f_{r_{vwm}}$. For the case under discussion, f_c is 1.25 GHz and $f_{r_{vwm}}$ is 560 MHz. We can see the first deviation from a smooth curve occurs at approximately $f_{r_{vwm}}$ and the magnetostatic volume mode resonances in the RCS of the CBS antenna occur at approximately 750 MHz and 1.05 GHz. This resonance at 750 MHz is in the UHF range desired. Proper design of the CBS antenna may even lower this resonance into the VHF range. The next resonance is seen at approximately 1.65 GHz and is in the surface wave mode range. The resonance frequency for a surface wave mode for free space boundaries occurs at 1.68 GHz. Since the ferrite layer is suspended between the top and bottom walls of the structure, it is neither bounded by metallic walls or free space. However, due to the proximity of the walls to the ferrite layer, it is not unreasonable to assume that a strong resonance may occur at $f^{mw}_{r_{swm}}$. In addition, there is another much weaker resonance at 1.75 GHz. This is another surface wave mode. This configuration is interesting since these resonances occur at frequencies very close to the resonances seen in the cavity experiments.

4. Power Handling Capabilities

The equations of motion utilized in describing magnetic material have non-linear terms. This nonlinearity can provide a mechanism for coupling the uniform precession of the electrons to spin wave modes at power levels much less than that required for r.f. saturation of the precession. This flood of energy out of the uniform motion of the electrons prevents the precession angle from increasing and brings about the early onset of the decline of the permeability at resonance [12]. Suhl [13] has determined an approximate form for estimating the threshold of this high power catastrophe. This can be written in the form,

$$h_{crit} = \frac{1}{2}\Delta H\sqrt{\frac{\Delta H}{4\pi M}} \tag{16}$$

Therefore, if the structure of the previous section is examined, $4\pi M$ and ΔH was 800 and 10 Oe, respectively. Solving for h_{crit} in the above equation yields 0.54 Oe which is equivalent to approximately 280 watts peak power ([12], page 586). Time averaged magnetic stored power can be found from [14]. Assuming that the field is constant in the material, the time averaged

power stored in a given block of material is,

$$P_m = \frac{1}{2}\omega\mu_o|H_{r.f.}|^2 V \tag{17}$$

Assuming one ferrite layer of Table 5 and an operating frequency of 800 MHz, the average power is approximately 46 watts.

Of course, the power dissipated due to losses in the material would heat the ferrite and change the material properties by passing the Neél temperature. The Neél temperature of a ferrite is a temperature above which the thermal energy is sufficient to destroy the magnetic alignment and thus the material becomes paramagnetic. Therefore, for high power applications, cooling the ferrite becomes a concern.

5. Summary

To date, the echo area of a rectangular CBS antenna filled with any combination of ferrite and dielectric layers can be analyzed. During the next year, work will continue on the formulation necessary for the analysis of the strip feed and the gain of the CBS antenna. Only the theory necessary for the normalization of the power pattern to calculate the directivity needs be considered. The programming of the feed portion of the CBS antenna will begin.

D. Cavity Backed Slot Experiments

Since the last report period, the experiments have been concentrated on altering the cavity and feed structure in the hopes that this change would excite a magnetostatic volume wave mode. Both magnetostatic volume and surface wave modes were excited strongly with this new configuration. The results of these measurements will be discussed in this section.

Previously, a cavity backed slot antenna was built employing low loss ferrite and dielectric layers and a two permanent magnet bias system. The slot was fed from a microstrip line centered in the slot which was centered in the cavity as shown in Figure 54. The scattering parameters were measured with an HP-8510 network analyzer and showed a magnetostatic wave resonance at 1.87 GHz. The power pattern of the CBS antenna was measured and agreed with S- parameter measurements by showing a peak in the gain at about

1.75 GHz. It is expected that at 1.87 GHz, the slot/microstrip configuration is tightly coupled and no radiation should occur. Slightly off that frequency is where the radiation happens since the feed match is still good, but the slot/microstrip coupling is now weaker. A second peak in the gain was seen at 800 MHz. This is a second lower frequency peak which is also a magnetostatic wave resonance. Unfortunately, it was only excited during the radiation measurements. This second peak is near the frequency range desired. This suggested that a different excitation was necessary to excite this mode. The experiments before were focused on varying the slot/microstrip feed to better understand the mechanism for resonance and to excite the lower frequency magnetostatic wave mode. The results showed that only a magnetic surface wave mode was excited. To excite magnetic volume wave mode, another feed structure was designed and built (Figure 55). The feed structure in this case was inside the cavity. This structure excited both surface and volume wave modes strongly.

Before discussing the experiments performed, the reasoning for the present feed configuration will be discussed. The desired low frequency volume wave mode has as its main component a vertical magnetic field. It is this field quantity that must be couple to the probe for a strong volume wave mode excitation. Previously, the feeds have been isolated from the ferrite through the slot. One possible way to couple to this magnetic field would be a vertical magnetic dipole, but it is a fictitious device. An electric loop can excite a vertical magnetic field. This loop must be located close the ferrite, in the cavity, to avoid any modal distortion seen by coupling through the slot. The other design parameter was to make this cavity a two-port device to determine the loss in the structure and the radiation efficiency. From these simple conditions, the cavity was altered and the new feed configuration was built.

Two sets of experiments will be discussed here. The first set will consider the new feed structure in the cavity with the slot short circuited (closed). The purpose of these first experiments were to force a volume wave magnetostatic mode to be excited. The second set of experiments were to determine how efficient the magnetostatic wave modes couple to the antenna. Note that all measurements were taken with an HP-8510 network analyzer over a frequency range of 50 MHz to 2 GHz. Also, the DC bias field is y-directed, in the plane of the homogeneous layers.

1. Closed Cavity Experiments

The first experiment shown in Figure 56 is the scattering parameters of the closed cavity configuration with a straight line feed across the cavity. The dimensions of the slot and cavity are shown in Table 5. The probe is centered in the third layer of the cavity. Similar to what was reported previously, a magnetostatic surface wave mode is excited, but at a lower frequency, 1.61 GHz. This mode is shifted in frequency due to the removal of the slot from the fixture. The second experiment shown in Figure 57 is same as the previous experiment but with the straight line replaced by a bent one. A different resonance mode was seen at approximately 1 GHz. This is a volume mode resonance. In this figure, the surface wave mode resonance can also be seen at 1.93 GHz. To insure that the second resonance seen is a volume wave mode, one of the permanent magnets was removed and replaced by a steel cube of the same dimensions. If the mode is a volume wave mode, the resonance should decrease in frequency and become higher Q due to the decrease of the DC magnetic bias field. If the mode is a surface wave mode, the decrease in the magnetic field should make the mode disappear, since the surface wave mode is much more sensitive to changes in the DC magnetic bias field. Figure 58 shows this change in the bias field. As seen by examining S_{11}, the dip decreased to 815 MHz and became more narrow and deep. This confirmed that the mode excited at 1 GHz and shifted to 815 MHz while decreasing the bias field is a magnetostatic volume wave mode. This resonance is in the UHF range and suggests a resonance in the VHF range is possible. Also, if the total power is calculated at these frequencies using $|S_{11}|^2 + |S_{21}|^2$, the losses are extremely small, on the order of 1% or less.

2. Slot/Cavity Experiments

The second set of measurements examined are the ferrite-loaded cavity with the slot open. Rather than show many results to determine loss, the S-parameters of the two port, radiation efficiency and the match with different loads on one port, only one plot will be shown and the results summarized. This plot, Figure 59, shows the efficiency, S_{11}, of the cavity backed slot with one probe shorted. Only one ferrite layer was in the cavity and it was biased by one permanent magnet. The probe was bent and suspended between the ferrite layer and the slot. At 1.29 GHz, the return loss is -2.45 dB; therefore,

56% of the power enters the cavity. From the first set of experiments, it was shown that the cavity is very low loss. This power must exit the cavity through the slot since it has nowhere else to go. Many different configurations were examined to be able to couple strongly to a volume wave mode in the cavity, and to the slot. This second set of experiments could again couple to the volume wave mode in the cavity, but could not couple strongly to the slot. The volume wave mode seems trapped within the ferrite layer. The slot needs to be changed in shape and/or position to couple more strongly to the cavity mode.

3. Conclusions and Future Work

The results presented in this report have been two-fold: (1) theoretical echo area and power handling capabilities of a three-dimensional CBS antenna partially filled with ferrite and dielectric layers and (2) experimental results showing the excitation of a magnetostatic surface and volume wave modes, their tuning by a variable DC magnetic bias in the CBS structure, and radiation efficiency. These results represent two significant steps in the design and modelling of ferrite filled CBS antennas. This is the first time that the theoretical calculation of the RCS from a ferrite and dielectric filled three dimensional CBS antenna has been reported to the authors' knowledge. It is important to discern this work from the contributions of many previous investigators utilizing ferrite material in the design of an antenna. Most investigators assume that the ferrite material is isotropic with a permeability that changes with the DC magnetic bias field, e.g. an effective permeability. This assumption ignores the effect of the off-diagonal terms of the permeability tensor to simplify the field equations. In this work, a *full wave* solution is utilized, hence, the permeability tensor is included in the analysis.

Secondly, the magnetostatic volume wave mode was excited experimentally and tuned by varying the DC magnetic bias of the ferrite. This is a significant step in the design of a broadband, electrically small CBS antenna. Both the theoretical and experimental resonances occurred in the desired UHF range. The potential for exciting a VHF resonance with a different design is feasible. Furthermore, the experimental results indicated that the antenna was poorly matched. The many degrees of freedom in the CBS antenna makes an empirical design over large bandwidths extremely time consuming. For an accurate CAD model of the antenna, the input imped-

ance of the probe in the cavity must be calculated. The input impedance calculation is one of future goals of this project.

During the next period (near term goals), additional experimental work on modifications of the cavity and feed network will be performed. The objective is to improve the input impedance and coupling from the volume wave mode to the slot. Also, some more novel ways to control the bias field rather than just removing a magnet will be considered.

In addition, the finishing touches will be put on the theory necessary to include the feed and the programming will begin. Once the feed is added to the analysis, input impedance and other useful information can be extracted.

The more long term goals of this project should be the inclusion of gain in the analysis of the CBS antenna. More information on tuning the slot, material losses, and radar cross section vs. magnetization and frequency would be available for the entire structure of interest. An infinite array analysis would be useful to determine the coupling effects in a large array environment. Also, the measurement of the RCS and gain of a CBS antenna would be useful for comparison with theory.

Layer	Variable	Meaning	Physical Dimensions
	a	cavity width	1.3 in
	b	cavity length	2.0 in
	c	cavity depth	0.8 in
	l	lot length	1.2 in
	w	slot width	0.3 in
	H_o	DC magnetic bias field	200 Oe
1	μ_r	relative permeability	1.0
	ϵ_r	relative permittivity	1.0
	t_1	thickness of the 1st layer	0.10 in
2	μ_r	relative permeability	1.0
	ϵ_r	relative permittivity	13.9
	$4\pi M_s$	saturation magnetization	800 Oe
	ΔH	resonance line width	10 Oe
	t_2	thickness of the 2nd layer	0.25 in
3	μ_r	relative permeability	1.0
	ϵ_r	relative permittivity	10.5
	t_3	thickness of the 3rd layer	0.02 in
4	μ_r	relative permeability	1.0
	ϵ_r	relative permittivity	1.0
	$4\pi M_s$	saturation magnetization	800 Oe
	ΔH	resonance line width	10 Oe
	t_4	thickness of the 4th layer	0.25 in
5	μ_r	relative permeability	1.0
	ϵ_r	relative permittivity	2.2
	t_5	thickness of the 5th layer	0.08 in

Table 5: Rectangular Slot and Cavity Parameters.

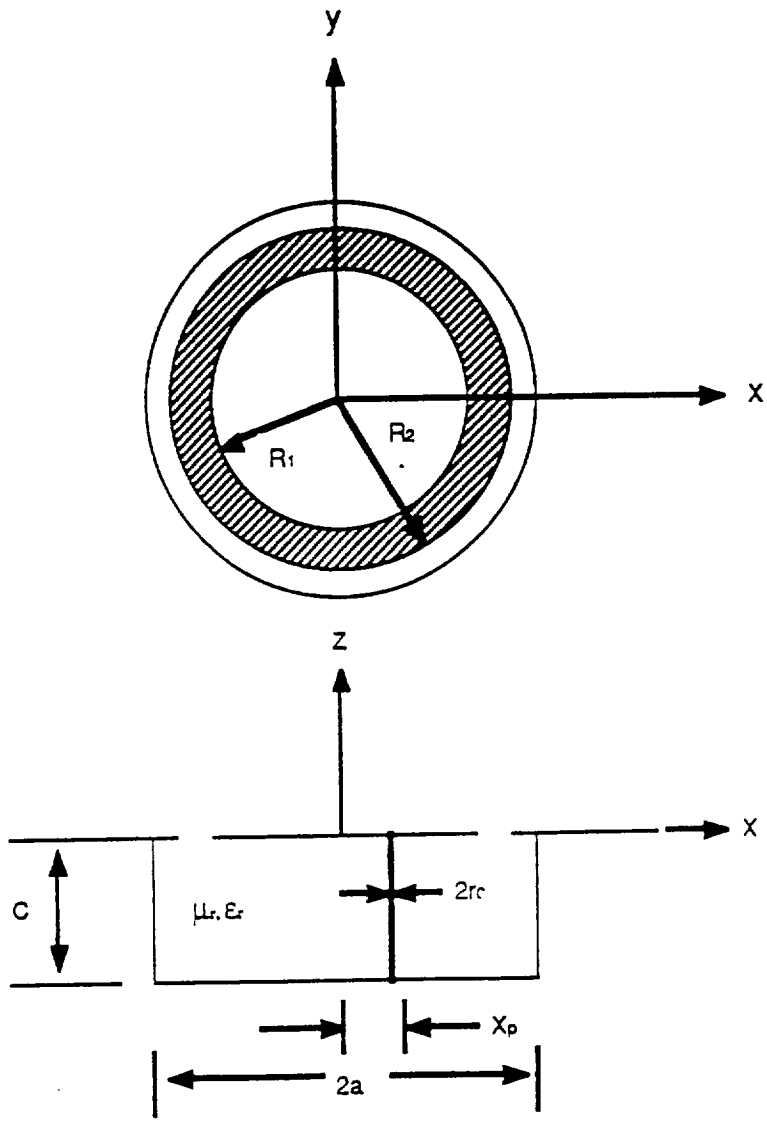

Figure 36: Geometry of a probe fed circular patch backed by a circular cavity.

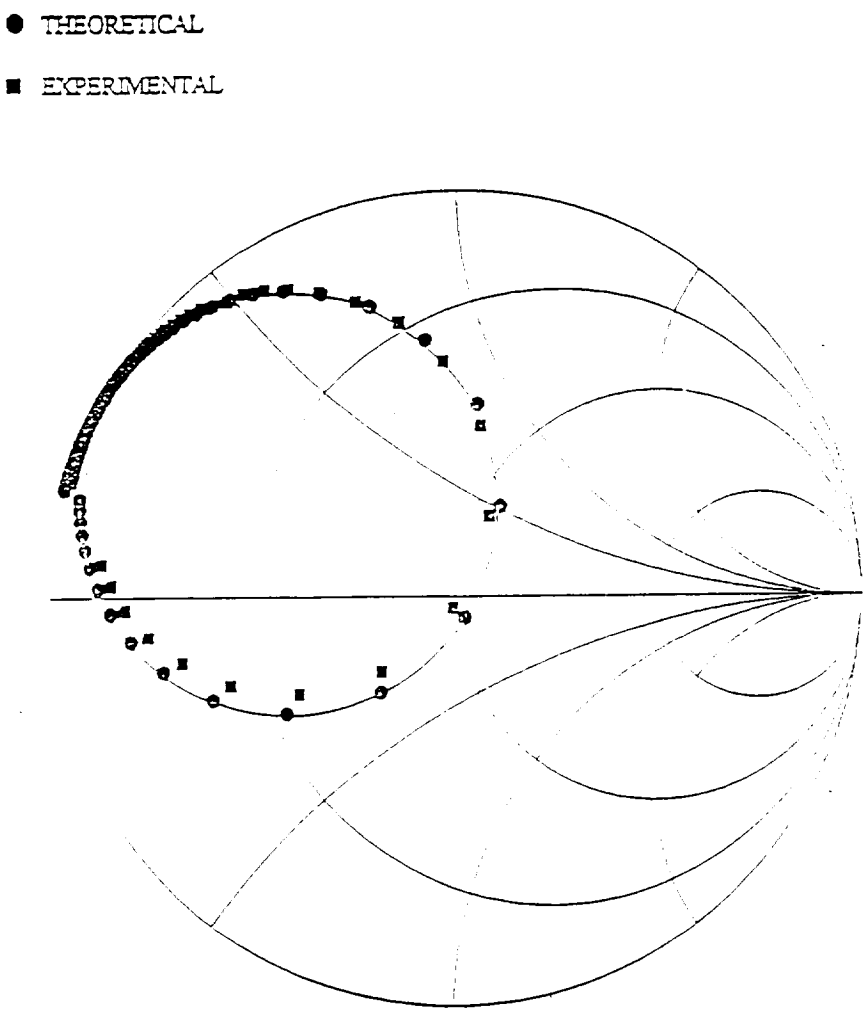

Figure 37: Input impedance versus frequency for circular cavity-backed circular patch on Smith chart (experimental and theoretical results) ($\epsilon_r = 2.2$).

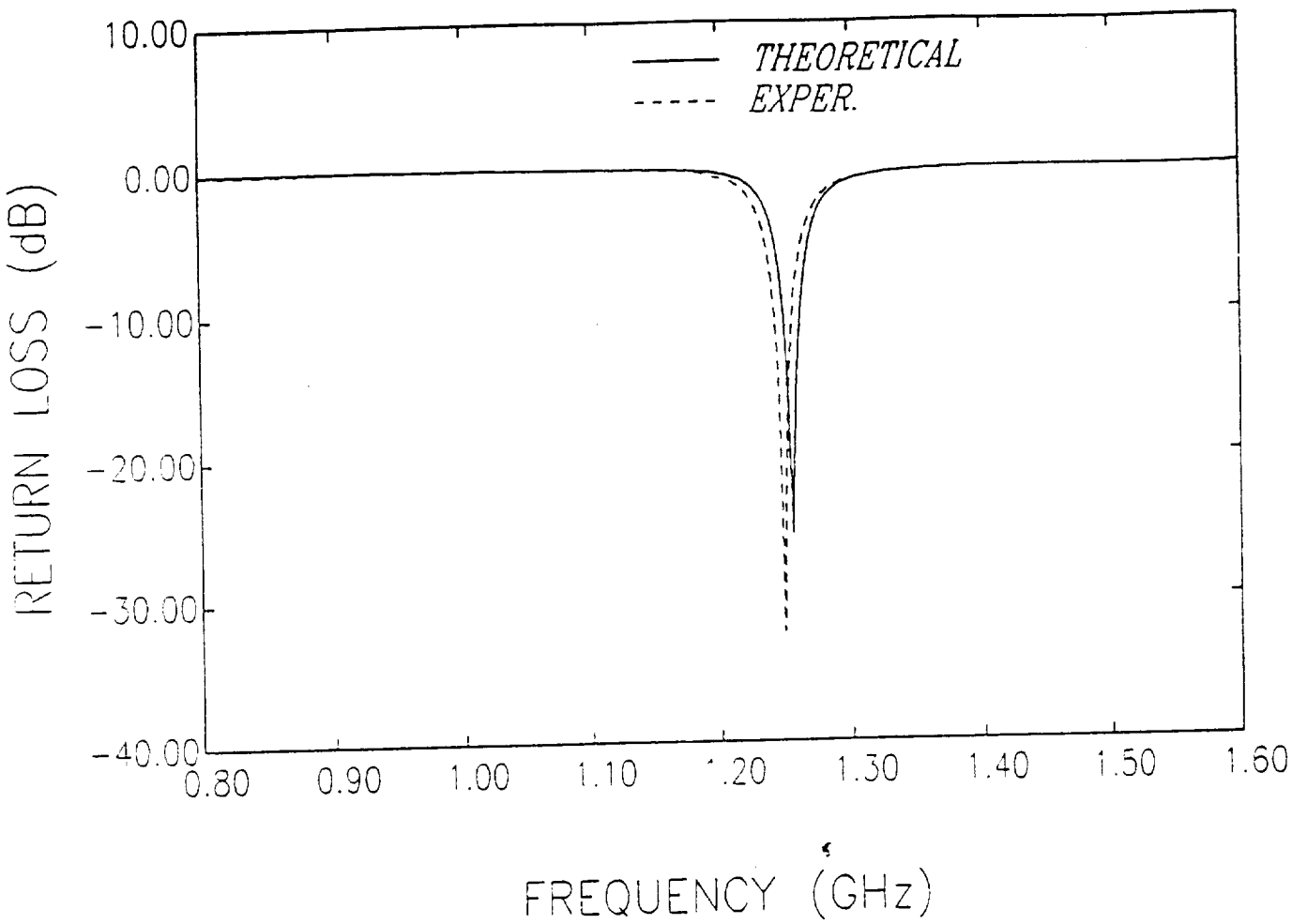

Figure 38: Return loss versus frequency for circular cavity-backed circular patch (experimental and theoretical results) ($\epsilon_r = 2.2$).

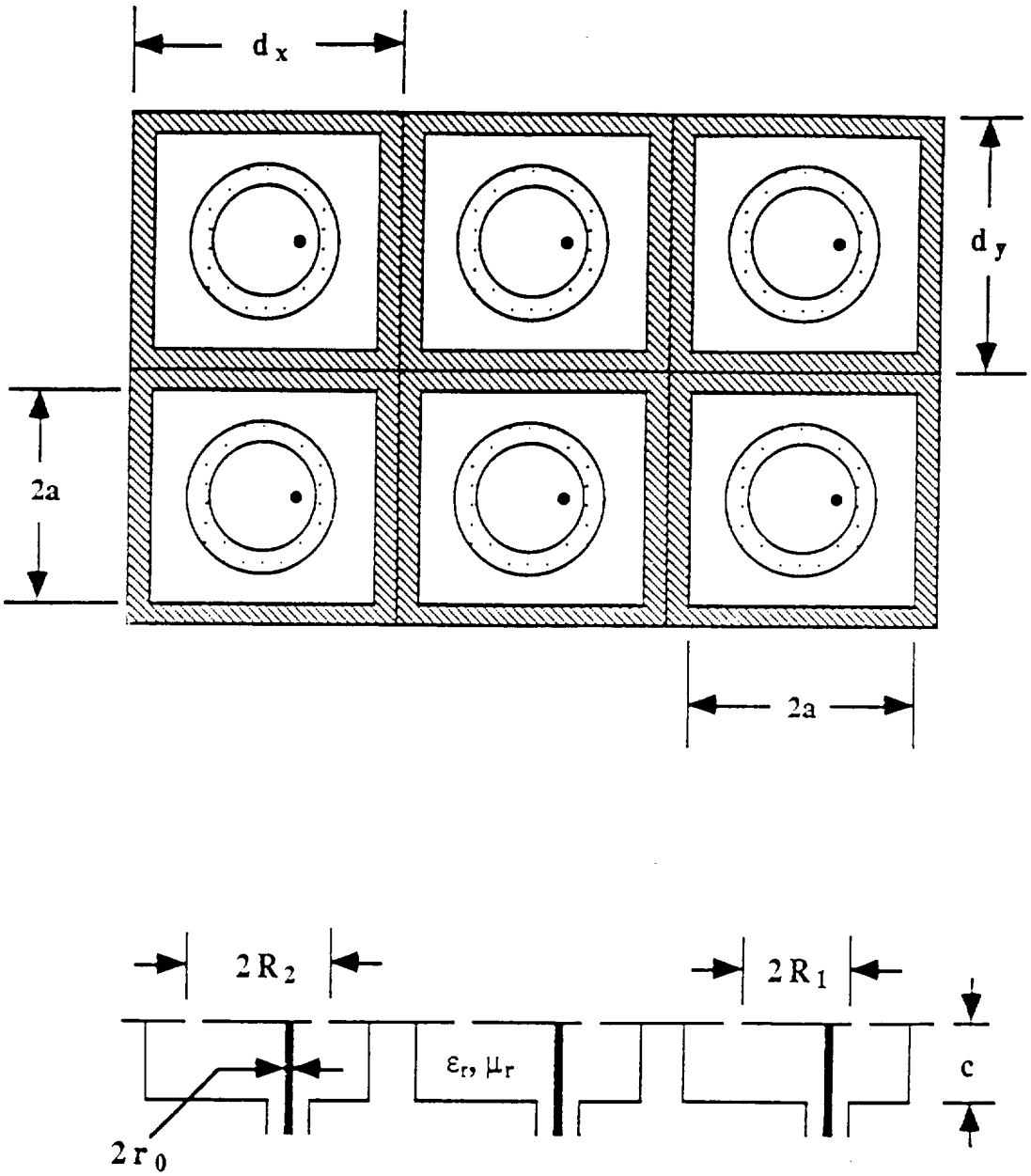

Figure 39: Schematic of an infinite array of probe fed circular microstrip patches each backed by a circular cavity.

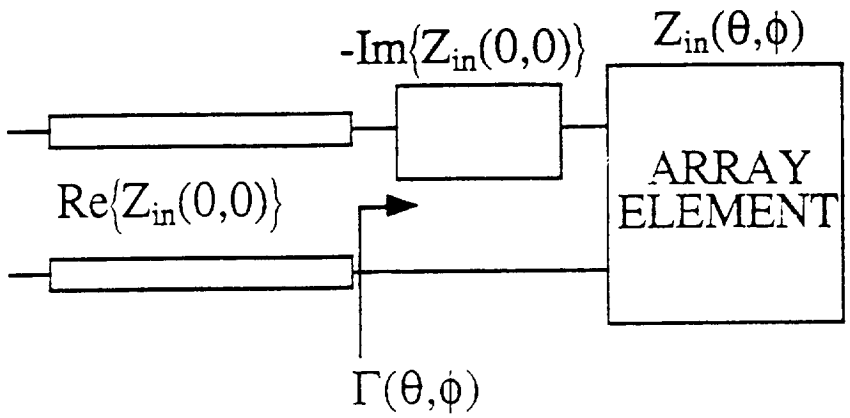

$$\Gamma(\theta,\phi) = \frac{Z_{in}(\theta,\phi) - Z_{in}(0,0)}{Z_{in}(\theta,\phi) + Z_{in}^{*}(0,0)}$$

Figure 40: Broadside-matched active element reflection coefficient of the cavity-backed patch antenna.

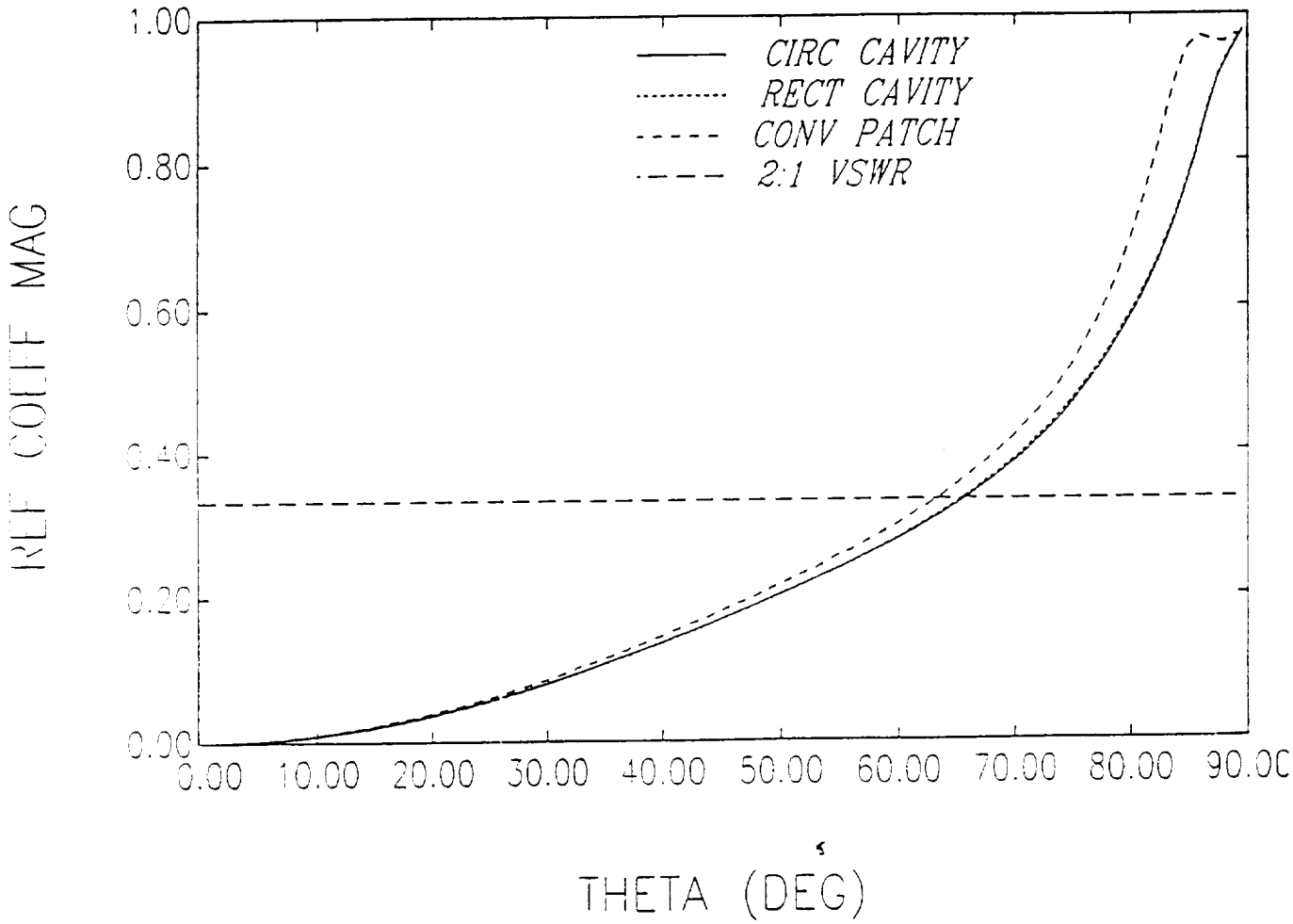

Figure 41: E-plane broadside-matched reflection coefficient versus scan angle for infinite arrays of circular and rectangular cavity-backed and conventional patches (d=0.02 λ_0).

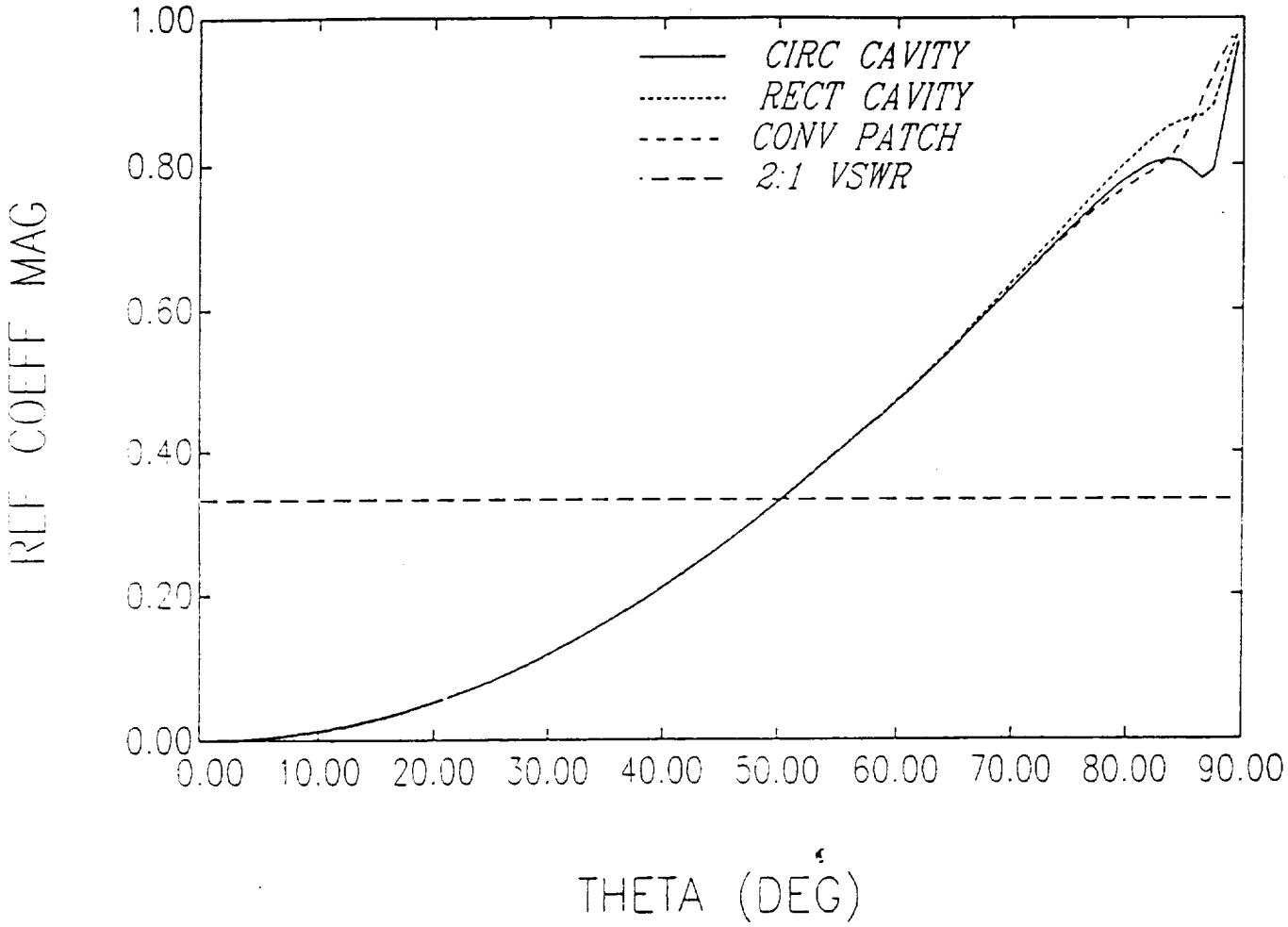

Figure 42: H-plane broadside-matched reflection coefficient versus scan angle for infinite arrays of circular and rectangular cavity-backed and conventional patches (d=0.02 λ_0).

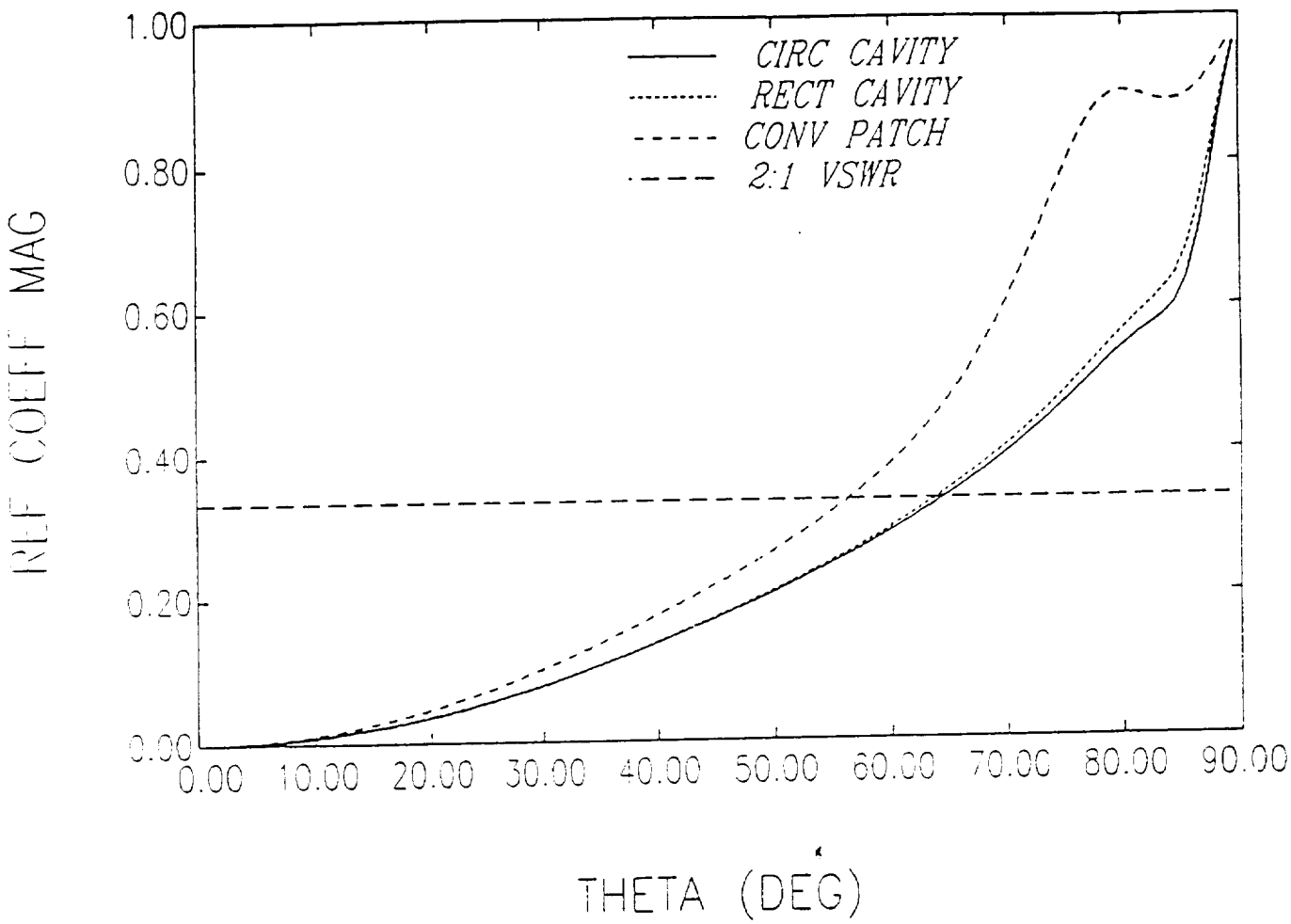

Figure 43: E-plane broadside-matched reflection coefficient versus scan angle for infinite arrays of circular and rectangular cavity-backed and conventional patches (d=0.05 λ_0).

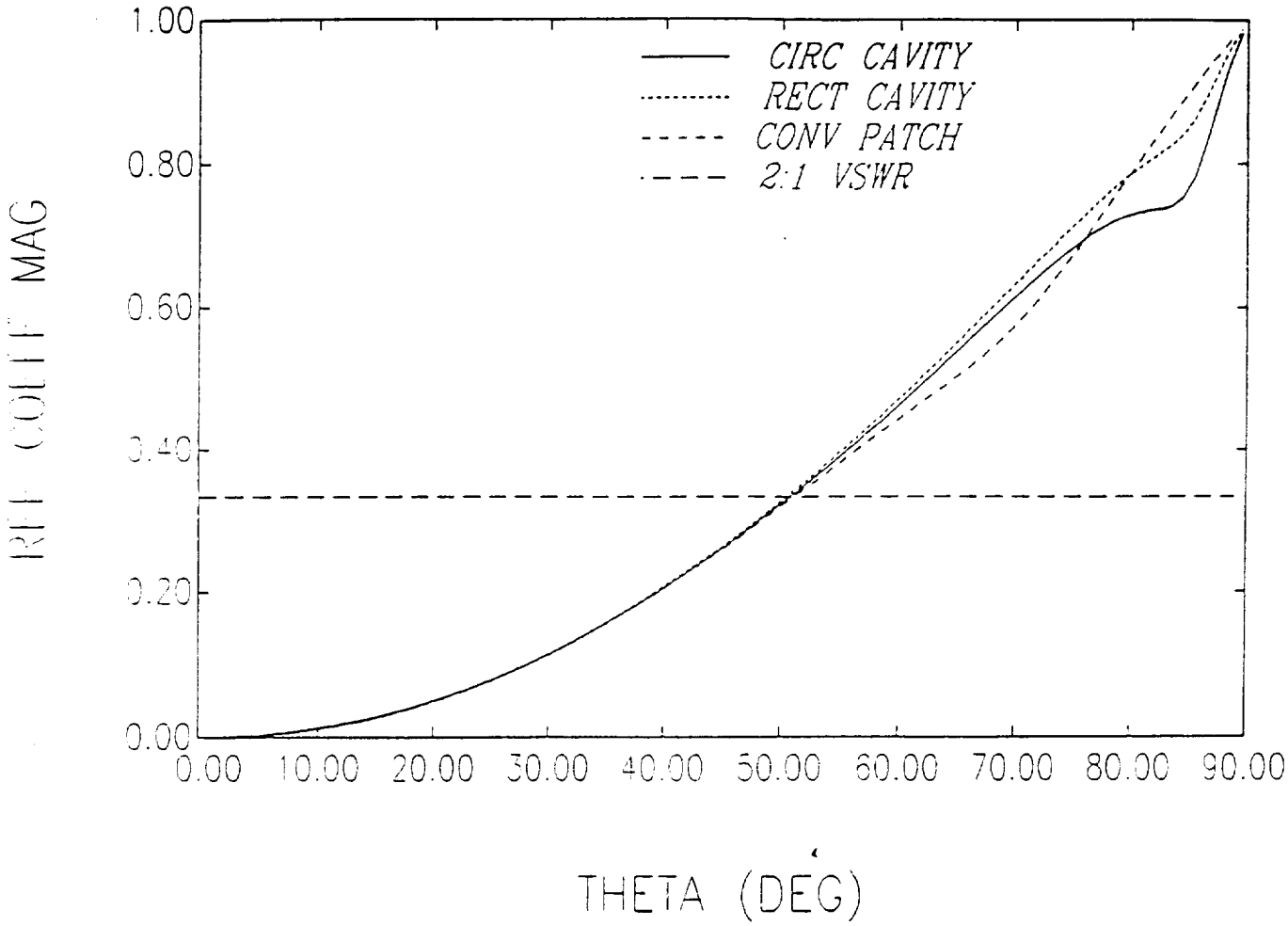

Figure 44: H-plane broadside-matched reflection coefficient versus scan angle for infinite arrays of circular and rectangular cavity-backed and conventional patches (d=0.05 λ_0).

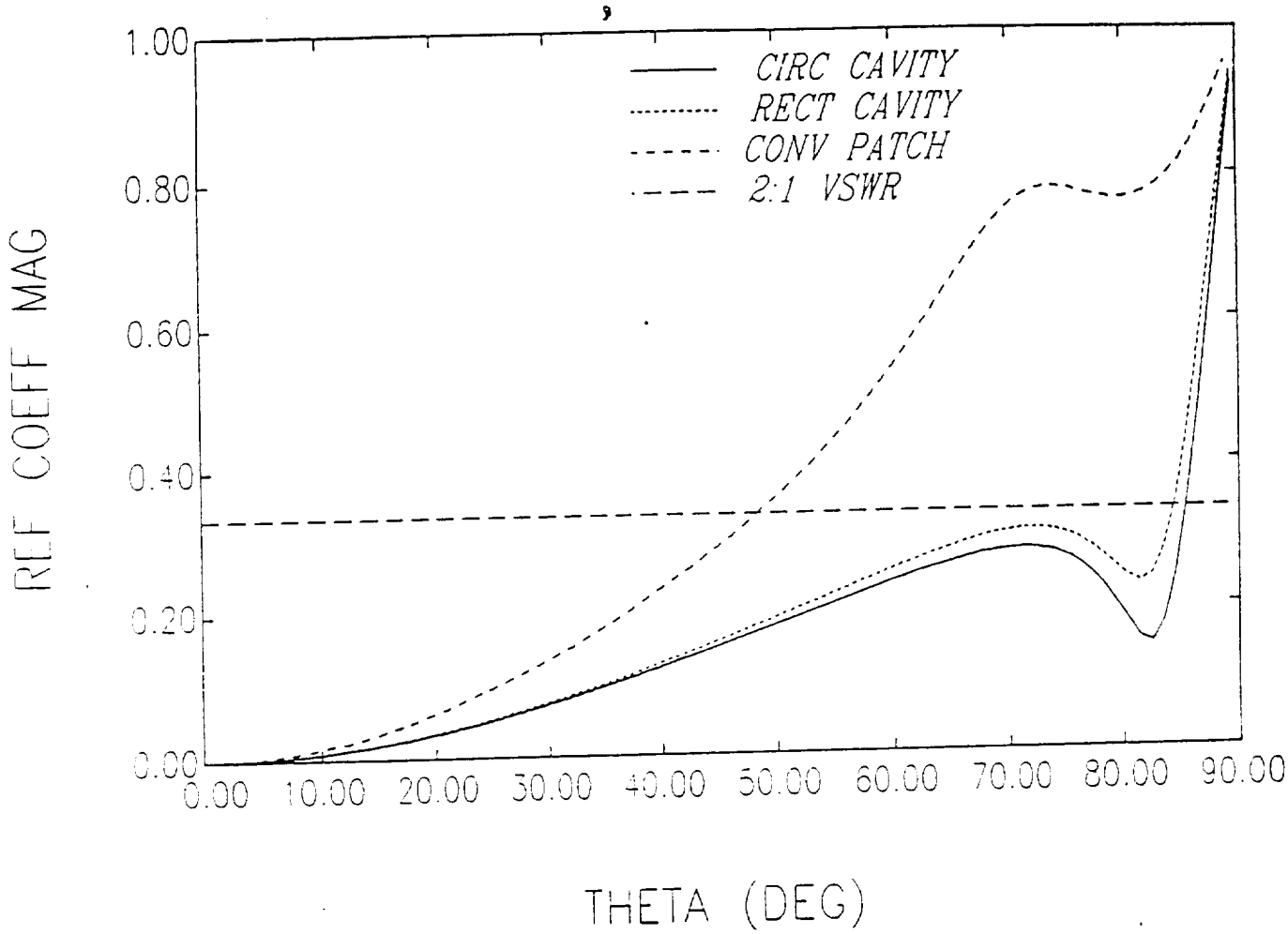

Figure 45: E-plane broadside-matched reflection coefficient versus scan angle for infinite arrays of circular and rectangular cavity-backed and conventional patches (d=0.08 λ_0).

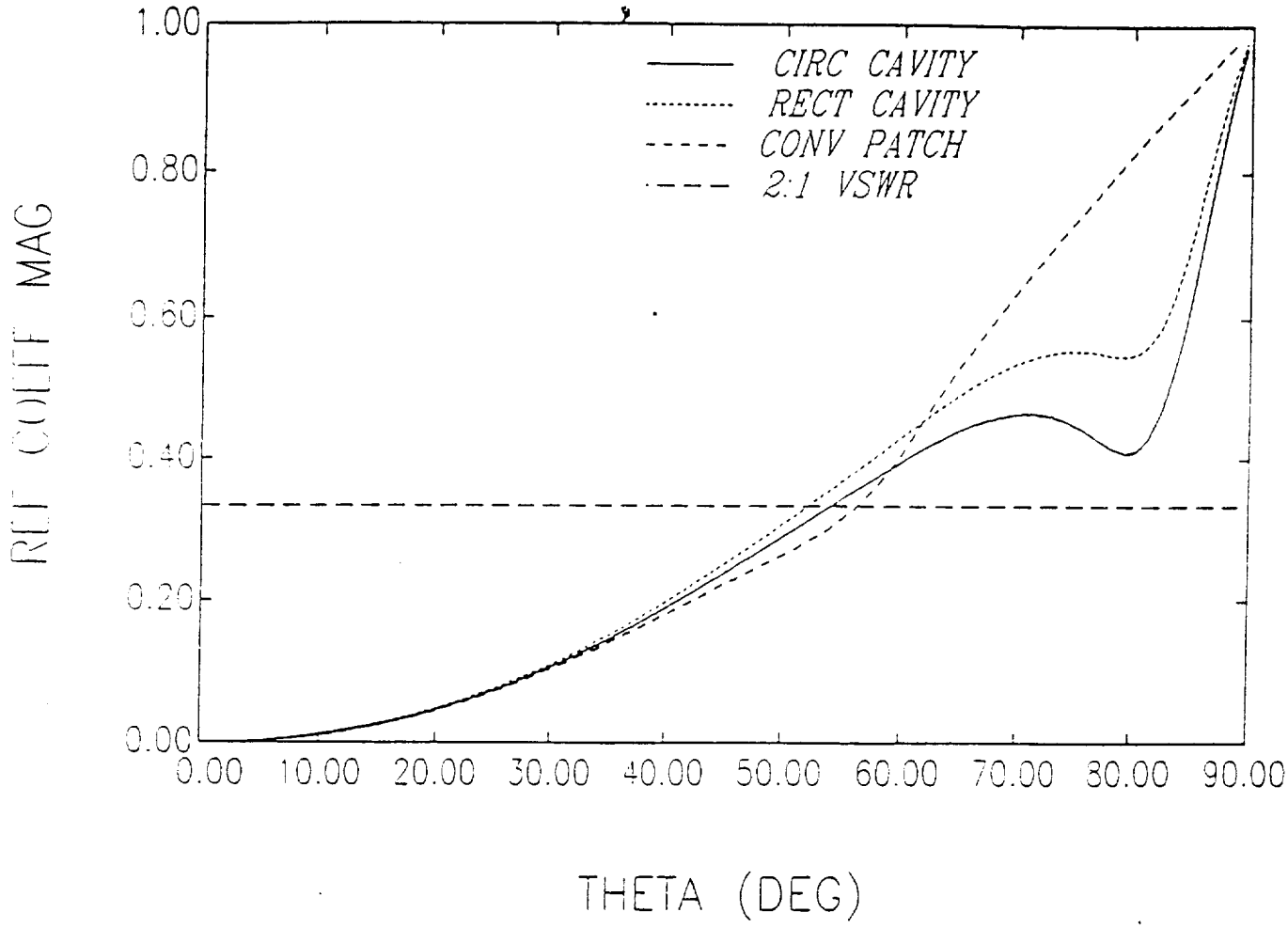

Figure 46: H-plane broadside-matched reflection coefficient versus scan angle for infinite arrays of circular and rectangular cavity-backed and conventional patches (d=0.08 λ_0).

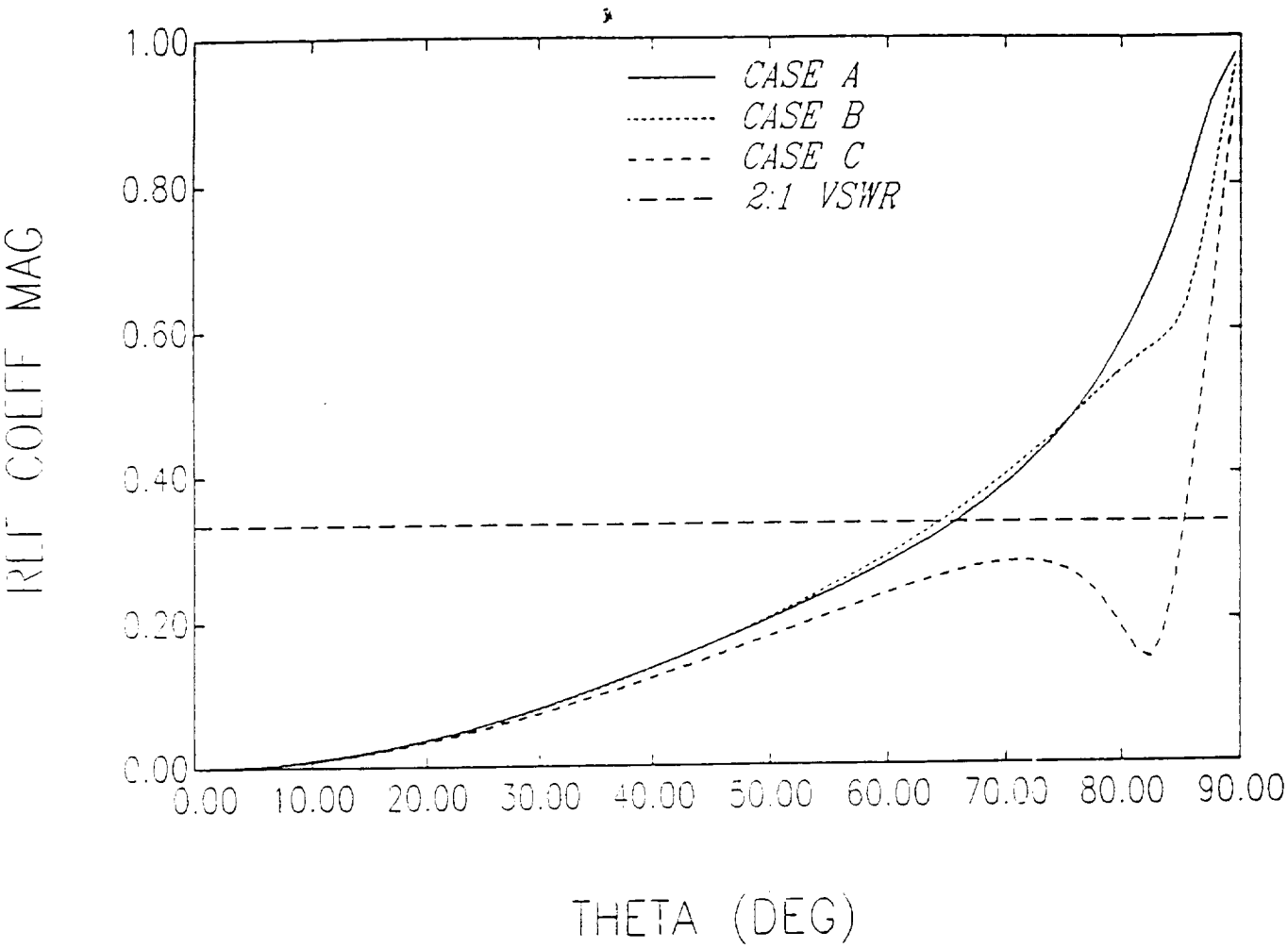

Figure 47: E-plane broadside-matched reflection coefficient versus scan angle for and infinite array of circular cavity-backed circular patches as a function of substrate thickness.

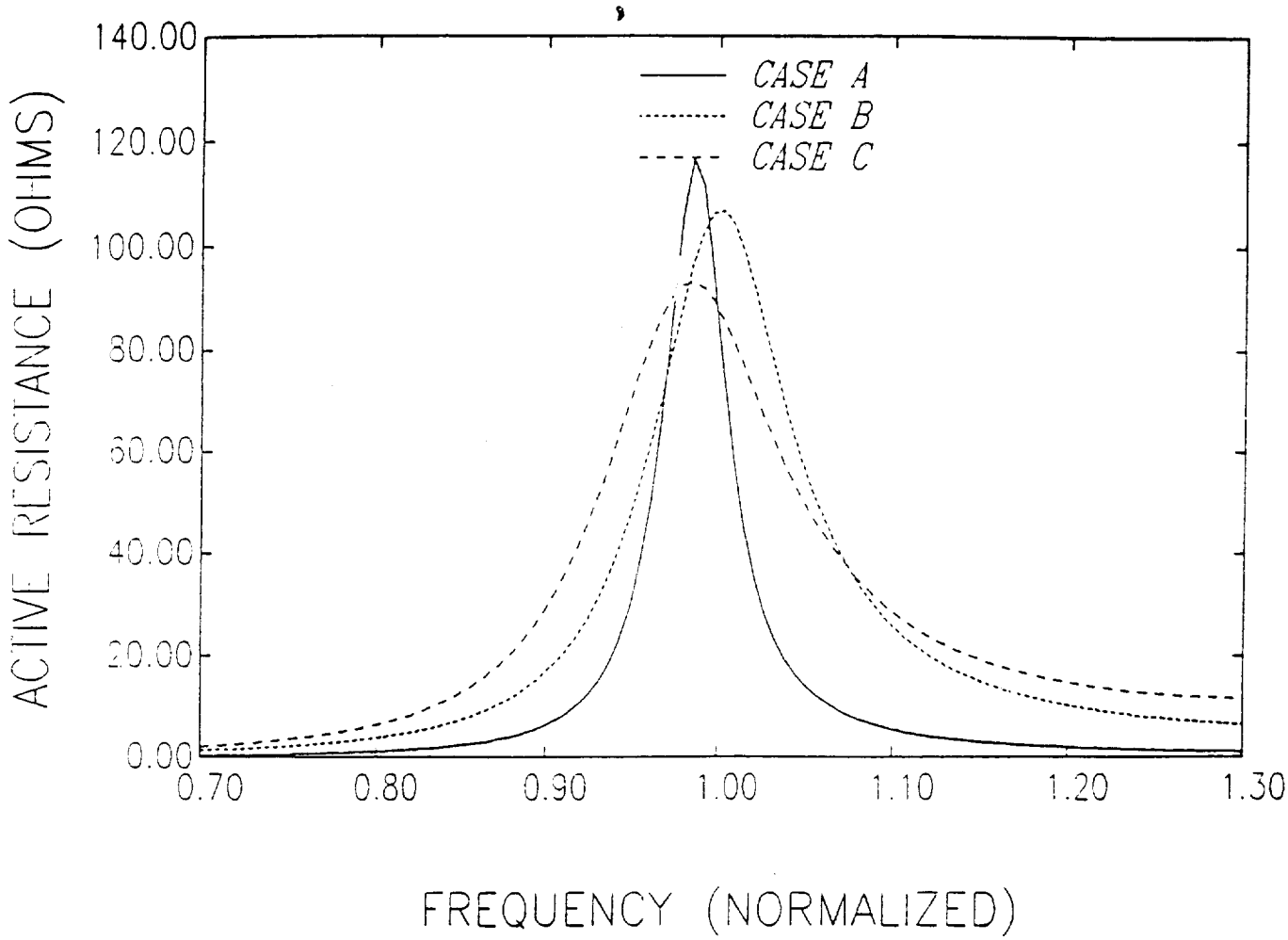

Figure 48: Active resistance versus frequency for an infinite array of circular cavity-backed circular patches as a function of substrate thickness.

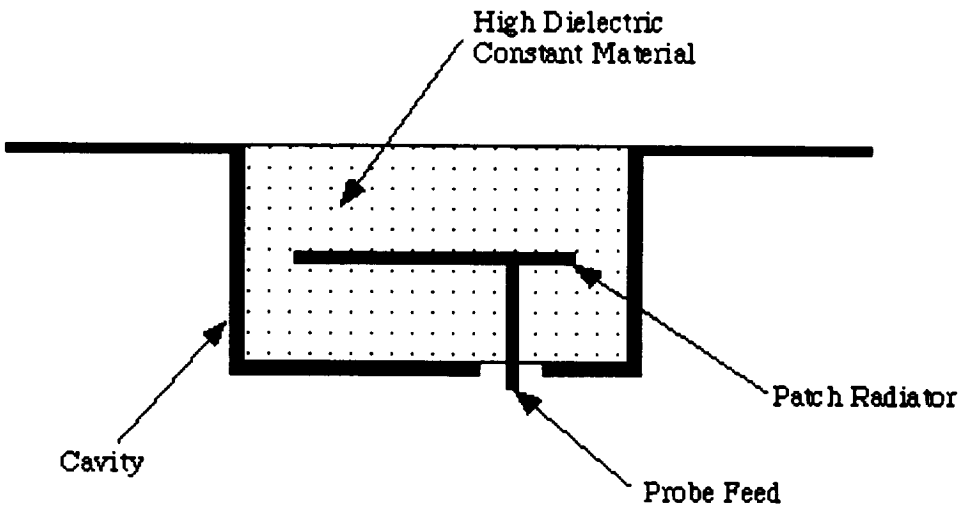

Figure 49: Geometry of a cavity-backed patch antenna that is suitable for use at UHF.

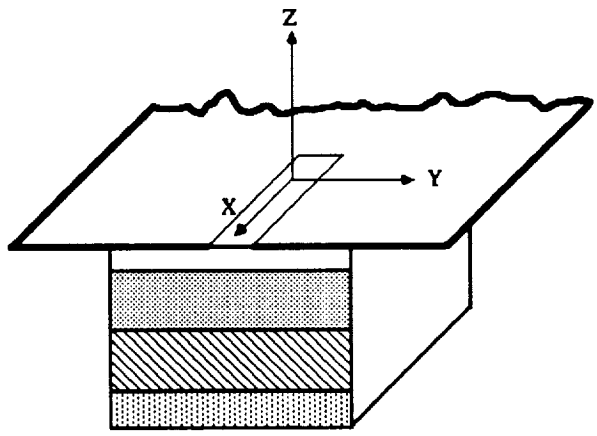

Figure 50: Sketch of CBS antenna.

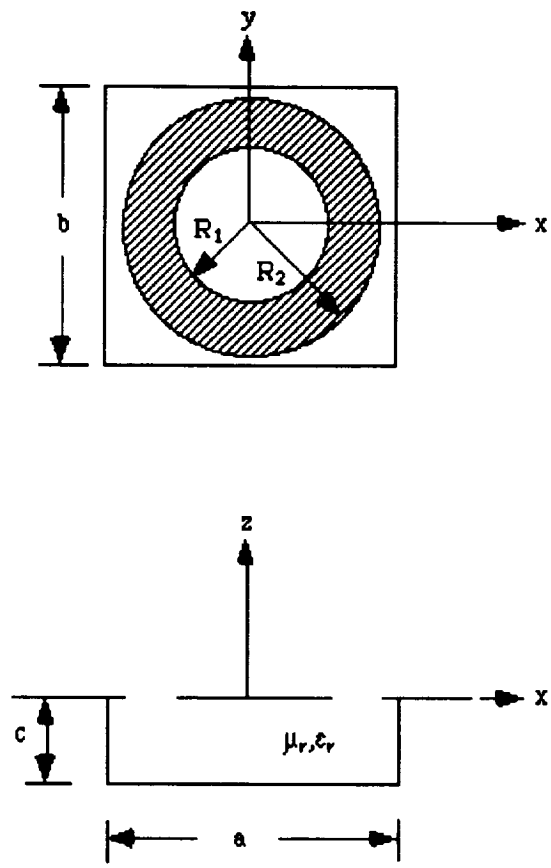

Figure 51: Geometry of Annular CBS antenna backed by a rectangular cavity.

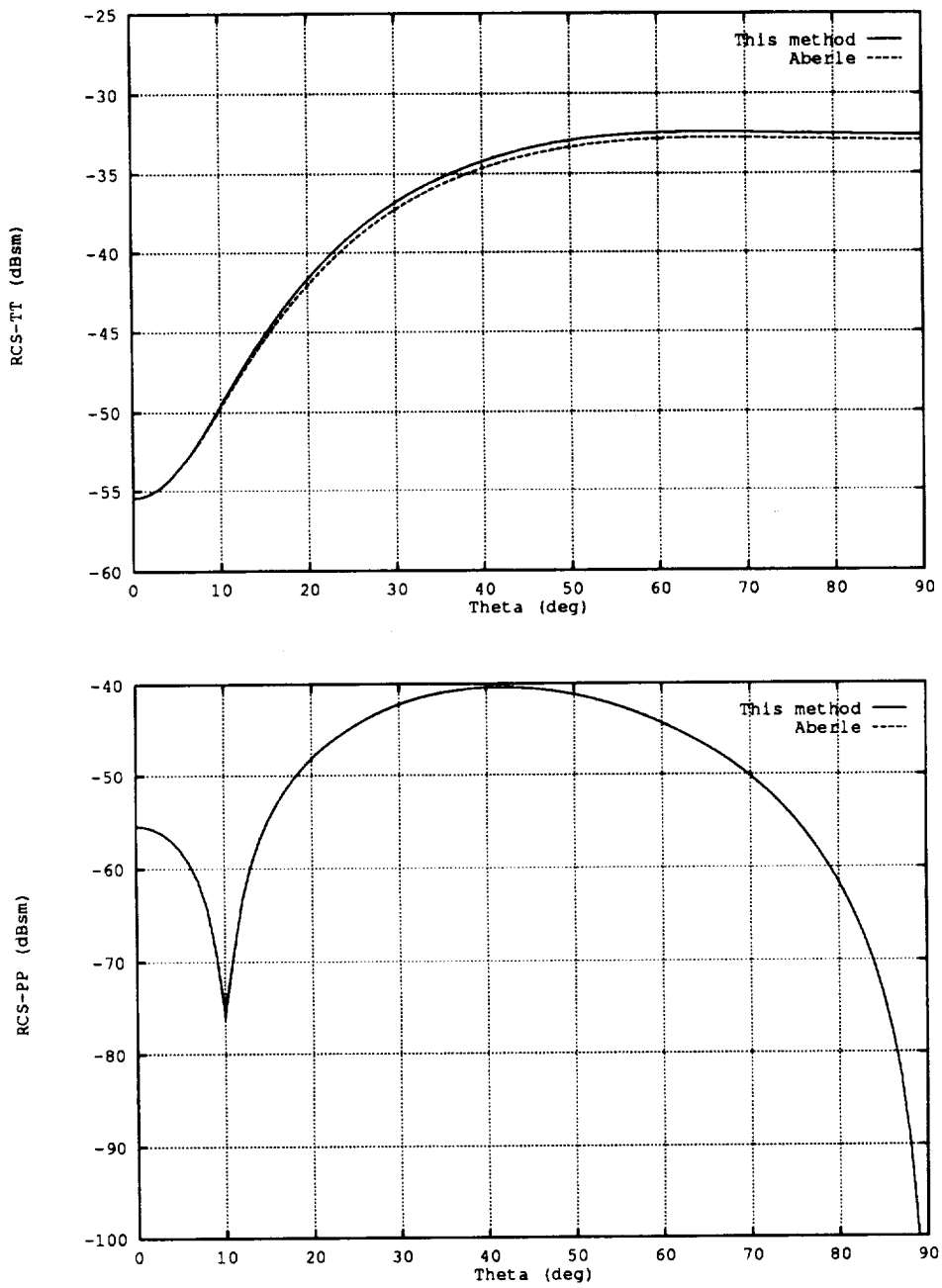

Figure 52: Comparison with Aberle for monostatic RCS at 5 GHz.

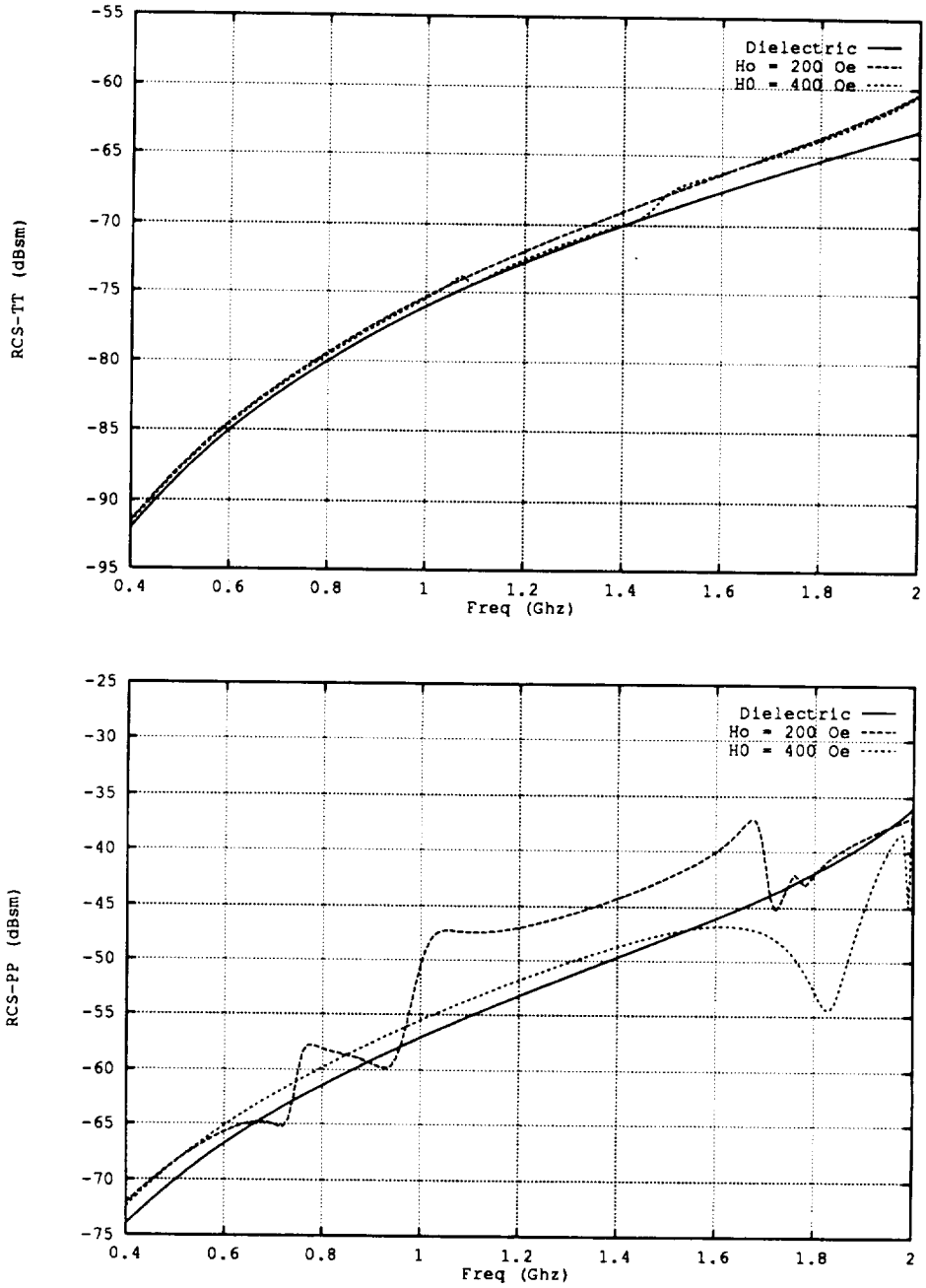

Figure 53: Monostatic RCS at normal incidence for a rectangular slot CBS antenna with varying H_0.

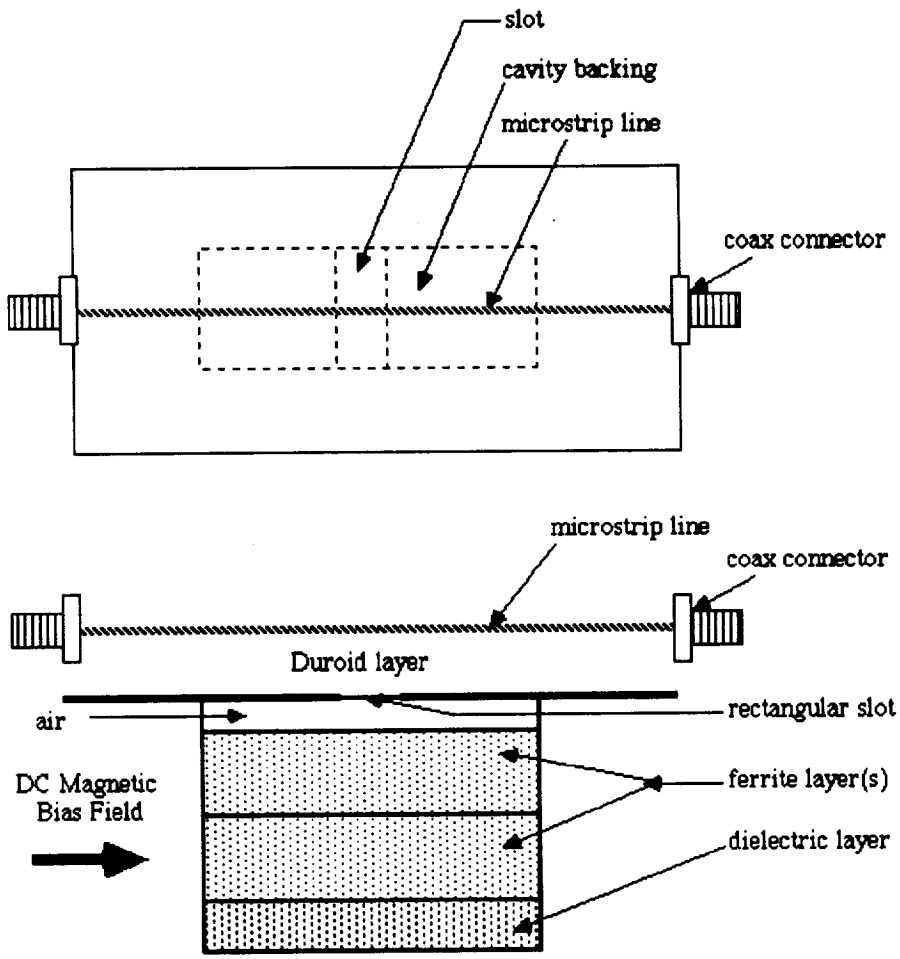

Figure 54: Original fixture for CBS antenna.

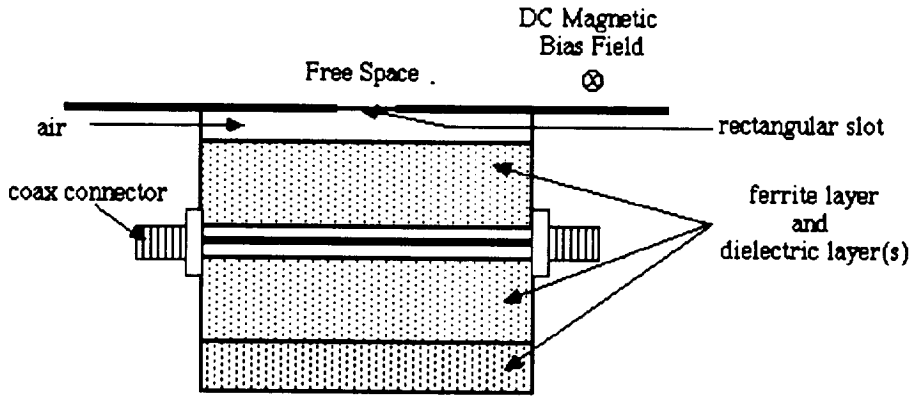

Figure 55: New CBS antenna with feed inside the cavity.

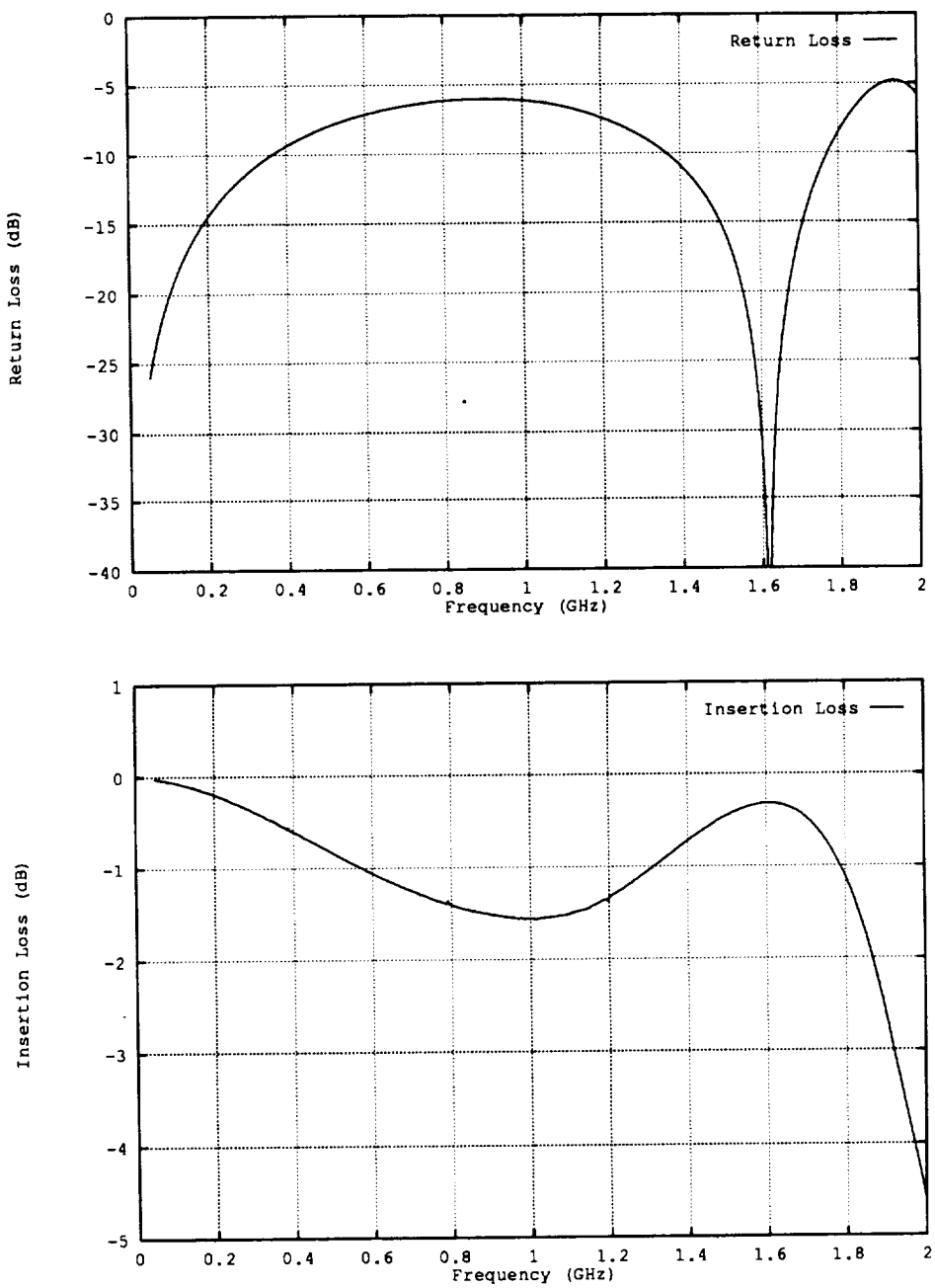

Figure 56: S_{11} and S_{21} of the ferrite and dielectric loaded closed cavity with the straight line feed.

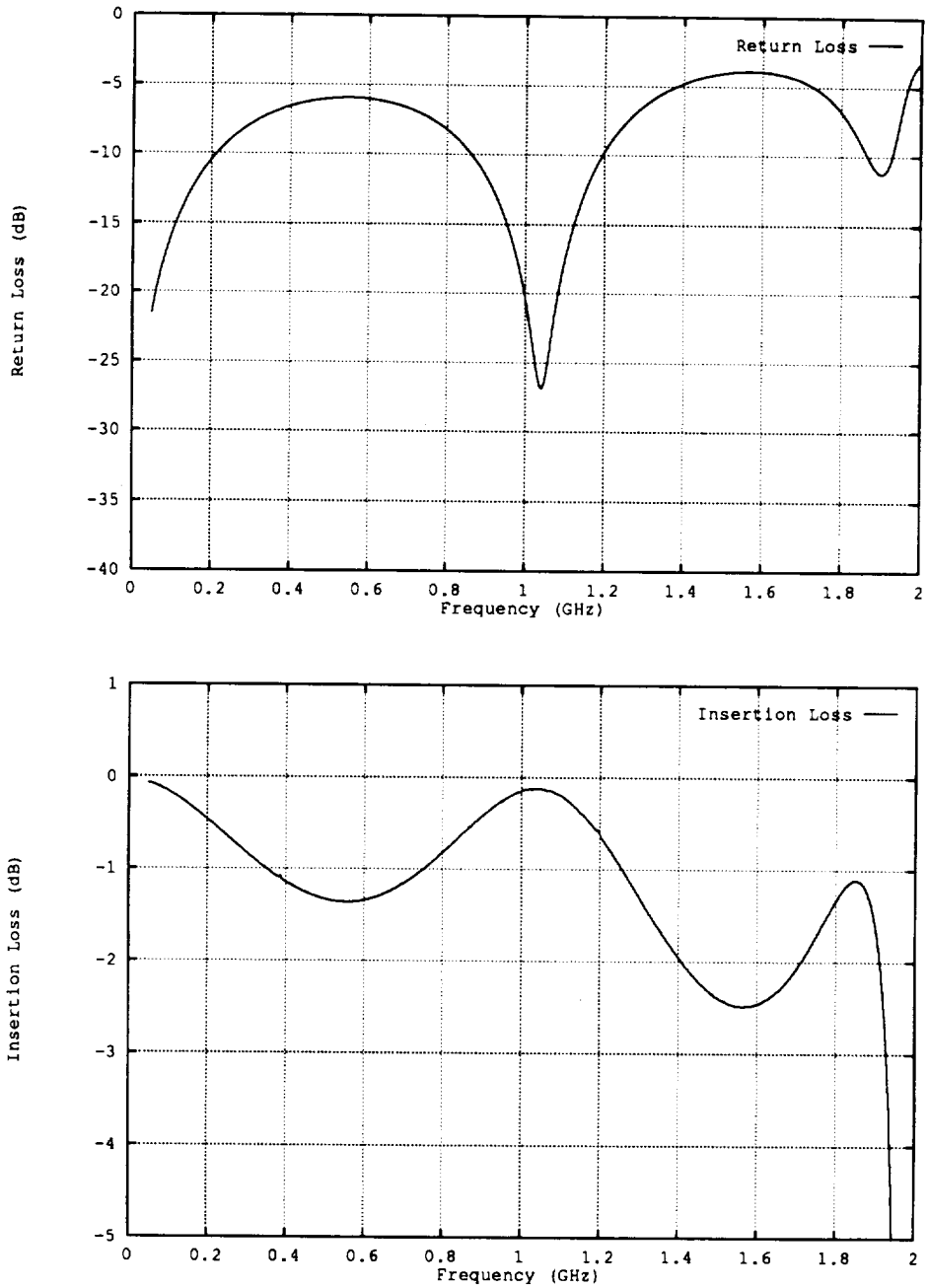

Figure 57: S_{11} and S_{21} of the ferrite and dielectric loaded closed cavity with the bent line feed with two permanent magnets.

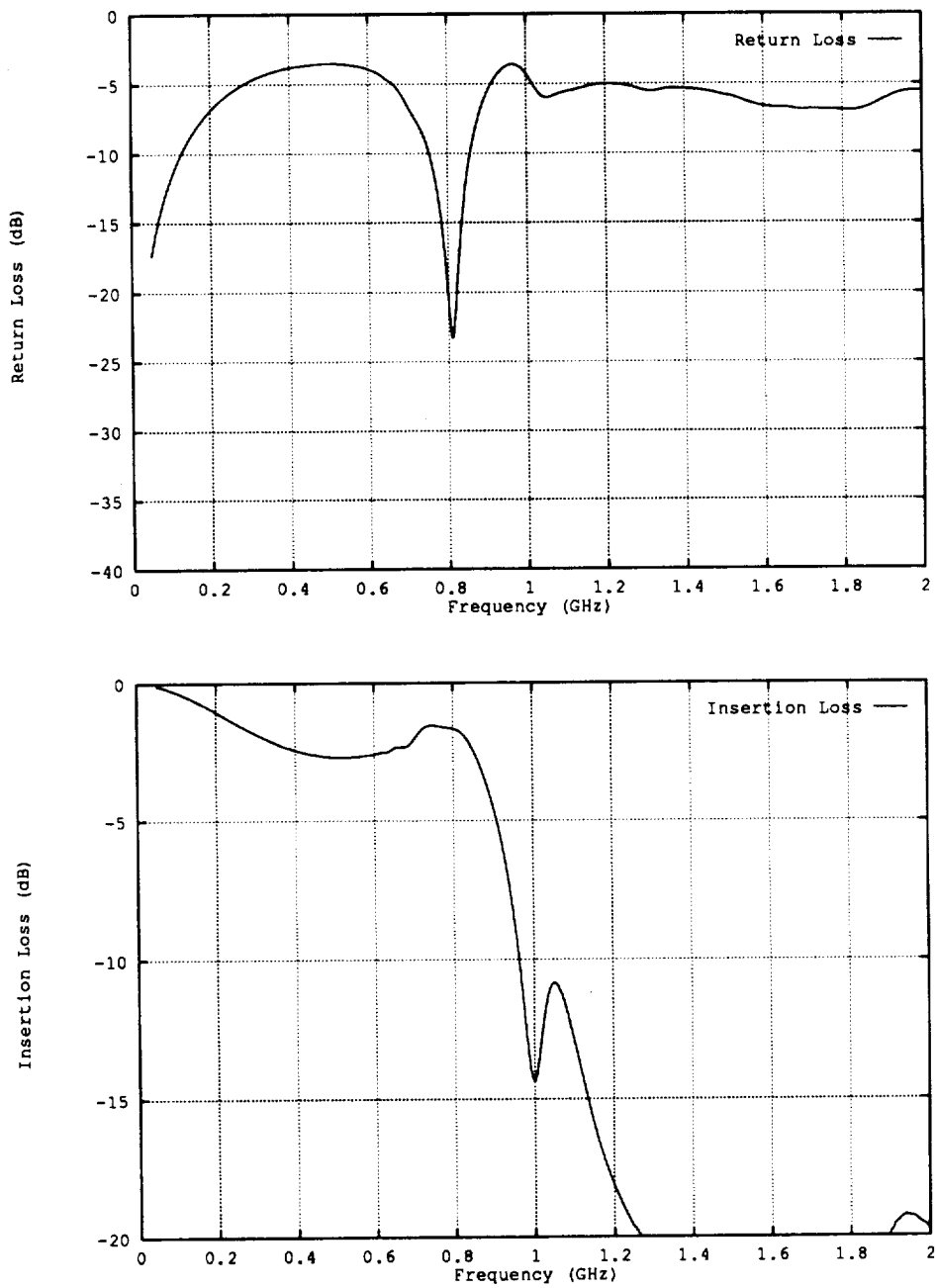

Figure 58: S_{11} and S_{21} of the ferrite and dielectric loaded closed cavity with the bent line feed with one permanent magnet.

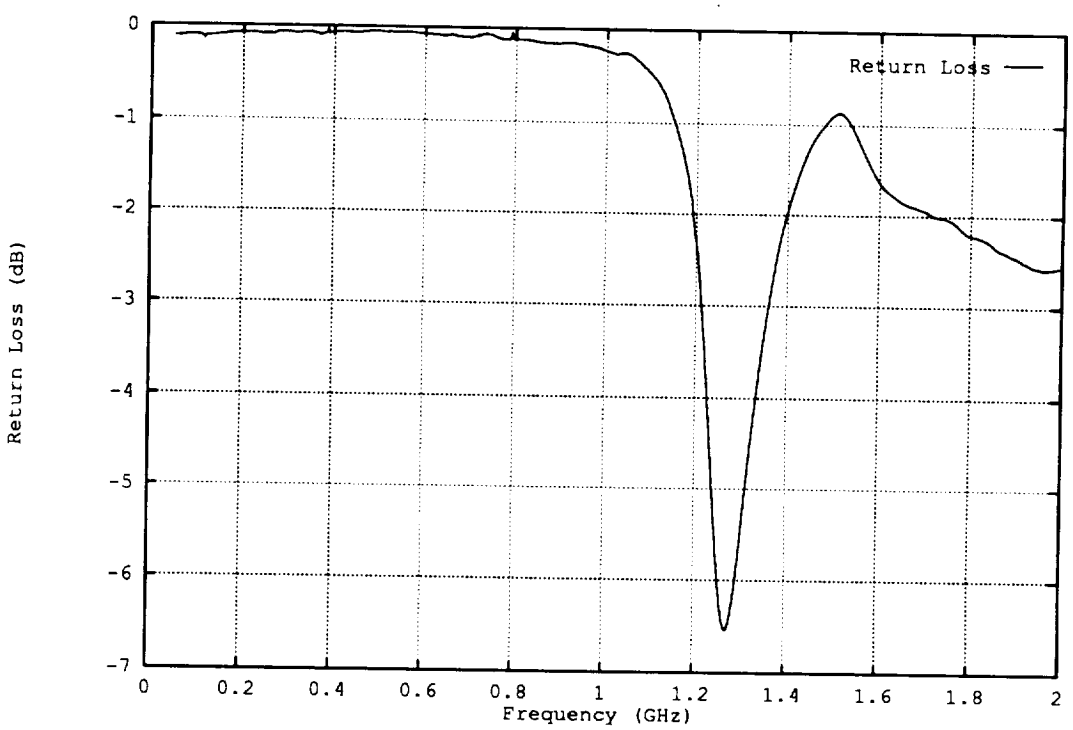

Figure 59: S_{11} of the ferrite and dielectric loaded CBS antenna with the bent line feed with one permanent magnet.

References

[1] Taflove, A. and Umashankar, K. R., "The Finite-Difference Time-Domain Method For Numerical Modeling of Electromagnetic Wave Interactions," Electromagnetics, Vol.10, pp. 105-126, Jan., 1990.

[2] Kats, D. S. and Picket-May, M. J. and Taflove, A. and Umashankar, K. R., "FDTD Analysis of Electromagnetic Radiation from Systems Containing Horn Antennas," IEEE Trans. on Antennas and Propagat., Vol. 39, pp. 1203-1212, Aug., 1991.

[3] Tirkas, P. A. and Balanis, C. A., "Finite-Difference Time-Domain Method for Antenna Radiation," IEEE Trans on Antennas and Propagat., Vol. 40, pp. 334-340, Mar., 1992.

[4] Tirkas, P. A., Balanis, C. A. and Renaut, R. A., "Higher order absorbing boundary conditions for the Finite-Difference Time-Domain Method," IEEE Trans. Antennas and Propagat. Vol. 40, pp. 1215-1222, Otc., 1992.

[5] A.T. Adams, "Flush Mounted Rectangular Cavity Slot Antennas - Theory and Design," *IEEE Trans. Antennas and Prop.*, vol. AP-15, pp. 342-351, May 1967.

[6] D.J. Angelakos and M.M. Korman, "Radiation from Ferrite Filled Apertures," *Proc. of the IRE*, vol. 44, pp. 1463-1468, October 1956.

[7] M.A. Morgan, D.L. Fisher and E.A. Milne, "Electromagnetic Scattering by Stratified Inhomogeneous Anisotropic Media," *IEEE Trans. Antennas and Prop.*, vol. 35, no. 2, p. 191, Feb. 1987.

[8] J.T. Aberle, *Novel Microstrip Antenna Configurations for Enhanced Performance,* Final Report, Air Force Engineering Foundation Grant RI-B-90-19, Sep. 1991.

[9] R.F. Harrington, *Field Computation by Moment Method,* Malabar, FL: Krieger, 1968.

[10] M.M. Ney, "Method of Moments Applied to Electromagnetic Problems," *IEEE Trans. Micro. Theo. Tech.*, vol. MTT-33, no. 10, pp. 972-980, Oct. 1985.

C 2

[11] E. El-Sharawy, "Full Wave Analysis of Printed Lines on Magnetic Substrates," Ph.D. dissertation, University of Massachusetts, 1989.

[12] B. Lax and K.J. Button, *Microwave Ferrites and Ferrimagnetics,* New York, New York, Mc-Graw Hill, Inc., 1962.

[13] H. Suhl, "The Nonlinear Behavior of Ferrites at High Microwave Signal Levels," *Proc. IRE*, vol. 44, p. 1270, 1956.

[14] C.A. Balanis, *Advanced Engineering Electromagnetics,* New York, New York, John Wiley and Sons, Inc., 1989.